REPUBLIQUE ALGERIENNE DEMOCRATIQUE ET POPULAIRE
MINISTERE DE L 'ENSEIGNEMENT SUPERIEUR
ET DE LA RECHERCHE SCIENTIFIQUE

Order number:...........
Series :.......

Mohammed Seddik Benyahia University – Jijel

Faculty of Science and Technology

Department of Electronics

Doctorate Thesis Presented

For the Obtaining of the Doctorate Degree (3rd cycle)

Specialty: **Micro optoelectronics**

By: **Taoufik DIB**

Theme:

Study of the Interaction of Optical Radiation with Binary II-VI Semiconductor Materials (ZnO and AZO)

Defended on: 2/07/2024

Thesis committee:

Mme. Douniazad Mezdour	Professor	U. M.S.B.Jijel	President
Mr. Boubekeur Birouk	Professor	U. M.S.B.Jijel	Thesis director
Mr. Riad Remmouche	Professor	U. M.S.B.Jijel	Examiner
Mr. Adel Mellit	Professor	U. M.S.B.Jijel	Examiner
Mr. Djamel Djouadi	Professor	U. Bejaia	Examiner

الملخص: الهدف الأساسي من هذا البحث هو إجراء تحليل مفصل لعينات أكسيد الزنك النقي وأكسيد الزنك المشوب بالألمنيوم، المترسبتين باستخدام تقنية الرش المغناطيسي. وينصب التركيز أيضا على ايجاد طريقة بديلة لاستخراج الخصائص الإلكتروضوئية لهذه العينات. تتضمن الدراسة التغيير في تركيبة أكسيد الزنك عن طريق ضبط تركيز الأكسجين، مما يؤدي إلى الحصول على عينات ذات خصائص مختلفة. بالاستعانة بجهاز القياس الطيفي الضوئي يتم دراسة الخصائص الإلكتروضوئية مثل تركيز الشحنة، وحركة حامل الشحنة، والمقاومة الضوئية، والمقاومة الكهربائية، والامتصاص الضوئي، وطاقة الفجوة.

بالإضافة إلى ذلك، يتم تطبيق نموذج معامل الانكسار الجديد "نموذج بيروك" لاختبار توافق وكفاءة العينات معه. وبعد ذلك، تتضمن عملية التحسين انشاء عينات مشابهة لتلك التي تظهر خصائص مفضلة من سلسلة أكسيد الزنك المشوب بالالمنيوم. يتم إجراء مزيد من التحقيق في هذه السلسلة المختارة عن طريق تغيير عامل درجة حرارة الترسيب. بالاستعانة بجهاز القياس الإهليلجي الطيفي يتم دراسة هذه العينات للحصول على فهم شامل لخصائصها. يتضمن فحص العينات تقييم نقاط قوتها للتطبيقات المحتملة في مختلف المجالات الصناعية.

لتعزيز الفائدة العملية للدراسة، يتم اشتقاق العلاقات الرياضية التجريبية لتبسيط عملية استخراج الخصائص الإلكترونية البصرية والتحقق من دقتها. يهدف هذا البحث إلى المساهمة برؤى قيمة للتطبيقات الصناعية وتوفير أساس للدراسات المستقبلية في هذا المجال.

Abstract: The main objective of this research is to conduct a detailed analysis of pure zinc oxide and aluminum-doped zinc oxide samples, deposited using the magnetron sputtering technique. The focus is on identifying an alternative method for efficiently extracting the optical-electronic properties of these samples. The study involves altering the composition of zinc oxide by adjusting the oxygen concentration, leading to obtaining samples with different properties. The optoelectronic properties such as charge concentration, charge carrier mobility, optical resistance, electrical resistance, optical absorption, and bandgap energy are studied using a spectrophotometry measurement and spectroscopic ellipsometry device.

Additionally, a new refractive index model, Birouk's model, is applied to test the compatibility and efficiency of the samples. Subsequently, the optimization process involves creating samples similar to those exhibiting preferred properties from the aluminum-doped zinc oxide series. Further investigation into this selected series is conducted by varying the annealing temperature factor. Using ellipsometry spectroscopy measurement device, these samples are studied to obtain a comprehensive understanding of their properties. Sample examination includes evaluating their strengths for potential applications in various industrial fields.

To enhance the practical benefit of the study, experimental mathematical relationships are derived to simplify the process of extracting optical-electronic properties and to verify their accuracy. This research aims to contribute valuable insights for industrial applications and to provide a basis for future studies in this field

Résumé: L'objectif principal de cette recherche est de réaliser une analyse détaillée des échantillons d'oxyde de zinc pur et d'oxyde de zinc dopé à l'aluminium, déposés en utilisant la technique de magnetron sputtering. L'accent est mis sur la détermination d'une méthode alternative pour extraire efficacement les propriétés optoelectriques de ces échantillons. L'étude comprend la modification de la composition de l'oxyde de zinc en ajustant la concentration en oxygène, conduisant à l'obtention d'échantillons aux propriétés variées. En utilisant un spectromètre optique, les propriétés électro-optiques telles que la concentration de charge, la mobilité des porteurs de charge, la résistance optique, la résistance électrique, l'absorption optique et l'énergie de la bande interdite sont étudiées.

De plus, un nouveau modèle, le modèle de Birouk, est appliqué pour tester la compatibilité et l'efficacité des échantillons. Ensuite, le processus d'optimisation comprend la création d'échantillons similaires à ceux présentant des propriétés préférées de la série d'oxyde de zinc dopé à l'aluminium. Une enquête approfondie sur cette série sélectionnée est réalisée en modifiant le facteur de température de dépôt. À l'aide d'un spectromètre ellipsométrique, ces échantillons sont étudiés pour obtenir une compréhension complète de leurs propriétés. L'examen des échantillons comprend l'évaluation de leurs points forts pour des applications potentielles dans divers domaines industriels.

Pour renforcer l'utilité pratique de l'étude, des relations mathématiques expérimentales sont dérivées pour simplifier le processus d'extraction des propriétés électroniques optiques et en vérifier la précision. Cette recherche vise à apporter des perspectives précieuses pour les applications industrielles et à fournir une base pour des études futures dans ce domaine.

DEDICATIONS

To my parents,

To my brothers and sisters,

To my friends and all my relatives,

I dedicate this work.

ACKNOWLEDGEMENTS

First and foremost, all praise is due to Allah, the Almighty, for granting me the strength to successfully complete this thesis.

I express my sincere gratitude to my esteemed supervisor, Professor Boubekeur Birouk, for selecting the topic of this thesis. I thank him for his confidence in me, his gentle guidance, and his valuable and continuous feedback throughout the creation of this work.

I extend my thanks to Mrs. Dounyazad Mezdour, professor at the University of Jijel, for accepting the invitation to chair the examination committee of this work.

My gratitude extends to Mr. Riad Remmouche, professor at the University of Jijel, for accepting the invitation to examine this work.

I also appreciate the willingness of Mr. Adel Mellit, professor at the University of Jijel, for accepting the invitation to examine this work.

I extend my thanks to Mrs. Djamel Djouadi, professor at the University of Bejaia, for accepting the invitation to examine this work.

I am also pleased to express my thanks to Professor Jean-Pierre Raskin from Louvain School of Engineering of ICTEAM-UCL, Belgium, for his valuable comments, suggestions, and engaging discussions.

Furthermore, I acknowledge and appreciate Dr. Romain Tuyaerts from Louvain School of Engineering of ICTEAM-UCL, Belgium, for his kind contribution to the experiments, including samples deposition and measurements, conducted at ICTEAM-UCL-Belgium.

I thank everyone who supported and assisted me, whether from afar or nearby, throughout my academic journey from elementary school to graduate studies.

Finally, I extend my deepest gratitude to my family, who deserves the greatest credit after Allah. I thank them for their encouragement, support, and upbringing that has led me to achieve what I have reached today.

Contents

Contents

List of Figures

List of Tables

General Introduction 13

Chapter I: Literature Review and Theoretical Framework

1 Basic characteristics of Zinc Oxide 4

1.1 Cristal structure 4

1.2 Electrical Properties 6

1.2.1 Native points defects 6

1.2.1.1 Oxygen and Zinc interstitial (O_i, Zn_i) 7

1.2.1.2 Oxygen and Zinc vacancies (V_O, V_{Zn}) 7

1.2.1.3 Concentration of a point defect 8

1.2.2 Scattering charge carriers in ZnO Crystals 8

1.2.2.1 Acoustical Scattering 8

1.2.2.2 Ionized Impurity Scattering 9

1.2.2.3 Neutral impurity scattering 9

1.2.2.4 Anisotropic Scattering 10

1.2.2.5 Optical scattering 10

1.2.3 Scattering in thin films 11

1.2.3.1 Grain Boundary Scattering 11

1.2.3.2 Dislocation Scattering 12

1.2.4 Zinc oxide electrical conductivity 12

1.2.5 Zinc oxide electrical mobility 14

1.3 Zinc Oxide Optical Properties 15

2 Application of ZnO 17

2.1 Solar cells 18

2.2 Light Emitting Diodes 19
2.3 Transparent Film Transistors (TFT) 20
2.4 ZnO Sensors: 22
2.4.1 Gas Sensors 22
2.4.2 Chemical Sensors 23
2.4.3 Pressure Sensors 24
2.4.4 UV Sensors 25
3 Deposition techniques 26
3.1 Chemical deposition techniques 27
3.1.1 Chemical Vapor Deposition (CVD) 28
3.1.2 Atomic Layer Deposition (ALD) 28
3.1.3 Chemical Bath Deposition (CBD) 29
3.1.4 Sol-Gel Deposition 30
3.2 Physical Deposition Techniques 31
3.2.1 Electron Beam Evaporation (EBE) 31
3.2.2 Magnetron Sputtering 33
3.2.3 Pulsed Laser Deposition (PLD) 34

Chapter II: Experimental techniques of measurement and methods

1 Introduction 34
2 Spectroscopic ellipsometry 34
2.1 Data analysis procedure 36
2.2 Application of spectroscopic ellipsometry 37
2.3 Advantages and drawbacks of spectroscopic ellipsometry 38
3 Spectrophotometry 39
3.1 Absorption coefficient 39
3.2 Refractive index 42
3.2.1 What advantages does the investigation of thin film refractive index offer? 42
3.2.2 The refractive index of thin film models 43
3.2.2.1 Cauchy Equation 44
3.2.2.2 Sellmeier Equation 44
3.2.2.3 Drude-Lorentz's Model 44
3.2.2.4 Tauc-Lorentz's Model 45
3.2.2.5 Birouk's Model 45

4 Hall measurement 46
5 Sputtering method 48

Chapter III: ZnO Thin Films

1 Introduction 50
2 Deposition of ZnO thin films using a sputtering system 51
3 Samples characteristics 53
3.1 Ellipsometry Spectra of the samples 53
3.2 Absorption coefficient of thin films 59
3.3 Bandgap and Urbach energy 61
3.4 Optical conductivity 63
4 Analyzing the refractive index through modeling 66
5 Conclusion 75

Chapter IV: AZO Thin Films

1 Introduction 73
2 Experimental method of AZO thin film deposition 73
3 Results and discussions 76
3.1 Spectroscopic ellipsometry and optoelectrical properties at the theoretical level 77
3.2 Variation of oxygen concentrations 80
3.2.1 Spectroscopic ellipsometry measurement 80
3.2.2 Electrical properties 85
3.2.3 Optical properties 94
3.3 Variation of deposition temperature 96
3.3.1 Electrical properties 100
3.3.2 Optical property 104
4 Conclusion 106
General Conclusion 103
References 105

List of Figures

Figure I. 1: ZnO crystal structures: (a) cubic rock-salt (B1), (b) cubic zinc blende (B3), and (c) hexagonal wurtzite (B4).. 5
Figure I. 2: ZnO wurtzite structure, also known as B4 type structure (Bravais lattice type). 5
Figure I. 3: The calculated band structure of Wurtzite ZnO using the HSE hybrid functional. The energy of the valence-band maximum was set to zero. 6
Figure I. 4: various defects present in a crystal. 7
Figure I. 5: Diagrammatic energy depicting the potential radiative transitions of zinc oxide caused by various levels of defects. 16
Figure I. 6: Applications of ZnO in different fields. We will briefly consider some of these applications. 17
Figure I. 7: The advantages of ZnO for solar cell application. 18
Figure I. 8: (a) illustrates the application of ZnO in nascent solar cell technologies, and (b) the quantity of research papers associated with ZnO in emerging solar cell technologies 19
Figure I. 9: depicts the annual publication trend of papers related to oxide TFTs. 21
Figure I. 10: Zinc oxide thin-film transistor (TFT) with a bottom gate configuration. 22
Figure I. 11: depicts a schematic representation of three prevalent transduction mechanisms alongside representative devices: (a) piezoresistivity, (b) capacitance, and (c) piezoelectricity. 24
Figure I. 12: Schematic diagram of UV sensor with ZnO nanostructures, bridge network. 26
Figure I. 13: Thin film deposition techniques. 27
Figure I. 14: Cycle of ALD deposition. 29
Figure I. 15: Schematic of Chemical Bath Deposition. 30
Figure I. 16: Schematic illustration of the spin coating process. 31
Figure I. 17: e-beam evaporation system. 32
Figure I. 18: Schematic illustration of magnetron sputtering method. 34
Figure I. 19: Schematic diagram of the pulsed laser deposition system. 35

Figure II. 1: The ellipsometry measurement is depicted using incident linearly polarized light aligned with both p- and s-components. When this light interacts with the sample, it results in distinct amplitudes and phase shifts for the reflected p- and s-polarizations, ultimately generating elliptically polarized light. Ψ is the amplitude by degree, and Δ the phase difference by degree. 35
Figure II. 2: Flow chart of the data analysis procedure. 37
Figure II. 3: Characterization of physical properties by spectroscopic ellipsometry. 38
Figure II. 4: Explanation of the Tauc-plot method on the curve level thanks to the absorption coefficient. 41
Figure II. 5: Schematic representation of Urbach tail states in a semiconductor system. 42
Figure II. 6: Schematic diagram of a Hall effect . 46
Figure II. 7: Contact positions of samples in Van der Pauw geometry. 48
Figure II. 8: Working mechanism of sputtering technique 48

Figure II. 9: The sputtering machine employs a unique setup for its sputtering guns. This setup incorporates permanent magnets to confine the plasma close to the target material. Furthermore, a system of water channels is in place to efficiently cool the target. Additionally, Oxygen-free High Conductivity (OFHC) copper electrodes are utilized to apply voltage to the target. 49

Figure III. 1: The sputtering chamber utilized for depositing ZnO, AZO thin films. A quartz microbalance was utilized to measure the deposition rate in real-time, and a thermocouple was integrated within the chamber to closely monitor temperature variations. Additionally, to achieve excellent uniformity, the samples were subjected to rotation at a speed of 45 revolutions per minute (rpm) 52
Figure III. 2: Evolutions of ellipsometry ratio ψ as a function of wavelength for different samples of ZnO thin films, the peaks in the spectra of the samples are denoted by ψ_{max}. 54
Figure III. 3: Evolution of the ellipsometry parameter ψ_{max} as a function of varying oxygen concentrations. 55
Figure III. 4: Evolution of the ellipsometry parameter ψ_{max} versus thickness of ZnO samples. 55
Figure III. 5: Evolutions of ellipsometry phase difference Δ as a function of wavelength for different samples of ZnO thin films, the wavelengths at peaks and downs in the spectra of the samples are denoted by $\lambda_{\Delta 1}$ for part 1, and $\lambda_{\Delta 2}$ for part 2. 56
Figure III. 6: $\lambda_{\Delta 1}$, and $\lambda_{\Delta 1}$ values as a function of oxygen concentration for ZnO thin films 57
Figure III. 7: $\lambda_{\Delta 1}$ comportment values versus ZnO thin film thicknesses. 58
Figure III. 8: $\lambda_{\Delta 2}$ comportment values as a function of the thickness of ZnO thin films. 58
Figure III. 9: Extinction coefficient variations as functions of incident radiation wavelength for different ZnO thin films. 60
Figure III. 10: Absorption coefficient variations as functions of incident radiation wavelength for different ZnO thin films. 60
Figure III. 11: Variation of $(\alpha h\upsilon)^2$ with the photon energy ($h\upsilon$) for different ZnO thin films (Thin arrow represents the linear behavior according to Tauc's relationship) 62
Figure III. 12: Bandgap energy variation as a function of different oxygen concentrations of ZnO thin films. 62
Figure III. 13: Urbach energy variation as a function of different oxygen concentrations of ZnO thin films. 63
Figure III. 14: Dependence of optical conductivity upon the wavelength of the incident photon for ZnO thin films. 64
Figure III. 15: Optical conductivity versus wavelength of the incident photon at a small range wavelength. 65
Figure III. 16: Optical conductivity as a function of oxygen concentration at several specific wavelength. 65
Figure III. 17: Refractive index development of ZnO thin films versus wavelength at visible and near-infrared range……………………………………………………………………………..………………66
Figure III. 18: Development extinction coefficient k for ZnO thin films versus wavelength at visible and near-infrared range. 67
Figure III. 19: Variation of refractive index square of ZnO thin films versus wavelength square. 68
Figure III. 20: Variation of the fitting parameters variations of the refractive index according to their position in the equation, parameters by order, the curves for ZnO deposits (one curve per sample characterized by its different oxygen concentration). 70

Figure III. 21: Absolute values of experimental fitting parameters versus their position in the equation, for ZnO deposits (one curve per sample characterized by its oxygen concentration), the dashed lines are Gaussian fittings........ 71
Figure III. 22: Different fitting parameter as a function of ZnO oxygen concentration (One curve per one parameter in all samples). 71
Figure III. 23: Refractive indices versus wavelength for different ZnO samples within the visible to near-infrared (Vis-NIR) wavelength range. Both experimental data and Birouk's model are included in the comparison........ 74
Figure III. 24: Refractive indices versus wavelength for ZnO sample at 27 % oxygen concentration within wider wavelength range. Both experimental data and Birouk's model are included in the comparison........ 75
Figure IV. 1: Thickness of AZO samples parameterized as a function of oxygen concentration. 75
Figure IV. 2: Plot of AZO samples thickness versus deposition temperature, with a 20% oxygen concentration........ 76
Figure IV. 3: Different curves of ellipsometric ψ angles versus wavelength λ of AZO thin films prepared at different O_2 concentrations. 80
Figure IV. 4: Different curves of ellipsometry Δ angles versus wavelength λ of AZO thin films prepared at different oxygen concentrations........ 81
Figure IV. 5: Ellipsometry ψ angles taken from AZO thin films prepared at different O_2 concentrations. 82
Figure IV. 6: ψ_{max} values of AZO thin films spectra as a function of oxygen concentration. 82
Figure IV. 7: Logarithm of oxygen concentration evolution versus Ψ angle extrema. 83
Figure IV. 8: Delta spectra as function of wavelength, of different AZO samples made with several oxygen concentration........ 84
Figure IV. 9: Evolution of charge carrier density versus Ψ_{max} angles for different AZO samples, showing the equation of the fitting curve. 86
Figure IV. 10: Evolution of resistivity as a function of Ψ_{max} angles for different AZO samples without S6 (resistive behavior)........ 87
Figure IV. 11: Evolution of mobility as a function of ellipsometric Ψ_{max} angles for different AZO samples........ 88
Figure IV. 12: a and b are Curves of Charge carrier density as function of $\lambda_{\Delta 1}$ and $\lambda_{\Delta 2}$ oscillations peaks respectively, for different AZO deposits with different oxygen concentrations........ 90
Figure IV. 13: (a and b) are Curves of mobility as function of $\lambda_{\Delta 1}$ and $\lambda_{\Delta 2}$ oscillations peaks respectively, for different AZO deposits with different oxygen concentrations. 91
Figure IV. 14: (a, b) are Curves of Charge carrier density and Resistivity, respectively, as function of Ψmin, for different AZO deposits with different oxygen concentrations........ 93
Figure IV. 15: Optical Bandgap energy versus Ψ_{max} for AZO thin films: (a) Experimental points; (b) log-log scale. 94
Figure IV. 16: Experimental points of bandgap energy versus Ψ_{min} for AZO thin films. 96
Figure IV. 17: Experimental (a) amplitude component Ψ, and (b) phase difference Δ, of the polarized reflected light from the surface of AZO films deposited at different temperatures........ 98
Figure IV. 18: Experimental results collected from the polarized reflected light on the surface of AZO films and plotted as a function of the deposition temperature: (a) maximum amplitude component Ψ_{max}; (b) minimum amplitude component Ψ_{min}........ 99
Figure IV. 19: Mobility of AZO thin films versus the minimal value of ellipsometric angle Ψ_{min}. 100
Figure IV. 20: Resistivity of AZO deposits versus Ψ_{max} angle at different deposition temperatures:(a) without S_1 sample; (b) with S_1sample........ 102

Figure IV. 21: Bandgap energy of AZO thin films deposited at different temperatures, as function of minimal values of ellipsometric angle Ψ_{min}. 104

List of Tables

Table IV. 1: Thickness of AZO samples (Sn) deposited at ambient temperature, and various oxygen concentrations, by DC magnetron reactive sputtering method. 74
Table IV. 2: Thickness of AZO samples (Sn) deposited at various temperatures, with a 20% oxygen concentration. 75
Table IV. 3: Comparison between measured and calculated AZO thin film oxygen concentration for "Ψ_{max} method". 84
Table IV. 4: Comparison between measured charge carrier density, resistivity and mobility values and calculated ones with the "Ψ_{max} method", of the various AZO deposits. 89
Table IV. 5: Comparison between measured and calculated AZO thin film bandgap energy Eg, in "Ψ_{max} method" case. 95
Table IV. 6: Comparison between measured and calculated, charge carrier density and mobility, of AZO thin films deposited at different temperatures. 103
Table IV. 7: Comparison between measured and calculated bandgap energy of AZO thin films deposited at different temperatures, in case of "Ψ_{min} method". 105
Table IV. 8: A table summarizing the optoelectrical properties of AZO thin films in relation to variations in oxygen concentration across three modes, along with the factors influencing these changes (The results are consistent with the literature[186]) 106
Table IV. 9: A table presenting a concise summary of select optoelectrical properties of AZO thin films with varying temperatures of deposition while maintaining a constant oxygen concentration, along with the influencing factors behind these changes (The results are consistent with the literature [186]). 107

List of tables

Table III. 1: Thickness t of ZnO thin films on silicon oxide substrate at different oxygen concentration. 53
Table III. 2: Data of polynomial fitting of refractive index models for different ZnO thin films at 9 degrees (10 terms). 69

Table IV. 1: Thickness of AZO samples (Sn) deposited at ambient temperature, and various oxygen concentrations, by DC magnetron reactive sputtering method. 74
Table IV. 2: Thickness of AZO samples (Sn) deposited at various temperatures, with a 20% oxygen concentration. 75
Table IV. 3: Comparison between measured and calculated AZO thin film oxygen concentration for "Ψ_{max} method". 84
Table IV. 4: Comparison between measured charge carrier density, resistivity and mobility values and calculated ones with the "Ψ_{max} method", of the various AZO deposits. 89
Table IV. 5: Comparison between measured and calculated AZO thin film bandgap energy Eg, in "Ψ_{max} method" case. 95
Table IV. 6: Comparison between measured and calculated, charge carrier density and mobility, of AZO thin films deposited at different temperatures. 103

Table IV. 7: Comparison between measured and calculated bandgap energy of AZO thin films deposited at different temperatures, in case of "Ψ_{min} method".. 105
Table IV. 8: A table summarizing the optoelectrical properties of AZO thin films in relation to variations in oxygen concentration across three modes, along with the factors influencing these changes (The results are consistent with the literature[186]) 106
Table IV. 9: A table presenting a concise summary of select optoelectrical properties of AZO thin films with varying temperatures of deposition while maintaining a constant oxygen concentration, along with the influencing factors behind these changes (The results are consistent with the literature [186])......... 107

General Introduction

General Introduction

The exploration of materials and their interactions with light encompasses a vast and enduring field of scientific inquiry. Researchers have been captivated by this pursuit for decades, driven by the desire to unveil the unique properties of materials and harness them for practical applications, particularly in the realm of thin films. Thin films, characterized by their practical efficiency across industrial applications, have experienced remarkable growth in recent decades.

Among the myriad materials under investigation, semiconductors, especially transparent varieties, hold a prominent position due to their distinct properties that render them well-suited for optoelectronic applications such as solar cells and flexible displays. Transparent conductive oxides (TCOs), a prevalent class of transparent conductive materials, have garnered significant attention in this regard. Notably, three popular classes of TCOs include SnO_2:X, ZnO:X, and In_2O_3, with intrinsic band gaps approximately ranging from 2.7 to 3.6 eV[1].

Within the realm of transparent semiconductors, aluminized zinc oxide (AZO) emerges as a particularly promising candidate. With its high transparency (>90%)[2], low resistance, cost-effectiveness, non-toxicity, and exceptional quality even in room temperature deposition, AZO stands out as an appealing choice for various applications.

Despite the strides made in understanding the properties of zinc oxide, there remains a significant scope for further research, especially in controlling various deposition factors such as semiconductor material proportions between Zn and O_2, deposition temperatures, and diverse doping techniques. Additionally, the field grapples with challenges, particularly in complex methodologies for measuring the ferroelectric properties of zinc oxide thin films, as well as thin films in general. For instance, measurements of gap energy and the index of refraction, as well as electrical conductivity, entail multiple successive stages, which can be both accurate and somewhat intricate in practice.

This study aims to address these limitations and contribute to the advancement of our understanding of both pure and impure zinc oxide materials.

The primary aim of this research encompasses two parallel objectives:

- Firstly, it involves a comprehensive exploration of the interference properties of light with zinc oxide, particularly focusing on optoelectrical properties.
- The second objective revolves around the quest for an alternative scientific and practical method facilitating the measurement of these characteristics. This method aims to be non-contact and efficient, steering clear of traditional and time-consuming procedures. It's noteworthy that certain methods have already been initiated, as evidenced in the existing literature[3].

The study covers fundamental aspects, such as providing analyses and augmentations to the optoelectrical properties of zinc oxide, and seeks alternative measurement methods for these

properties. Additionally, it delves into sub-aspects, including the analysis of experimental results based on an optical model of the index of refraction.

Systematic scientific approach for study

In this study, a systematic scientific approach was adopted:

- *Preparation of the Experiment:*

  This involves depositing thin films of ZnO and AZO on silicon oxide SiO_2 substrates using the sputtering technique. Various factors, such as differences in oxygen concentration and deposition temperature, are carefully controlled.

- *Measurement and Results Extraction Procedure:*

  Samples are exposed to various measurement devices, including a spectroscopic ellipsometry device providing optical spectra, a four-point and Hall Effect apparatus for measuring electrical properties, and also a Spectrophotometre, an advanced Zeiss Ultra 55 field emission gun scanning electron microscope (FEGSEM) equipment.

- *Analysis of Results:*

  An exceptional analysis is performed by combining certain optoelectrical properties to unveil novel insights into the behavior of (ZnO, AZO) samples under light. Equations are developed to rapidly, non-distractively, and accurately extract material properties.

The research's scope and limitations are defined by the experimental conditions applied in this study. The data and numerical equations are constrained by these conditions, encompassing factors such as the spectral field limits and the proportions of oxygen and zinc compositions. Despite these constraints, certain results from the study offer generalizability. This includes insights into the overall behavior of optoelectrical properties in zinc oxide samples, the alignment of study outcomes with specific models such as the Birouk's model (a novel model for determining the refractive index of semiconductor thin films), and the established relationships derived from the experiment. These relationships are user-friendly for extracting material properties, with applicability to various situations.

The general structure of the study's chapters and the aspects covered are outlined as follows:

- **Chapter I**
  The initial chapter serves as a broad introduction, providing an overview of the fundamental properties of zinc oxide. It delves into both electrical and optical characteristics while showcasing potential applications for the material. Additionally, it outlines renowned methods for fabricating films using zinc oxide.

- **Chapter II**
  Chapter Two focuses on the apparatus and methodologies employed in the creation of ZnO and Al doped ZnO (AZO) samples. It details the devices and techniques used for extracting electro-optical properties from these films, along with methods for result analysis.

- **Chapter III**
  This section delves into the investigation of zinc oxide films, specifically focusing on the methodology for depositing these films and subsequently extracting and analyzing their optical properties. The emphasis on optical properties, rather than electrical properties, is motivated by the inherent high resistance of pure zinc oxide in the electrical aspect, contrasting with its notable strength in transparency. The chapter also explores the correlation between the refractive index of zinc oxide samples and a novel refractive index model (Birouk's model).

  Chapter IV
  Chapter Four delves into an exploration of the optoelectrical properties of aluminum-doped zinc oxide (AZO) samples across various oxygen concentration ratios and deposition temperatures. The chapter not only elucidates the impact of these variables on the optoelectrical properties but also establishes the pure mathematical relationship between thin film characteristics and spectroscopic parameters (ψ and Δ). By amalgamating these recent findings, a comprehensive investigation of these properties unfolds, leading to the derivation of equations that offer a streamlined approach for assessing the photovoltaic properties of AZO films.

Chapter I: Literature Review and Theoretical Framework

1 Basic characteristics of Zinc Oxide

Wide bandgap materials typically exhibit electrical insulating properties, while most conducting materials are opaque to visible light. An intriguing exception to this norm lies in a class of oxide semiconductors known for their dual attributes of being good electrical conductors and transparent in the visible region of the electromagnetic spectrum[4]. Despite being recognized for over half a century, these materials, termed transparent conducting oxides (TCOs), remain among the least understood semiconductors[5]. This class includes binary materials like ZnO, SnO_2, CdO, and Ga_2O_3, along with multi-component oxides such as indium–gallium–zinc oxide and cubic spinel compounds like $CdIn_2O_4$ and $SnZn_2O_4$.

Specifically, TCOs with wide band gaps (Eg > 3 eV) exhibit remarkable electrical conductivity (~10^3 – 10^4 S/cm) combined with high optical transmittance (>85%) in the visible to near-infrared (Vis-NIR) region[6] .This distinctive combination makes TCOs highly sought after for various applications in modern technologies. They find practical use in devices such as flat panel displays, light-emitting diodes, electrochromic windows, photovoltaic devices, and thin film transistors[7–9] .

In the domain of TCO semiconductors, Zinc Oxide (ZnO) stands out due to its diverse range of properties, attracting significant attention from the scientific community. The following section delves into the fundamental aspects of ZnO, exploring its crystal structure, electrical characteristics, and optical properties.

1.1 Cristal structure

Most of the group II–VI binary compound semiconductors crystallize in either cubic zinc blende or hexagonal wurtzite (Wz) structure where each anion is surrounded by four cations at the corners of a tetrahedron, and vice versa[10].

Among these II–VI binary compound semiconductors, there is ZnO. ZnO exists in three different crystalline forms, namely wurtzite (B4), zinc blende (B3), and rocksalt (B1) structures (See Figure I.1).

At ambient temperature and pressure conditions, a wurtzite ZnO crystal structure is the most common among the three available structures due to its high thermodynamic stability. ZnO normally forms in the hexagonal (wurtzite (B4)) structure (See Figure I.2), with lattice constants a = 3.253 Å, c = 5.213 Å, and a calculated theoretical ratio of c/a = 1.633 (See Figure I.2). In the wurtzite structure, every atom forms tetragonal bonds with four neighboring atoms through sp^3 covalent bonding, which exhibits a significant ionic nature.

rock salt (NaCl) structure may be obtained at relatively high pressure[11]. Wurtzite ZnO can be transformed into rocksalt ZnO if 9 GPa pressure is applied, although its rocksalt structure is rarely found. [12]

On the other hand, the zinc-blende structure can be stabilized only by the growth on cubic structure[11] .

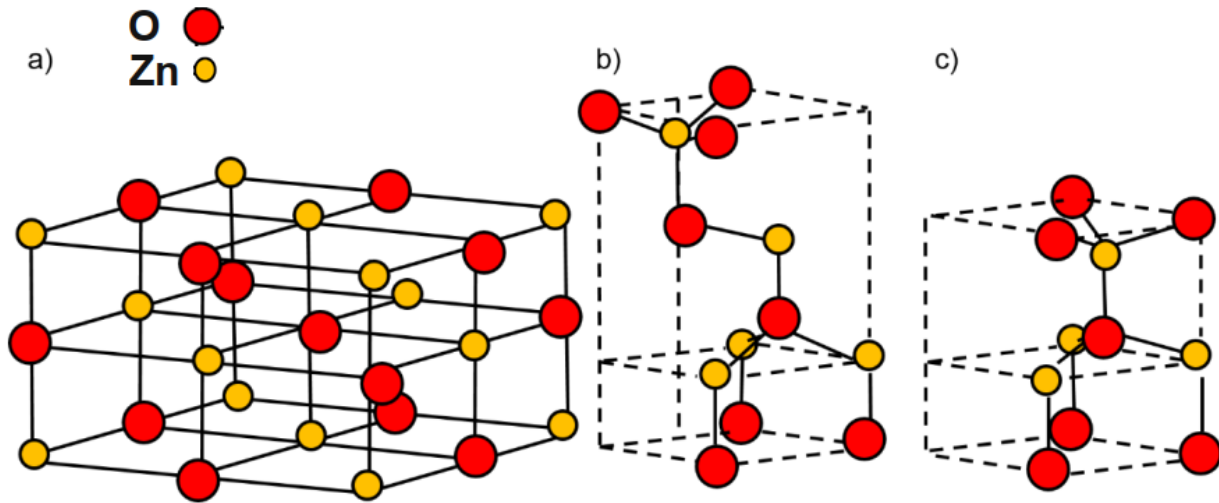

Figure I. 1: ZnO crystal structures: (a) cubic rock-salt (B1), (b) cubic zinc blende (B3), and (c) hexagonal wurtzite (B4).[13]

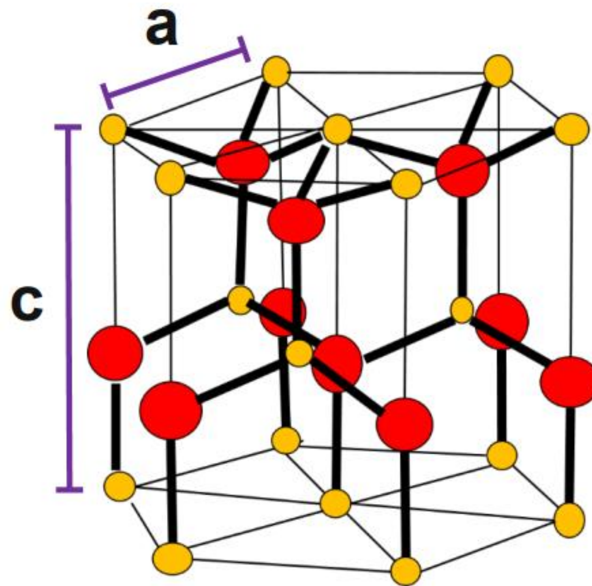

Figure I. 2: ZnO wurtzite structure, also known as B4 type structure (Bravais lattice type)[13] .

Many theoretical calculations have been performed by researchers to calculate the band structure of ZnO crystal[14, 15]. Figure 1.3 Represents the electronic band structure of a Wurtzite ZnO crystal. The precise positioning of Zn 3*d* energy levels was definitively established by employing the local density approximation (LDA) along with the inclusion of pseudo-potentials corrected for

atomic self-interaction (SIC-PP)[16]. Within the context of ZnO, it was observed that both the highest energy point of the valence band and the lowest energy point of the conduction band align at the Γ point (The center of the Brillouin zone) with k = 0. This observation underscores that ZnO exhibits the characteristics of a direct band gap semiconductor.

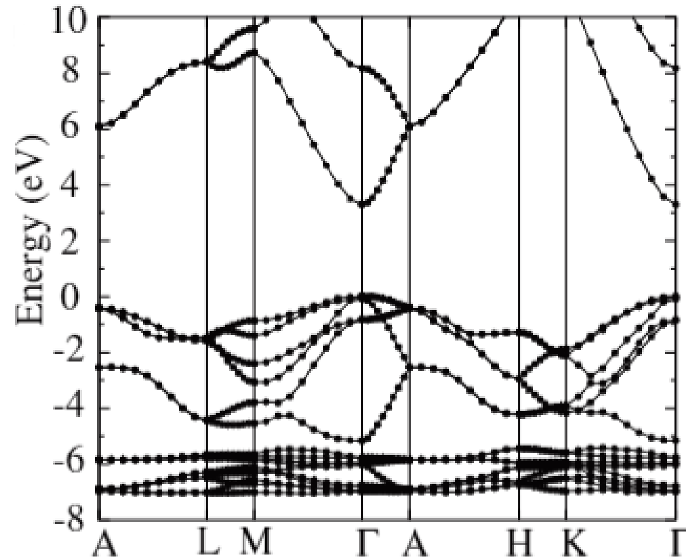

Figure I. 3: The calculated band structure of Wurtzite ZnO using the HSE hybrid functional. The energy of the valence-band maximum was set to zero[17].

1.2 Electrical Properties

The electrical properties of zinc oxide (ZnO) refer to the characteristics and behavior of the material concerning its conductivity, resistivity, and response to an applied electric field. These properties are crucial for understanding and utilizing ZnO in various electronic and optoelectronic applications. Here are key aspects related to ZnO's electrical properties, we can discuss them after the native point defects, which are the main basis for controlling the electrical properties of the material:

1.2.1 Native points defects

Comprehending the characteristics of inherent point defects is vital for the effective utilization of semiconductor materials. These defects play a pivotal role in governing various aspects, including doping, compensation, minority carrier lifetime, and the efficiency of luminescence, either directly or indirectly.

ZnO is inherently an n-type semiconductor material because it contains intrinsic defects like zinc interstitials (Zn_i) and oxygen vacancies (V_O), along with impurities, particularly hydrogen, which function as donor states within the ZnO structure [18]. Figure I.4 shows the various defects present in a crystal, where substitutional defects are atoms of a different element replacing some of the host lattice atoms, interstitial atoms are additional atoms located in positions between regular lattice positions, and Frenkel defects are a cation vacancy and a cation-ion pair.

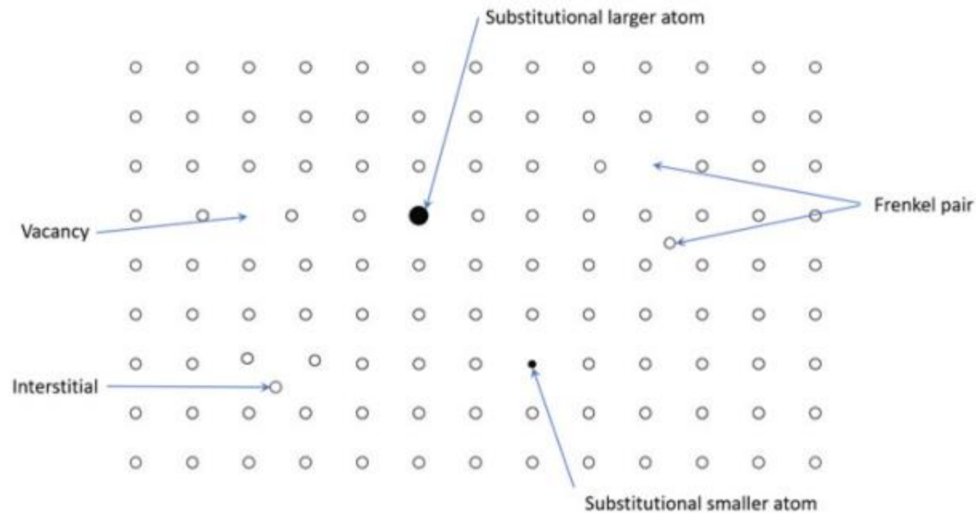

Figure I. 4: various defects present in a crystal.

1.2.1.1 Oxygen and Zinc interstitial (O_i, Zn_i)

In the context of crystal structures, an atom interstitial (O_i or Zn_i) in ZnO refers to an atom that occupies an interstitial position within the crystal lattice, rather than being part of a regular oxygen and Zinc lattice site. An interstitial position is a space between the regular lattice sites of the crystal structure where an atom or ion can be accommodated. The presence of oxygen or Zinc interstitials (O_i, Zn_i) in the crystal structure of ZnO can affect the material's properties, such as its electrical and optical characteristics. atoms interstitials may introduce defects into the crystal lattice, influencing the conductivity and other electronic properties of the material.

1.2.1.2 Oxygen and Zinc vacancies (V_O, V_{Zn})

Zinc vacancy (V_{Zn}), and Oxygen vacancies (V_o) refers to a location within the crystal lattice where zinc (Zn) or oxygen (O) atoms are missing or vacant. Vacancies can occur in crystal structures due to various reasons, including defects during crystal growth or thermal processes.

In ZnO, the crystal structure is often wurtzite, and the zinc atoms are an integral part of the lattice. A zinc vacancy (V_{Zn}) means that one of these zinc atoms is absent. The same goes for oxygen atoms as well. Defects like zinc or oxygen vacancies can influence the material's electronic and optical properties. For example, the presence of zinc vacancies in ZnO may create energy levels within the band gap, affecting the material's conductivity and its response to light.

Understanding and controlling such defects, are essential for tailoring the different properties of ZnO[19], especially, for specific applications like optoelectronics[20], sensors, and transparent conductive coatings. More precise details about the effect of defects on the properties of materials, especially zinc oxide can be found in the literature[21–23] .

1.2.1.3 Concentration of a point defect

The concentration of a point defect depends on its formation energy. In thermodynamic equilibrium and in the dilute regime, the concentration of a point defect is given by[21] [24]:

$$c = N_{sites} exp\left(-\frac{E^f}{k_B T}\right) \tag{I.1}$$

Where E^f is the formation energy, N_{sites} the number of sites the defect can be incorporated on, k_B the Boltzmann constant, and T the temperature.

Formation energy is a thermodynamic concept that measures the energy required or released during the creation of a defect in a crystal lattice. In the context of point defects in a crystalline material, the formation energy quantifies the energy change associated with the introduction of a specific type of defect.

Equation 1 indicates that defects characterized by high formation energies will exist in low concentrations. This relationship is used frequently allowing for giving valuable insights into the behavior and stability of defects in ZnO. Understanding this relationship offers several benefits like: Control of defect concentrations[25], prediction of defect behavior at different temperatures, understanding of material stability…etc.

1.2.2 Scattering charge carriers in ZnO Crystals

At ambient temperatures, one significant factor contributing to scattering is the presence of phonons[26]. Phonons, considered quasi-particles, symbolize quantum units of vibrational energy within a lattice of atoms, exhibiting oscillations at a specific frequency. These phonons can be categorized into two types: acoustic, involving a synchronized motion of atoms, and optical, representing an out-of-phase movement among adjacent atoms. Additionally, the existence of impurities in actual crystals leads to the scattering of charge carriers. Here are some common scattering mechanisms in both single crystals and then thin films:

1.2.2.1 Acoustical Scattering

Acoustical scattering in ZnO crystals is the phenomenon where acoustic phonons, which are the quantized vibrations of the crystal lattice, interact with the electrons in the semiconductor material. ZnO, being a crystalline structure, exhibits mechanical vibrations in the form of acoustic phonons. When electrons traverse the crystal lattice, they can undergo scattering due to their interaction with these acoustic phonons. The collisions between electrons and phonons result in changes to the electrons' momentum and energy, impacting their overall transport properties.

However, lattice deformation scattering induced by acoustic phonons occurs due to a localized energetic shift in the band edges. As explained by Bardeen and Shockley[27], the Hall mobility associated with the acoustical lattice mode can be expressed as:

$$\mu_{H\,ac} = r_{H\,ac} \frac{\sqrt{8\pi}\hbar^4 c_l e}{3E_1^2 \sqrt{m^{*5}\left(kT\right)^3}} \tag{I.2}$$

The Hall coefficient for acoustic phonon scattering, denoted as $r_{\text{Hac}} = 3\pi/8$, involves parameters such as c_l, representing the average longitudinal elastic constant, and E_1, which signifies the energy shift of the conduction band per unit deformation. Although E_1 is not precisely established for ZnO, its impact on the overall properties is relatively minor. This is due to the dominance of optical and piezoelectric scattering phenomena in ZnO, as highlighted in reference[28].

1.2.2.2 Ionized Impurity Scattering

In zinc oxide (ZnO) crystals, ionized impurity scattering refers to the phenomenon where charge carriers, such as electrons or holes, undergo scattering due to the presence of ionized impurities or defects within the crystal lattice. These ionized impurities act as obstacles, disrupting the smooth movement of charge carriers through the crystal. As charge carriers attempt to traverse the lattice, they encounter ionized impurity sites, leading to scattering events that hinder their mobility. This interference results in a reduction in the overall conductivity of the material. Notably, ionized impurity scattering in ZnO crystals is generally independent of temperature, making it a consistent factor influencing charge carrier mobility across a range of temperatures.

Overall, that described process involves the scattering of free carriers by the screened Coulomb potential generated by charged impurities, such as dopants, or defects. This theoretical treatment was first introduced by Conwell in 1946, as documented in references[29].

The mobility of ionized impurities (μ_{Hii}) in nondegenerate semiconductors is expressed by the formula provided in reference[30]:

$$\mu_{Hii} = r_{H_{ii}} \frac{128\sqrt{2\pi}\left(\varepsilon\varepsilon_0\right)^2\left(kT\right)^{3/2}}{\sqrt{m^*}N_i Z^2 e^3 \left[\ln\left(\frac{24m^*\varepsilon\varepsilon_0\left(kT\right)^{3/2}}{ne^2\hbar^2}\right)\right]} \tag{I.3}$$

where n and N_i are the carrier and the impurity concentration, respectively. For N_i it can be written: $N_i = n + 2N_A$, with N_A the acceptor density. $r_{Hii} = 1.933$ is the Hall coefficient for ionized impurity scattering.

1.2.2.3 Neutral impurity scattering

Neutral impurity scattering in a ZnO crystal involves the interaction of electrons with neutral defects or impurities embedded within the crystal lattice. These impurities, which may include foreign atoms or vacancies, introduce localized potential variations in the crystal structure. When electrons traverse the crystal, they experience scattering events due to the presence of these neutral

impurities, leading to changes in their trajectory and energy. The scattering process can influence the overall electrical conductivity and mobility of charge carriers in the semiconductor.

Neutral shallow-impurity scattering is a commonly addressed topic in research papers on transport phenomena in Transparent Conductive Oxide (TCO) films at room temperature, as indicated by references[31]. The mobility resulting from neutral impurity scattering was initially formulated by Erginsoy[32]. Erginsoy's approach involved scaling electron scattering at hydrogen atoms to that within a semiconductor. This scaling was achieved by incorporating the semiconductor's dielectric constant and carrier effective mass, which lead to:

$$\mu_{Hn} = r_{Hn} \frac{m^* e^3}{A(T) 4\pi\varepsilon\varepsilon_0 \hbar^3 N_n} \tag{I.4}$$

In this context, A(T) represents the scattering cross-section factor, and N_n denotes the density of neutral scattering centers.

1.2.2.4 Anisotropic Scattering

In a single ZnO crystal, anisotropic scattering refers to the phenomenon where the scattering of charge carriers varies depending on the crystal direction. This means that the rate at which charge carriers, such as electrons or holes, are scattered by defects, impurities, or phonons differs along different crystallographic axes. Anisotropic scattering is especially noticeable in crystals with marked anisotropic characteristics, where specific crystallographic directions show higher or lower scattering rates than others. This crystal dependence arises from the inherent anisotropy in the material's structure, influencing the behavior of charge carriers and, consequently, the overall electronic properties of the crystal along different directions.

Hutson pioneered the assessment of electrical conductivity in both parallel and perpendicular directions to the c-axis of ZnO single crystals, as documented in his initial report[32]. With a measurement precision of 10%, Hutson determined that the electrical transport in ZnO exhibits isotropic behavior at room temperature.

1.2.2.5 Optical scattering

Optical mode scattering in ZnO crystals is a phenomenon that arises from the interaction between electrons and the electric field induced by lattice vibrations, specifically polar longitudinal-optical phonons. ZnO is a polar semiconductor with partially ionic bonding, meaning there is a significant contribution from ionic forces in its crystal structure. The lattice vibrations, or phonons, induce an electric field due to the displacement of ions within the crystal lattice. When electrons move through the crystal, they can experience a scattering process as they interact with this electric field created by the polar longitudinal-optical phonons. This interaction can lead to changes in the electron's momentum and energy, influencing its behavior within the semiconductor.

Summarily, Devlin[33] suggests that the origin of this scattering process lies in the interaction between electrons and the electric field generated by lattice vibration polarization, specifically polar longitudinal-optical phonons. This phenomenon occurs in polar semiconductors characterized by partially ionic bonding. In accordance with Devlin's findings, the optical Hall mobility can be computed using this framework:

$$\mu_{\mathrm{Hopt}} = r_{\mathrm{Hopt}} \varphi \frac{e}{2\alpha\omega_0 m^*}\left[\exp\left(\frac{\hbar\omega_0}{kT} - 1\right)\right] \quad \text{(I.5)}$$

The polaron coupling constant, denoted as α, is determined by the following:

$$\alpha = \left(\frac{1}{\varepsilon_\infty} - \frac{1}{\varepsilon_{\mathrm{s}}}\right)\sqrt{\frac{m^* E_{\mathrm{H}}}{m_e \hbar\omega_0}} \quad \text{(I.6)}$$

The symbols used in the context are defined as follows: ε_∞ and ε_s represent the high-frequency and static dielectric constants, respectively. E_H denotes the first ionization energy of the hydrogen atom (13.595 eV), $m*$ and m_e stand for the effective and vacuum electron masses, and $\hbar\omega_0$ represents the energy associated with the longitudinal optical phonon (73.1 meV). Additionally, r_{Hopt} represents the Hall coefficient factor for optical mode scattering.

1.2.3 Scattering in thin films

Scattering in zinc oxide (ZnO) thin films can arise from various sources, and understanding these scattering mechanisms is crucial for optimizing the performance of electronic devices based on ZnO thin films. Some of the most common scattering mechanisms in ZnO thin films include:

1.2.3.1 Grain Boundary Scattering

ZnO thin films typically exhibit a polycrystalline nature, composed of small crystalline grains separated by interfaces called grain boundaries. When charge carriers, such as electrons or holes, navigate through these thin films, they inevitably come across these grain boundaries. The scattering mechanism at play involves an abrupt alteration in crystal orientation or lattice structure at these boundaries, leading to the dispersion of charge carriers. This scattering phenomenon impedes the smooth movement of charge carriers through the material, ultimately exerting a notable influence on their mobility. However, Grain boundaries in semiconductors introduce local disruptions to the crystallographic structure, leading to the creation of defects within the semiconductor's band gap. Furthermore, these grain boundaries can act as traps for electrons, resulting in the formation of depletion zones on both sides of the grain. This process is linked to the establishment of a barrier height (Φ_B) for the electrons. Seto[34] developed a model to explain electronic transport in polycrystalline silicon. In his model, he hypothesized that trap states for electrons form a δ-shaped density of states within the band gap, and these states are entirely filled.

According to Seto's model, the effective mobility (μ_{eff}) is predominantly influenced by thermionic emission occurring across the grain boundaries.

$$\mu_{eff} = \mu_0 \exp\left(-\frac{\phi_B}{k_B T}\right) \tag{I.7}$$

The mobility within the grain, denoted as μ_0, is determined according to the expression provided in reference[34].

$$\mu_0 = \frac{e L}{\sqrt{2\pi m^* k_B T}} \tag{I.8}$$

with L being the grain size.

1.2.3.2 Dislocation Scattering

Dislocation scattering is a natural phenomenon occurring in polycrystalline materials, particularly evident in films with a high concentration of crystallographic defects, notably dislocations[35]. In polycrystalline semiconductors, such as transparent conducting oxides, experimental data on carrier transport is rarely explained through this process, despite the intrinsic prevalence of dislocations[36]. ZnO thin films, for instance, can exhibit a substantial dislocation density, reaching approximately 10^{12} cm^{-2}, with an average separation of about 10 nm[37]. These dislocations harbor defects at a density of around 10^{7} cm^{-1}, capable of being charged and influencing carrier scattering.

1.2.4 Zinc oxide electrical conductivity

The electrical conductivity of zinc oxide (ZnO) refers to its ability to conduct an electric current when an electric potential is applied. It is a measure of how easily electrical charges, in the form of electrons or holes, can move through the material. The electrical conductivity is a fundamental property that plays a crucial role in determining the performance of ZnO in various electronic and optoelectronic devices.

The electrical conductivity of thin films can be effectively controlled and enhanced through various factors. In this section, we will explore how these factors influence electrical conductivity, reserving the discussion on electrical mobility for the next section.

Electrical conductivity can be affected by:

Doping

ZnO can exhibit both n-type and p-type conductivity depending on the presence of specific defects and impurities. As we mentioned previously that in its intrinsic or native state, ZnO often shows n-type conductivity due to the presence of defects such as zinc interstitials (Zn_i) and oxygen vacancies (V_o). The n-type conductivity means that electrons are the primary charge carriers.

To achieve p-type conductivity in ZnO, intentional doping with specific impurities is often required. This introduces positively charged "holes" as the dominant charge carriers. Commonly used dopants for achieving p-type ZnO include elements like nitrogen (N), aluminum (Al), and gallium (Ga).

A study conducted by A. Hafdallah and colleagues[38] investigated the impact of dopant elements and their concentrations on the electrical conductivity of zinc oxide (ZnO) thin films produced through the ultrasonic spray technique. In this research, the thin films were doped with indium. The findings revealed that the conductivity of the samples exhibited an increment corresponding to the rise in the doping level, reaching its peak value at 5.3 cm^{-1} with an indium concentration of 6%.

Trilok Kumar Pathak and colleagues[39] conducted a study on Nitrogen-doped ZnO (NZO) thin films synthesized on glass substrates using the sol-gel and spin coating method. The findings revealed that the AC conductivity demonstrated an upward trend with an increase in frequency, reaching a maximum value on the order of 10^{-11} $(\Omega\ cm)^{-1}$.

Annealing

Annealing processes involve heat treatment of ZnO thin films at specific temperatures. Annealing can influence the distribution of defects, improve crystal quality[40], and enhance carrier mobility[41], thereby impacting the overall conductivity.

In a research investigation led by N. Bouhssira et al[42], zinc oxide (ZnO) thin films were fabricated by thermally evaporating ZnO powder. The initially deposited films displayed a dark brown hue, were characterized by a zinc-rich composition, and exhibited low transmittance. Following this, the films underwent annealing in an air atmosphere at different temperatures spanning from 100 to 400 °C.

In another study conducted by Z. Ben Ayadi et al. [40], highly aluminum-doped zinc oxide (ZnO:Al) films were fabricated using radio frequency (rf)-magnetron sputtering at a low temperature employing aerogel nanoparticles. Subsequently, the films underwent an annealing process and were characterized through electrical techniques. The achieved minimum resistivity was 1.17×10^{-3} Ωcm, coupled with a carrier concentration of 7.61×10^{20} cm^{-3}. This favorable result was obtained by annealing the nano powder at 300 °C in an oxygen atmosphere.

Growth Conditions:

The growth conditions during thin film deposition[43], such as temperature, pressure[44], and gas composition, can impact the crystalline structure and defect density of ZnO. Optimizing these parameters can lead to enhanced electrical conductivity.

1.2.5 Zinc oxide electrical mobility

The mobility of a semiconductor, such as zinc oxide (ZnO), refers to the capacity of charge carriers (either electrons or holes) to traverse the material under the influence of an electric field. In the specific case of ZnO, a common semiconductor used in electronic devices, mobility gauges the facility with which charge carriers can drift through the material in response to an applied electric field. Typically measured in units of square centimeters per volt-second ($cm^2/V{\cdot}s$), mobility values are indicative of the material's electrical performance. Higher mobility signifies superior electrical behavior, suggesting that charge carriers encounter less resistance, enabling more efficient movement within the material.

Zinc oxide (ZnO) is widely recognized for its inherent n-type semiconducting behavior, primarily attributed to the existence of two prominent intrinsic defect species: zinc interstitial (Zn_i) and oxygen vacancy (V_o). Achieving p-type properties in ZnO is considerably more challenging[45]. In practice, impurities like hydrogen (H), aluminum (Al), and gallium (Ga) commonly present in commercial sources also contribute to electron doping. Regardless of the donor sources, impurity scattering acts as a limiting factor, impeding electron mobility. [46]

The bulk electron mobility falls within the range of 200–400 cm^2/Vs, primarily restricted by acoustic and phonon scattering. Conversely, in thin films, electron mobility typically falls within the range of 1–100 cm^2/Vs, largely attributed to factors like interface roughness and grain boundary scattering[47].

Various factors, including film quality, crystal structure, defect density, and impurity presence, influence the mobility of ZnO thin films:

Film Thickness

The thickness of the ZnO thin film can impact carrier mobility. In some cases, thinner films may exhibit higher mobility due to reduced scattering effects. In a study conducted by M. Bouderbala and colleagues[48], they investigated the impact of thickness on the structural, morphological, electrical, and optical properties of undoped ZnO thin films. Through the use of r.f. sputtering, films of varying thicknesses were prepared. The results revealed a distinct influence of film thickness on mobility. Specifically, as the thickness increased from 70 to 1800 nm, there was a notable rise in mobility, increasing from 2 to 37 $cm^2/V{\cdot}s$. Conversely, carrier concentration showed minor fluctuations with changes in film thickness, maintaining a relatively constant value of around 10^{20} cm^{-3}. However, a discernible trend toward a decrease in carrier concentration was observed.

In a study led by Kavindra Kandpal et, al [49]. the investigation focused on the structural and electrical characteristics of ZnO thin films deposited through reactive RF sputtering at room temperature, with applications in thin film transistors (TFT). To explore thickness-dependent effects, films of 100, 200, and 800 nm were deposited on a p-type silicon substrate. The thermionic transport model across grain boundaries revealed that, at room temperature, carrier mobility increased for the 800 nm thick ZnO film (4.01 $cm^2.V^{-1}S^{-1}$) due to enhanced grain size compared to the 100 nm (1.07 $cm^2.V^{-1}S^{-1}$) and 200 nm (1.71 $cm^2.V^{-1}S^{-1}$) thick ZnO films, respectively.

Post-Processing Techniques

Employing post-processing techniques, such as laser annealing or ion implantation, can be used to modify the structure and properties of ZnO thin films, affecting carrier mobility[50, 51].

1.3 Zinc Oxide Optical Properties

Zinc oxide's optical characteristics arise from two distinct transition modes: (1) the movement of free excitons between energy levels within the valence band/conduction band of pristine crystals, known as intrinsic excitation, and (2) the transition of bound excitons between discrete energy levels induced by dopants, impurity elements, or defects present in the crystal structure, termed extrinsic excitation.

The distinct UV emission in zinc oxide (ZnO) is widely recognized, and it is commonly attributed to either exciton recombination or the band-edge transition [52] according to previous studies[53]. In addition to the UV emission, ZnO often exhibits a broad green fluorescence, with a central wavelength ranging between 5.6 and 2.5 eV [54]. The origin of this green luminescence is complex, and it may not originate from a single source, as it has been observed in samples produced through various growth methods[17]. Various factors contribute to the emission characteristics of ZnO, and understanding these luminescent features is essential for tailoring its properties in diverse applications.

The origin and mechanisms underlying emissions in the visible regions of zinc oxide (ZnO) have been a subject of extensive study for over two decades, with persistent controversies [55]. In the case of green emissions, commonly associated with intrinsic or extrinsic defects in ZnO, various hypotheses have been proposed, although none have been definitively proven[56]. Among these hypotheses are associations with oxygen vacancies or zinc interstitials. Some proposed mechanisms include transitions between singly ionized oxygen vacancies and photoexcited holes[57], transitions between electrons near the conductive band and deeply trapped holes at oxygen vacancies (V_O)[58], and the involvement of surface defects[59]. Despite these proposed hypotheses, a clear understanding of the luminescence centers and the luminescence mechanism for green emissions in ZnO remains elusive, highlighting the need for continued research and investigation in this area.

The green luminescence observed in zinc oxide (ZnO) has been attributed to zinc vacancies (V_{Zn}), which act as acceptors and are likely to form in n-type ZnO [17]. Sekiguchi et al conducted experiments supporting V_{Zn} as the source of the green luminescence [60]. They reported a significant reduction in green luminescence following hydrogen plasma treatment, indicating a

strong passivation effect. This observation aligns with the hypothesis that V_{Zn}, acting as an acceptor, can be passivated by hydrogen[61].

In contrast, previous studies have suggested oxygen vacancies as the cause of the characteristic green luminescence in ZnO. Oxygen vacancies typically exhibit three charge states: the neutral oxygen vacancy (V_O), the singly ionized oxygen vacancy (V_O^+), and the doubly ionized oxygen vacancy (V_O^{2+}). These vacancies are positioned below the bottom of the conduction band (CB) in the series of V_O^0, V_O^+, and V_O^{2+}, from top to bottom. The position of different defect levels is illustrated in Fig. I.5.

These findings highlight the ongoing debate in the literature regarding the specific origin of green luminescence in ZnO, with some studies pointing to zinc vacancies and others suggesting oxygen vacancies. The experiments by Sekiguchi et al[60], demonstrating the passivation of green luminescence by hydrogen treatment, provide additional support for the role of zinc vacancies in this phenomenon.

The visible emission in zinc oxide (ZnO) primarily arises from electronic transitions between levels near the conduction band edge and defect-associated trap states. According to Vanheusden et al. [68], this emission is predominantly linked to defect states, specifically oxygen vacancies and zinc interstitials. Transition involving zinc vacancies has been reported to result in blue emission, often in conjunction with oxygen antisite (O_{Zn})[62]. However, it's worth noting that the latter is an acceptor-type defect characterized by a considerably high formation energy, even under favorable oxygen-rich conditions[70].

Green emission is commonly attributed to ionized oxygen vacancies[71]. Finally, the red emission observed in ZnO can be associated with the presence of oxygen interstitials (O_i) and neutral oxygen vacancies (V_o). These defect-related emissions play a significant role in the optical properties of ZnO and are crucial for various applications.

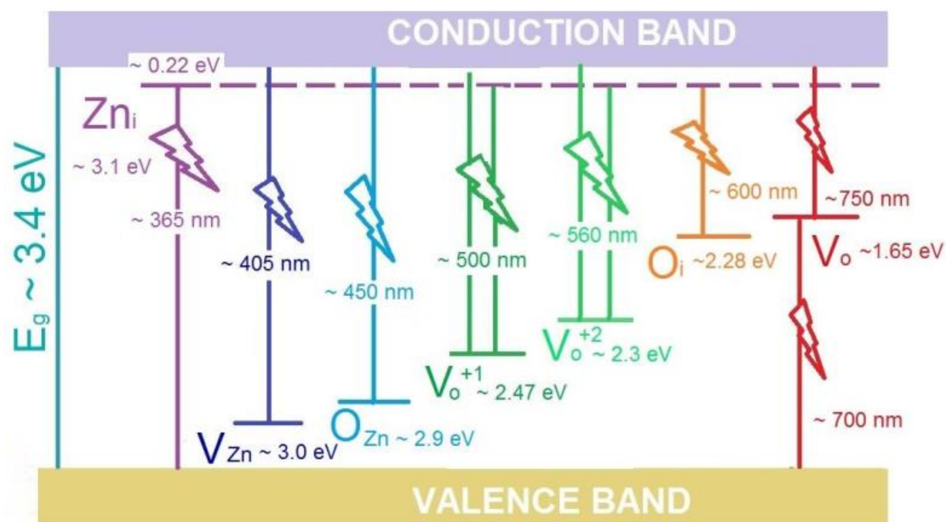

Figure I. 5: Diagrammatic energy depicting the potential radiative transitions of zinc oxide caused by various levels of defects, E_g = energy gap, Z_{ni} = zinc interstitial, V_{Zn} = zinc vacancy, O_{Zn} = oxygen interstitial, V_o^{+1}, V_o^{+2}, and V_o are= oxygen vacancies, O_i^- = oxygen interstitial [64].

2 Application of ZnO

Zinc oxide (ZnO) holds significant importance in optoelectrical applications, leveraging its unique properties for a range of technological advancements. As a wide-bandgap semiconductor, ZnO plays a crucial role in the development of optoelectronic devices. Its notable characteristics, including transparency in the visible spectrum, high electron mobility, and the ability to emit light, make it ideal for applications such as light-emitting diodes (LEDs), laser diodes, photodetectors, and transparent conductive films, and some other applications as see in Figure I.6.

Figure I. 6: Applications of ZnO in different fields[65].

We will briefly consider some of these applications.

2.1 Solar cells

Recent years have seen a growing interest in the development of transparent conducting oxide-based photovoltaic cells. These oxides offer the potential to create high-performance photovoltaic cells suitable for large-scale terrestrial applications[66]. Transparent conducting oxides bring several advantages to photovoltaic cells technology[74]:

- Enhanced Sensitivity: The transparent conductive film allows for the direct transmission of solar radiation to the active region with minimal loss, resulting in improved sensitivity to high-energy photons in the solar spectrum.
- Simplified Fabrication: Lower junction formation temperatures make the fabrication of these photovoltaic cells easier and more efficient.
- Dual Functionality: These films can serve as both low-resistance contacts to the junction and anti-reflective coatings for the active region, streamlining the photovoltaic cells design.

This development holds promise for more efficient and practical solar energy harvesting.

Figure I.7 depicts the benefits of employing ZnO as the active material in solar cell applications. Zinc oxide (ZnO) materials are characterized by their wide bandgap semiconducting properties, featuring a band gap ranging from 3.1 to 3.3 eV. This bandgap confines light absorption primarily to the UV region. To broaden their light absorption into the visible spectrum, ZnO can be combined with materials possessing smaller energy gaps, including dye sensitizers, organic polymers, and semiconductors with narrower band gaps.

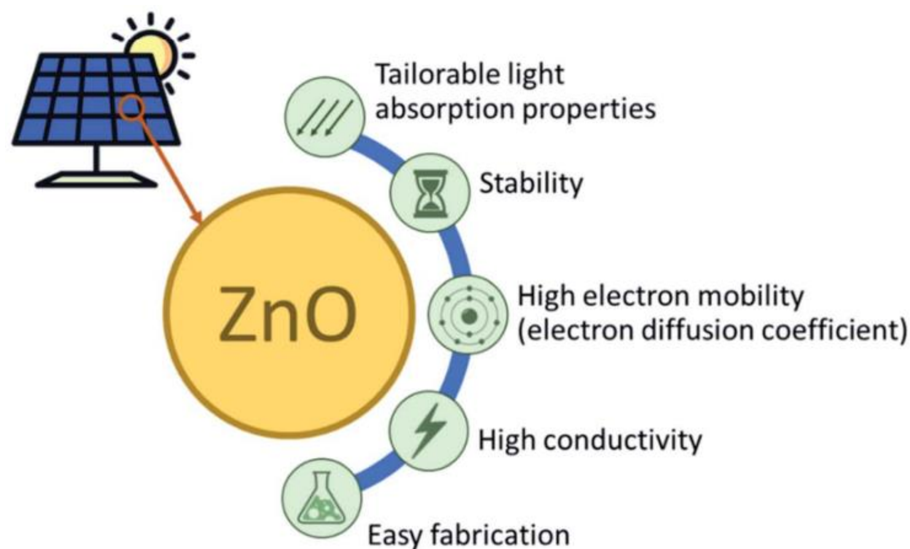

Figure I. 7: The advantages of ZnO for solar cell application.[66]

In the field of photovoltaics, Zinc Oxide (ZnO) has found extensive application in various emerging solar cell devices, including perovskite solar cells, kesterite-based devices, quantum dot solar cells, dye-sensitized solar cells, and organic solar cells[76] [77]. Figure I.8 illustrates (a) Using ZnO in emerging solar cells and (b). the trend in the number of published papers over recent

years, specifically focusing on utilizing ZnO in diverse emerging photovoltaic technologies. There is a noticeable upward trend in the number of published papers, particularly in the realms of perovskites, kesterites, and organic photovoltaics.

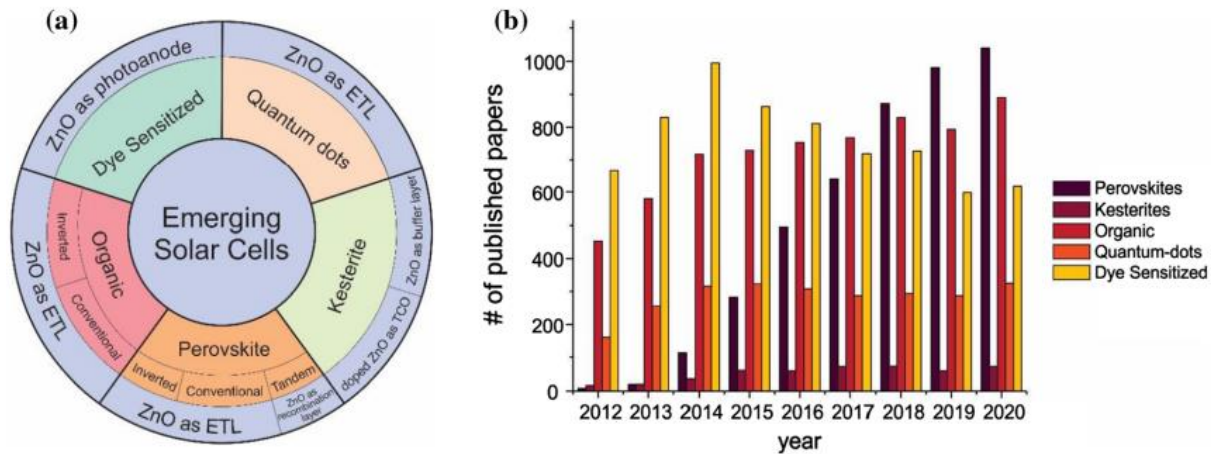

Figure I. 8: (a) illustrates the application of ZnO in nascent solar cell technologies, and (b) the quantity of research papers associated with ZnO in emerging solar cell technologies.[78]

2.2 Light Emitting Diodes

Drapak[70], in 1967, pioneered the fabrication of one of the earliest, if not the first, ZnO-based hybrid heterostructure light-emitting diodes (LEDs). In this groundbreaking work, Drapak employed Cu_2O as a p-type layer, achieved through the thermal oxidation of a deposited Cu metal layer on ZnO substrates grown via vapor phase methods. The resulting LED structures exhibited electroluminescence under both forward and reverse biases, showcasing broad spectra with peak emissions observed at 540 nm.

But now, the basic composition of LED lights based on zinc oxide is completely different from before. we will take a quick look at the most important recent developments in the aspects of heterogeneous and homogeneous ZnO LEDs.

- *heterojunction light-emitting diode*

A heterojunction light-emitting diode (LED) refers to a type of LED that incorporates a heterojunction, which is a junction between two different semiconductor materials. In a heterojunction LED, the interface between these dissimilar semiconductor materials plays a crucial role in the device's operation.

Roberto Macaluso et al. [80]conducted a study on advancements in ZnO/GaN-based LEDs, incorporating high-thickness GaN layers in the p-region and employing a customized device topology. Heterojunction LEDs were created by depositing a quasi-coalesced, non-intentionally doped ZnO nanorod layer using chemical bath deposition onto a metal–organic vapor-phase epitaxy-grown epitaxial layer of p-doped GaN. The fabrication of circular LEDs emitting violet

light, featuring a remarkably small p-n contact distance of 3 μm, was achieved. These LEDs demonstrated a turn-on voltage of 3 V and emitted optical power at 395 nm within the range of a few microwatts.

In a study conducted by Yu Huang et al. [81], heterojunction light-emitting diodes (LEDs) were developed based on n-ZnO/CsPbBr3/p-GaN using pulse laser deposition (PLD). The impact of the CsPbBr3 interlayer on the electroluminescence (EL) performance of n-ZnO/p-GaN was thoroughly examined. The results revealed the significant influence of the CsPbBr3 interlayer on the emission performance of the heterojunction LED. By varying the thickness of the CsPbBr3 interlayer, the emission peaks of the heterojunction LED were observed to shift from violet to greenish-yellow. This suggests that the electroluminescence characteristics can be precisely adjusted by manipulating the CsPbBr3 films.

- *Homojunction (Light-Emitting Diode)*

In a homojunction LED, the semiconductor material used for both the p-type and n-type regions is the same in this case, ZnO. Typically, a homojunction LED is constructed by creating a p-n junction within a single semiconductor material.

The first-ever homojunction UV light-emitting diode (LED) incorporating both p-type and n-type ZnO nanoparticles (NPs) has been successfully developed by Islam M. Shafiqul et al. [82]Nitrogen-doped ZnO and gallium-doped ZnO NPs were utilized to create the p-type and n-type NP layers, respectively. The fabricated LEDs possess structures of p-ZnO/GZO and p-ZnO/n-ZnO/GZO. These devices exhibit near-UV electroluminescence (EL) at room temperature, and the emission power is doubled with the incorporation of the n-ZnO NP layer. Through a comprehensive analysis of I–V characteristics, EL, and photoluminescence results for the LEDs, it is established that holes inject from the p-ZnO NP layer to the n-ZnO NP layer, confirming the mechanism of these devices as that of p-n junction LEDs.

Gaohang He et al.[83] conducted a study in which they synthesized individual microwires of antimony-doped ZnO (ZnO:Sb) demonstrating consistent and reliable p-type conduction. The researchers achieved adjustable p-type conduction characteristics by varying the weight ratios of Sb2O3 in the precursor mixtures. These ZnO:Sb microwires functioned as emitting filaments, displaying electroluminescence (EL) with wavelength tunability when subjected to bias. The researchers utilized these microwires to fabricate homojunction light-emitting devices, characterized by excellent diode properties. The resulting p–n junction exhibited strong near band edge emissions, predominantly centered at 400 nm.

2.3 Transparent Film Transistors (TFT)

While silicon (Si) has demonstrated its dominance in the realm of thin-film transistor (TFT) technology through amorphous and polycrystalline Si, an emerging interest is focusing on its optically transparent counterpart, known as transparent thin-film transistor (TTFT) technology [84], [85], Among these materials from which it is made is zinc oxide. These nearly invisible TTFTs hold significant potential for diverse applications where transparency is a crucial requirement, especially in commercial and military contexts. For example, when incorporated into

automobile windshields, they could facilitate the transmission of visual information, effectively turning ordinary glass into a multifunctional electronic device, thereby enhancing security systems and expanding their utility.

Numerous research groups have delved into the realm of transparent electronics, generating over 541 papers from 2001 to 2010[86]. The sheer volume of publications during this period restricts the feasibility of a precise and detailed analysis of the collective work. To provide an overview of the scientific output, Figure I.9 illustrates the progression of published papers specifically focusing on n-type oxide-based TFTs from 2001 to 2010.

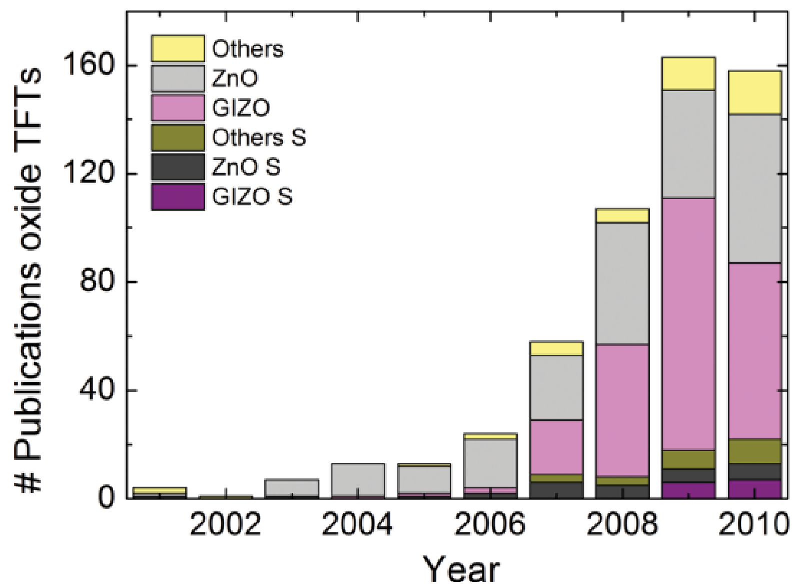

Figure I. 9: depicts the annual publication trend of papers related to oxide TFTs.[86]

Analyzing about 200 papers on GIZO TFTs unveils two main findings. Firstly, sputtering dominates as the primary deposition technique, representing over 90% of cases. Secondly, GIZO TFTs can be grown at temperatures below 150 °C, ensuring acceptable electrical performance. However, comparing TFT characteristics poses challenges due to substrate variations, diverse dielectric materials, and varying interfaces. Differences include non-patterned channel layers and specific layouts where source/drain electrodes completely overlap the channel layer [84].

A Zinc Oxide Thin-Film Transistor (ZnO TFT) typically comprises a ZnO channel, a gate dielectric, and three electrodes: the source, drain, and gate[85]. The TFT structure can be classified as either coplanar or staggered based on the relative positions of the source and drain with respect to the channel. In a coplanar structure, the source and drain are on the same side of the channel, while in a staggered structure, they are on opposite sides.

There are variations within these structures, including bottom and top gate configurations. In a bottom gate structure, the gate electrode is positioned beneath the channel, while in a top gate

structure, the gate electrode is located on top of the structure. The most common topology for ZnO TFT is the staggered bottom gate configuration.

To illustrate, if the source and drain are on opposite sides of the ZnO channel, creating a staggered arrangement, and the gate electrode is positioned beneath the channel, it represents a staggered bottom gate ZnO TFT. This configuration is depicted in Figure I.10, providing a schematic view of one of the prevalent ZnO TFT topologies.

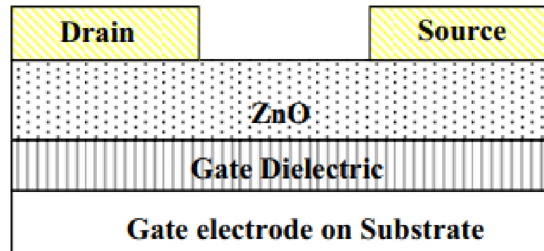

Figure I. 10: Zinc oxide thin-film transistor (TFT) with a bottom gate configuration.

Critical electrical parameters used to evaluate the performance of thin-film transistors (TFTs) include the 'on-to-off ratio of drain current' and the 'mobility of the active channel.

In recent years, development in transparent zinc oxide transistors has reached very significant improvements compared to previous years. As is clear in the following research [87-93].

2.4 ZnO Sensors:

Zinc oxide (ZnO) is a versatile material that has been employed in various sensor applications due to its unique properties. Here are some types of sensors created with zinc oxide:

2.4.1 Gas Sensors

ZnO is widely used as a gas sensing material for detecting the toxic and harmful gases because of its superior physicochemical properties. and becomes currently a research hotspot for detecting the toxic and harmful gases [94]

In the study of gas sensing properties, the morphology control of materials has an important impact on gas sensing performance.

The most common type of MOS-based gas sensor uses a resistance type transducer, which detects the adsorption of different gases according to the change of resistance [95]

ZnO gas sensors are widely used for detecting gases such as CO (carbon monoxide), NOx (nitrogen oxides), H2 (hydrogen), and VOCs (volatile organic compounds). The performance of the gas sensor is often assessed by investigating several parameters such as gas response (R), response and recovery times, operating temperature, the concentration of the analyte, and detection limit of n the sensor [96]

Many factors could affect the sensor performance ZnO-based materials, including various structure and property parameters. The structural parameters mainly contain morphology, size and porosity. The response of the sensor is determined by the interaction between the adsorption oxygen and the target gas. By increasing the specific surface area, the high adsorption oxygen content can be achieved. The adsorption oxygen content is conducive to promoting the redox reaction between oxygen molecules and gas molecules, which improves the sensing response of the sensing material. Reducing the grain size of the material improves its sensitivity by limiting charge conduction. Porosity could contribute to the material selectivity due to small molecules diffusing into the material. Therefore, the morphology and structure of the material has a significant effect on the gas sensitive property[97]

2.4.2 Chemical Sensors

Zinc oxide (ZnO) finds application in chemical sensors designed to detect alterations in chemical compositions, serving purposes in environmental monitoring and industrial processes. ZnO-based sensors have garnered global attention as they exhibit a notable response rate to chemical toxins along with exceptional selectivity and sensitivity, making them significant contributors to the development of cost-effective sensors [98]. The high photoelectric reaction, coupled with admirable chemical and thermal stability in ZnO nanomaterials, positions them as promising candidates for the preparation of effective chemical and biological sensors [99].

The process of nano structuring ZnO in various shapes has further enhanced its properties, allowing for a range of applications and facilitating device miniaturization [100][92]. Among different metal oxide materials, ZnO is extensively employed in crafting sensors for hazardous chemicals due to the conductive nature of ZnO nanostructures and their high chemical and thermal strength under operational conditions. Notably, researchers have utilized vertically aligned nanorods of ZnO for modifying electrode surfaces in hydrazine estimation [102]. Ibrahim et al. demonstrated a highly sensitive and selective electrochemical sensor for phenyl hydrazine using Ag-doped ZnO nanoflowers [103], while Umar et al. reported the application of ZnO nano-urchins for sensory electrodes in the recognition of phenyl hydrazine via the current-voltage (I–V) technique[104].

Recent developments include Ahmad et al.'s creation of a binder-free, highly reactive, and sensitive chemical sensor for detecting p-nitroaniline using ZnO nanoparticles[105], where ZnO nanorods modified a fluorine-doped tin oxide (FTO) electrode. Cheng et al. tested thin films of ZnO-based nanoparticulate for sensing ethanol and propyl alcohol molecules, achieving higher sensitivity and selectivity for the tested molecules[106]. Furthermore, Arshak and Gaiden demonstrated the capability of thick films of ZnO-based nanostructures to simultaneously detect ethanol and propanol. Ongoing research in this field continues to explore and advance the capabilities of ZnO-based chemical sensors.

2.4.3 Pressure Sensors

The roots of pressure sensor development can be traced back to 1954, marked by the discovery of compressive resistance effects in silicon and germanium by Smith[98]. The surge in intelligent robots and wearable electronic devices has fueled the rapid development of new flexible pressure sensors. These devices find applications in entertainment, gaming, automotive, consumer electronics, industries, healthcare, and other fields [108]. The perception mechanisms of flexible pressure sensors can be categorized into piezo resistivity, capacitance, and piezoelectricity[109], [110].

Zinc oxide (ZnO) is ideal for pressure sensors due to its piezoelectric properties, which allow it to generate an electric charge in response to mechanical stress, facilitating pressure detection.

Sensors based on the piezoresistive effect involve the distortion of the composite material through external force, altering the distribution and contact status of conductive fillers and resulting in a regular change in composite resistance (as depicted in Figure I.11). Notably, these sensors do not necessitate a complex sensor structure. Their advantages include low power consumption, a wide pressure testing range, and a straightforward manufacturing process, making them extensively researched compared to capacitive and piezoelectric pressure sensors. Applications for piezoresistive sensors span medical examinations, sealing inspections, physical exercise monitoring, and more [102, 103]. Commercial products, such as smart bras capable of monitoring heartbeats by detecting resistance variations, exemplify the practical implementation of these sensors in the market.

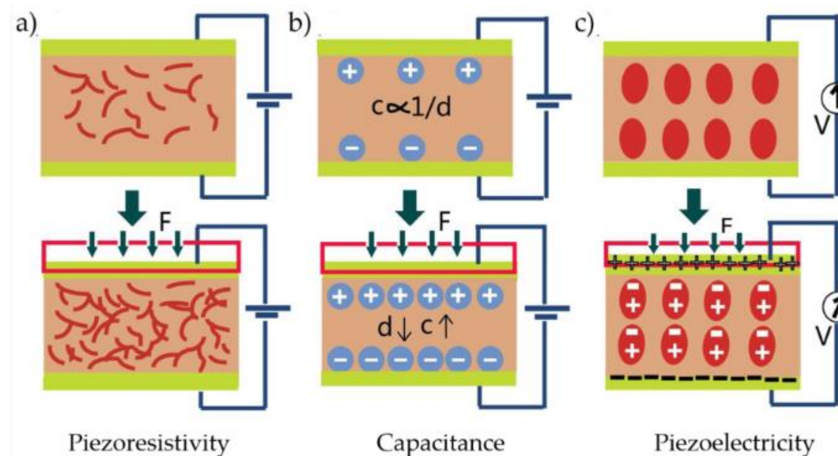

Figure I. 11: depicts a schematic representation of three prevalent transduction mechanisms alongside representative devices: (a) piezoresistivity, (b) capacitance, and (c) piezoelectricity.[104]

In a study conducted by Victor K. Samoei et al. [114], a pressure sensor was created and assessed using an aluminum-doped zinc oxide (AZO) thin film deposited on polyethylene (PE) substrates through a rf magnetron sputtering method. The resistance of the AZO film exhibited a notable

increase with rising pressure applied to the PE/AZO diaphragm, whether in tensile or compressive modes. This sensor demonstrates the capability to quantitatively measure pressure under both vacuum and gauge pressure conditions, offering high reproducibility and repeatability.

2.4.4 UV Sensors

Thin film ZnO presents an appealing option for UV sensing due to its wide and direct band gap, positioned in the near UV spectral region, and an extended photo-carrier lifetime. Traditional silicon-based photodetectors are commonly used for UV light detection, but they exhibit sensitivity across the visible and infrared regions, with relatively lower sensitivity in the UV range due to silicon's lower band gap (1.1 eV at room temperature). Solid-state detectors utilizing wide band gap materials like ZnO showcase superior performance for UV ray detection .

ZnO nanowires/nanorods (NWs/NRs) UV sensors, in particular, demonstrate enhanced electrical properties owing to their high surface-to-volume ratio, facilitating efficient electron-hole pair generation and recombination upon UV stimulation [116]. UV sensors typically operate by detecting changes in electrical resistance upon exposure to UV radiation. The presence of highly adsorbed electrons contributes to remarkably high sensitivity, characterized by significant resistance differences between light-off and light-on conditions [117].

The challenge of p-type doping in ZnO limits the fabrication of ZnO p–n junction-based UV sensor devices. Consequently, ZnO metal–semiconductor–metal (MSM) devices have gained considerable attention, adopting either a Schottky-barrier-based photovoltage type or a photoconductive type for UV sensing [118]. Schottky barrier-type detectors are highly efficient in UV sensing, offering rapid response and low noise performance, making them ideal for applications in space. ZnO photoconductive type devices, on the other hand, are easy to fabricate and exhibit high responsivity and photo current gain.

MSM UV sensors incorporating ZnO nanostructures, as illustrated in Figure I.12, operate based on a distinctive principle. In a dark environment, oxygen molecules capture free electrons, forming a depletion region. Upon UV illumination, ZnO absorbs UV light, exciting electrons from the valence band to the conduction band, generating electron-hole pairs. Photo-induced hole pairs have holes trapped at oxygen-related hole-trapping states, typically located at the nanostructure's surface. The imbalance in the number of electrons and holes reduces the recombination rate. The remaining electrons are either re-adsorbed to the oxygen molecules at the surface, aggregated at the anode, or recombine with the ionized hole[109, 110].

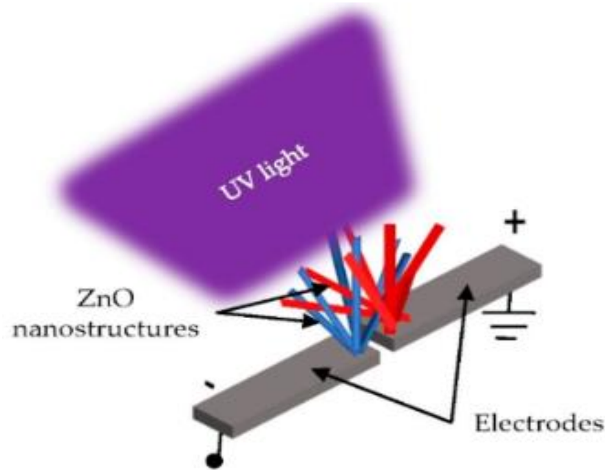

Figure I. 12: Schematic diagram of UV sensor with ZnO nanostructures, bridge network.[121]

3 Deposition techniques

Today's considerable improvements in industrial and electrical devices are mostly attributable to breakthroughs made in a critical field known as deposition techniques. To improve the quality and complexity of thin films for solid-state devices, electronic engineers have continuously worked to advance deposition technology. The desire for better and more affordable deposition methods, as well as for in-situ process monitoring and control tools to measure film attributes, has been effectively met by equipment manufacturers. The increased understanding of the physics and chemistry pertaining to films, surfaces, interfaces, and microstructures is another important element speeding up the development of deposition technology. The extraordinary developments in analytical instrumentation during the past few decades have enabled this insight.

Many deposition techniques exist to shape materials [122]. But we will focus here on thin film deposition methods only. Thin-film deposition technologies can be categorized into two main types: purely physical methods, such as evaporative techniques, and purely chemical methods, including gas- and liquid-phase chemical processes (See Fig. I.13). In this part, we will define the two types with some examples.

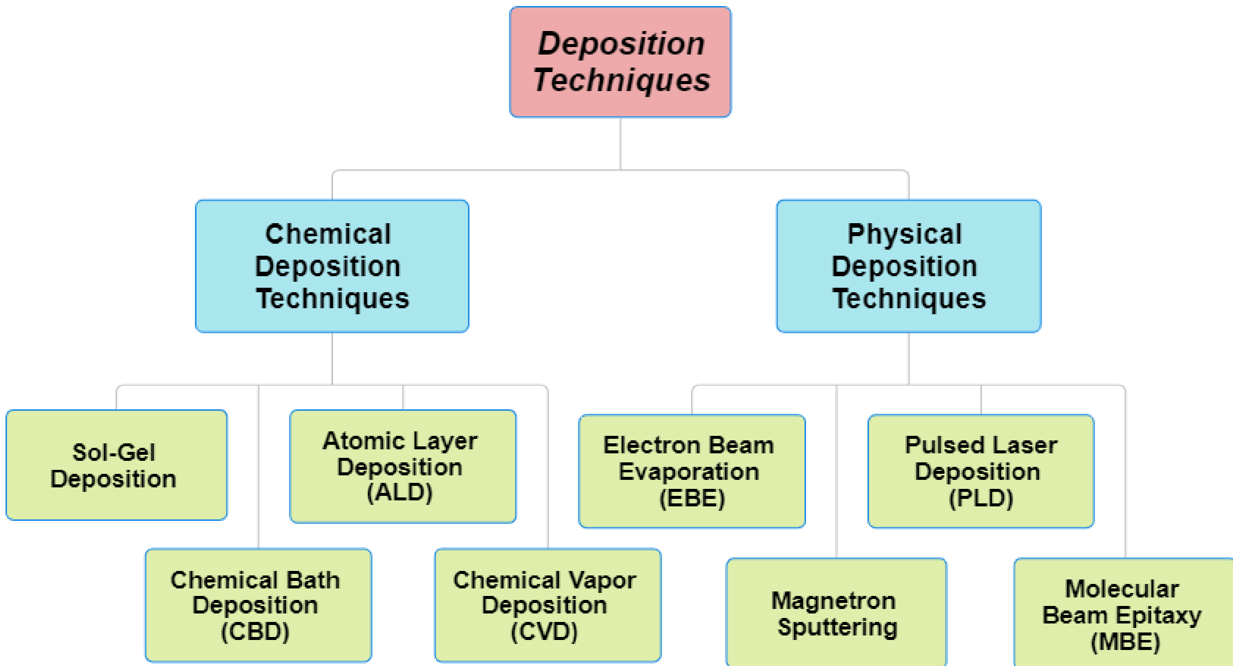

Figure I. 13: Thin film deposition techniques.

3.1 Chemical deposition techniques

Chemical deposition techniques, alternatively known as chemical deposition processes, encompass a varied array of manufacturing methods employed for depositing thin films, coatings, or layers of different materials onto a substrate through meticulously controlled chemical reactions. These methodologies capitalize on chemical reactions between precursor substances to accomplish the intended material deposition and film growth. Essential features of chemical deposition techniques involve the utilization of chemical reactions, frequently within a controlled environment, to produce thin films with specific attributes, including composition, thickness, crystallinity, and structure.

Chemical deposition plays a vital role in the fabrication of semiconductors [123], optoelectronic devices, protective coatings, sensors, catalysts, and a multitude of other advanced materials and components. These techniques enable the development of materials with tailored properties, making them indispensable in modern manufacturing and research.

These techniques include a wide range of processes, from vapor phase methods such as chemical vapor deposition (CVD) and atomic layer deposition (ALD) to solution-based methods such as chemical bath deposition (CBD) and gel deposition. Which we will present in the following paragraphs

3.1.1 Chemical Vapor Deposition (CVD)

Chemical Vapor Deposition (CVD)[114, 115] stands as a significant technique for producing thin films of semiconductor materials.

In this method, one or more gaseous compounds react with a solid substrate's surface. The vapor, containing the material to be deposited, is transported to the substrate's surface, where it undergoes decomposition, often through a heterogeneous process [74]. The nature of this decomposition process varies depending on the composition of the volatile transport species.

It is crucial to ensure that the decomposition occurs primarily at or near the substrate surface and not in the gaseous state to prevent the formation of powdery deposits, which could lead to film haziness. This preservation of film quality is essential for semiconductor applications.

The distinctions in precursor materials lead to variations in the CVD process, enabling the precise growth and control of semiconductor thin films for various technological applications.

Within the realm of the chemical vapor deposition (CVD) technique, various technical variants exist, including Plasma-Enhanced (PECVD), Low-Pressure CVD (LPCVD), Atmospheric Pressure (APCVD), and Ultrahigh Vacuum (UVCVD).

One of the researchers employing one of those techniques is M. Purica et al [126]. In their work, transparent and conductive ZnO thin films were fabricated through a chemical vapor deposition method, utilizing Zn $(C_5H_7O_2)_2$ as Zn source. Where, highly transparent (bigger than 80%) and conductive ($\rho=10^{-4}$ Ωcm) ZnO films have been prepared by a SSCVD technique using Zn acetylacetonate as source.

3.1.2 Atomic Layer Deposition (ALD)

Atomic layer deposition (ALD) is an advanced thin film deposition method that operates on the principles of alternating saturative surface reactions. Unlike many other chemical vapor deposition techniques, ALD employs a distinctive approach wherein source vapors are introduced into the reactor sequentially, one at a time, with purging or evacuation periods in between. During each exposure step, the surface becomes saturated with a monomolecular layer of the introduced precursor. ALD operates through cycles involving alternating reactions, with each cycle depositing a single (see Fig. I.14). The thickness of the resulting film is directly correlated with the number of ALD cycles executed, providing meticulous control over the growth of the film.

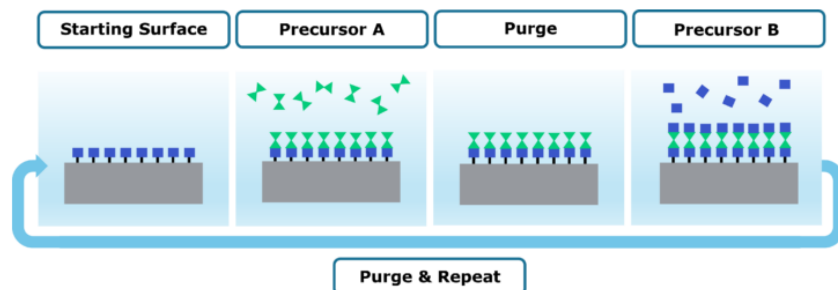

Figure I. 14: Cycle of ALD deposition.

This intricate process results in a self-limiting film growth mechanism, characterized by several advantageous attributes.

ALD is known for its exceptional conformality and uniformity, ensuring that the deposited film precisely follows the contours of the substrate. Moreover, it offers straightforward and precise control over film thickness. These unique characteristics make ALD a highly regarded technique in the realm of thin film deposition, particularly in applications where precision and uniformity are paramount.

This technology has many advantages, including[127]: Accurate and simple thickness control, Large-area capability, Large-batch capability, Excellent conformality, High quality materials are obtained at low processing temperatures, Capability to prepare multilayer structures in a continuous process. This technique offers the flexibility to deposit various thin films, depending on the range of materials available, including ZnO, as demonstrated in the work by Zhengning Gao et al. [128], which explores the atomic layer deposition of doped ZnO films.

3.1.3 Chemical Bath Deposition (CBD)

This wet chemical method for depositing different materials' thin films onto substrates is called Chemical Bath Deposition (CBD). This process works especially well for growing materials like zinc oxide (ZnO) [129], which is used in semiconductor devices, photovoltaics, and optoelectronics.

Making a chemical bath using precursor chemicals is the first step in the creation of CBD. Usually, the components needed for film deposition are present in metal salts or complexes, which serve as precursor compounds. For instance, zinc oxide (ZnO) is prepared by reacting a zinc salt with an oxygen source, usually ammonia or amine. Sources of sulfur and cadmium are used for CdS.

Figure I.15 illustrates the primary setup of the Chemical Bath Deposition (CBD) system, where the substrate, which can be made of silicon, glass, or other materials, is immersed in a chemical solution .The material to be deposited and the particular application will determine which substrate is best.

The required substance is formed by a reaction between the precursor chemicals in the bath and immersion. The substrate's presence facilitates this reaction, which takes place at the substrate's surface. Depending on which particular precursor chemicals are employed, the precise chemical

reactions can be highly complicated. A small layer of the target material begins to form on the substrate as the chemical reactions continue. Because the growth is self-limiting, the concentration of the precursor chemicals and the length of the immersion can regulate the thickness of the film. The substrate is usually washed with a solvent to eliminate any remaining chemicals once the appropriate film thickness is reached, and then dried. The final film sticks to the surface of the substrate. Among the many benefits of CBD are its broad range of substrate coating options and comparatively low equipment requirements. It can be difficult to get exact control over layer thickness and homogeneity, and the process might take longer than with some other deposition processes.

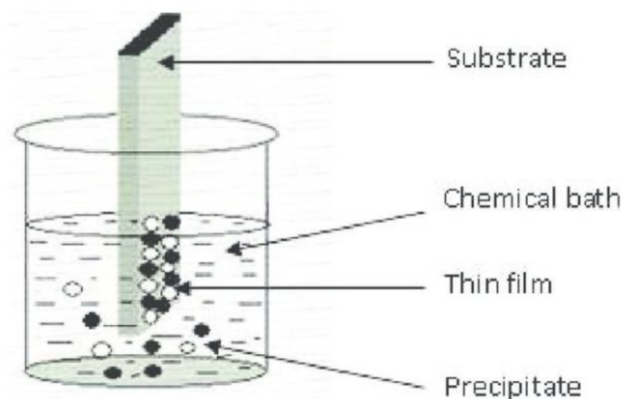

Figure I. 15: Schematic of Chemical Bath Deposition.

3.1.4 Sol-Gel Deposition

Sol-gel coating stands out among various techniques due to several advantages. This method operates at low processing temperatures [130], making it a cost-effective choice [131].

Sol-gel procedures involve the use of a solution (sol) or gel containing precursor chemicals, which can be sprayed, dip-coated, or spin-coated onto a substrate. The process is quite straightforward. Thin films are formed by the precursor components reacting during drying or heat treatment. The first step is to create a solution containing the desired precursor, either an oxide or a non-oxide. Applying this solution to a substrate can be done by draining, dipping, or spinning. This procedure is noteworthy because it allows a coating to be applied simultaneously to the inside and exterior surfaces of complicated forms.

The resultant films usually have a consistent thickness of approximately one micron and show homogeneity over a sizable surface area while adhering firmly to the substrate. The fact that this equipment is affordable should be emphasized, particularly in view of the fact that deposition methods requiring vacuum settings are more expensive. Furthermore, a variety of materials, including metals, polymers, and ceramics, can be coated with these coatings.

These coatings are typically applied at ambient temperature. It is important to note, nevertheless, that a large number of them require additional heating—also known as calcination—in order to improve density and structure. This adaptable process may produce coatings with amorphous or

crystalline properties, offering versatility for a range of uses. High homogeneity, low temperature, and high purity are the general benefits of the sol-gel technique [132].

The price of raw materials is one drawback, and while drying, there is frequently significant volume shrinkage and cracking (we have to get rid of the "organics").

Sol-gel processes are versatile and can be used to create thin films of various materials, including ZnO [133], ZnS.

Various widely-used sol-gel deposition techniques include Dip Coating [134], Spray Pyrolysis, and Sol-Dipping. Figure I.16 illustrates a specific Sol-Gel technology known as Spin Coating.

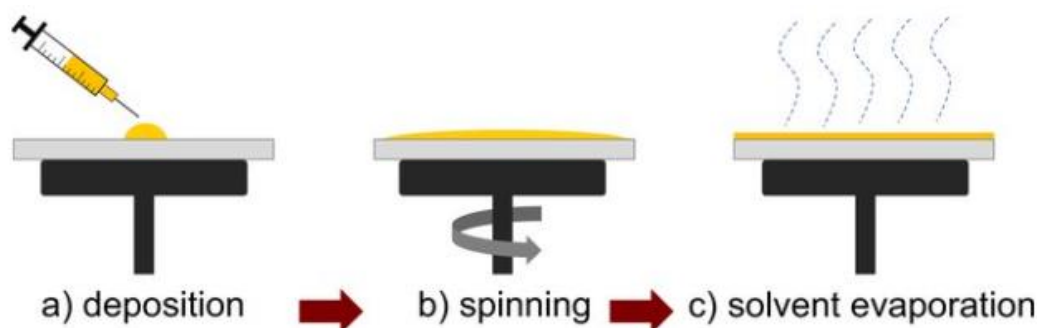

Figure I. 16: Schematic illustration of the spin coating process.

3.2 Physical Deposition Techniques

Physical deposition techniques, often called physical vapor deposition (PVD) techniques or physical deposition procedures, are a broad class of manufacturing processes used to precisely apply coatings or thin films made of different materials onto a substrate. These methods make use of physical processes like condensation or atom-by-atom deposition to accomplish the required layer growth and material deposition. Physical deposition focuses primarily on the physical transformation of material from a source to a substrate, as opposed to chemical deposition techniques, which rely on chemical reactions between precursor ingredients. These techniques are essential in many different fields, including as surface engineering, materials science, electronics, and optics.

3.2.1 Electron Beam Evaporation (EBE)

Electron Beam Evaporation (EBE)[136] is a highly precise and controlled thin-film deposition technique commonly used in materials science and semiconductor device fabrication. The process involves the use of an electron beam to heat a solid material source, which leads to its vaporization. This vaporized material is then deposited onto a substrate, forming a thin film. that technique was used in several types of semiconductors to elaborate thin films, like AZO[137],

EBE starts with a solid material source, typically in the form of a small, precisely shaped pellet or crucible. This source material is the substance from which the thin film will be deposited. It can be a pure element or a compound, depending on the desired thin-film composition. The heart of the EBE system is an electron gun, which generates a focused beam of high-energy electrons. This

electron beam is directed at the solid material source. When the high-energy electrons from the electron gun strike the material source, they transfer their energy to the source material. This sudden input of energy results in the vaporization of the source material. As a result, atoms or molecules of the source material are converted into a vapor or gas phase. The vaporized material is then directed toward the substrate, which is typically placed in close proximity to the material source. The vapor condenses onto the substrate's surface, forming a thin film. The film grows atom by atom or molecule by molecule, allowing for precise control over the film's thickness and composition. Figure I.17 is an illustrative representation of this process.

Advantages of electron beam evaporation include high purity, precise control, uniformity, and wide material compatibility.

Overall, Electron Beam Evaporation is a versatile and effective technique for producing thin films with high precision, making it valuable in industries where fine control over film properties is essential.

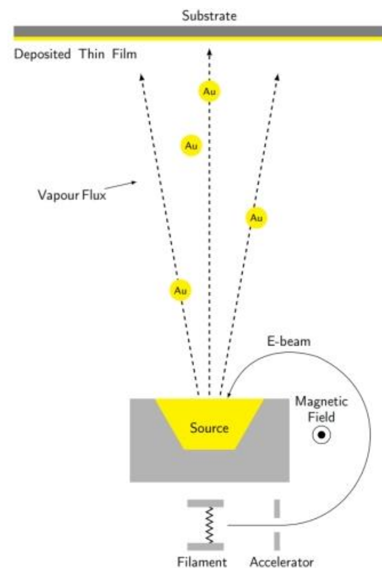

Figure I. 17: e-beam evaporation system.[138]

3.2.2 Magnetron Sputtering

Magnetron sputtering is a physical vapor deposition (PVD) technique widely used for thin film deposition in various industries and applications. In this process, a magnetically enhanced plasma is utilized to sputter material from a target (source) and deposit it onto a substrate, forming a thin film. The key components of magnetron sputtering include a vacuum chamber, a target material, and a substrate (See Fig. I.18).

Here's an overview of the magnetron sputtering process:

Vacuum Chamber [139]*:* The process takes place in a vacuum chamber to create a low-pressure environment. This ensures the absence of air and other contaminants that could interfere with the thin film deposition.

Target Material [140]*:* The material to be deposited as a thin film is placed in the form of a target within the vacuum chamber. This target can be composed of various materials such as metals, alloys, or ceramics, depending on the desired properties of the thin film.

Substrate [141]*:* The substrate, onto which the thin film will be deposited, is carefully positioned within the vacuum chamber. Substrates can be made of glass, silicon, or other materials, depending on the application.

Magnetron Configuration: A magnetron, typically placed behind the target, generates a magnetic field. This field confines electrons near the target surface, enhancing the efficiency of the sputtering process.

Plasma Generation [142]*:* A low-pressure gas, such as argon, is introduced into the vacuum chamber. Radiofrequency (RF) power or direct current (DC) power is applied to the target material, causing ionization of the gas and the formation of a plasma. The positively charged ions in the plasma are accelerated towards the negatively charged target (cathode), leading to the ejection of target atoms or molecules.

Thin Film Deposition: The sputtered target material travels through the vacuum chamber and deposits onto the substrate, forming a thin film. The control of deposition parameters, such as pressure, power, and temperature, allows for precise control over the thin film properties.

Magnetron sputtering is favored for its ability to produce high-quality thin films with good adhesion, uniformity, and thickness control. It is widely used in the semiconductor industry, optics, electronics, and various other fields where precise thin film coatings are essential. This method is popular and applicable to a wide range of materials like silicon [143], ZnO[144], ZnS[145].

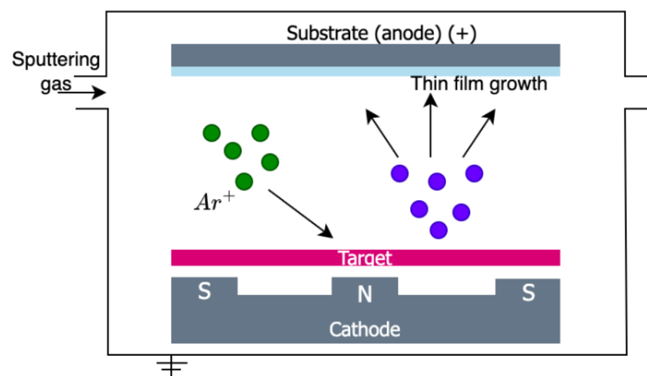

Figure I. 18: Schematic illustration of magnetron sputtering method.

3.2.3 Pulsed Laser Deposition (PLD)

Pulsed laser deposition (PLD) is considered one of the more advanced techniques for depositing transparent semiconducting oxides like ZnO [135, 136]. In recent times, it has gained prominence as a method of choice for fabricating crystalline thin films characterized by exceptional crystallinity.

Short, high-energy laser pulses are used in the PLD process to evaporate a solid target inside a high vacuum or ultra-high vacuum chamber. The target surface is exposed to a pulsed laser beam, which causes it to evaporate. The evaporated material then condenses onto a substrate to form a film that is chemically identical to the target material. The extremely fast heating of the target surface—heating rates as high as 10^8 Kelvin per second—caused by the pulsed laser irradiation is the cause of this amazing congruence in evaporation. The target will evaporate uniformly as a result of this quick heating, regardless of the particular evaporation points of its constituent parts or compounds.

Compared to other film development methods, PLD has the unique ability to create crystalline films while keeping substrate temperatures far lower. These properties prevent temperature degradation of the semiconductor material and the underlying integrated circuit.

A PLD system's main parts usually consist of a vacuum chamber, optics, and a laser. The procedure includes the creation of a plasma plume comprising extremely energetic species in addition to the physical contact between the solid target and the high-power pulsed laser. The transfer of the ablated material onto the substrate surface is greatly aided by this plasma plume.

PLD targets are far smaller than those employed in sputtering techniques, providing more flexibility in the production of multi-layered films made of multiple materials by sequentially ablation of different targets. Furthermore, by varying the number of laser pulses, exact control over film thickness can be obtained, even at the level of individual atoms in a monolayer. The main principles and PLD system are summarized in Figure I.19.

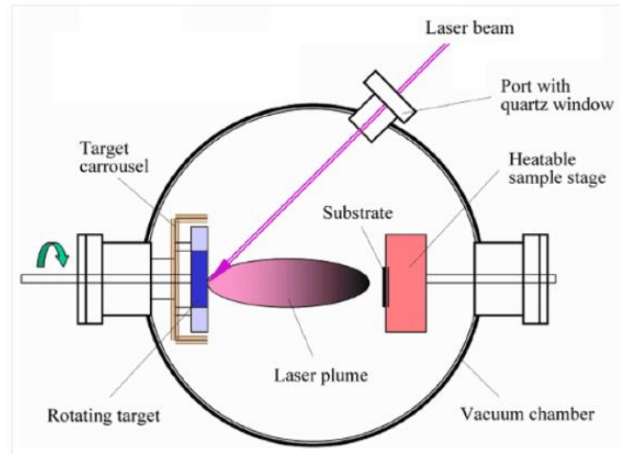

Figure I. 19: Schematic diagram of the pulsed laser deposition system.

Chapter II： Experimental techniques of measurement and methods

1 Introduction

During this study, we used some equipment, techniques, and methods for the optoelectrical characterization of samples. In this chapter, we will present different equipment and methods used, such as:

- Magnetron sputtering: It is the main technique we rely on in thin film deposition
- Ellipsometry technique: used for optical thin film characterization.
- Hall method: used for electrical measurement of thin film material
- Spectrophotometry: Was employed to derive some features delineating the impact of samples on incident light rays, including absorption...
- Birouk's model of refractive index: On its basis, the index of refraction was studied

2 Spectroscopic ellipsometry

Ellipsometry, pioneered over a century ago by Drude [137], is now primarily associated with the Drude model, which bears his name. The distinctive aspect of ellipsometry lies in its ability to ascertain samples' optical constants (refractive index, n, and extinction coefficient, k) by analyzing alterations in light polarization during reflection[138].

This study places significant reliance on this particular technique, especially within the context of this study. The equipment of ellipsometry that has been used in measurements (thickness, Ψ and Δ spectrum) is (*SENTECH SE 850*).

Spectroscopic ellipsometry (SE) is a highly regarded and precise characterization method that offers non-destructive and non-contact assessment. Its prominence arises from its fundamental principle, which revolves around the alteration in the polarization of light as it interacts with a sample, whether through reflection or transmission. This change in polarization allows extracting valuable properties from the sample under investigation. [139]

As a well-established technique, ellipsometry quantifies two essential parameters: the amplitude ratio, often expressed as tan Ψ, and the phase difference denoted as Δ, between light waves (See Figure II.1). The Ψ and Δ spectra are obtained by varying the wavelength of light, encompassing the ultraviolet-visible and infrared regions.

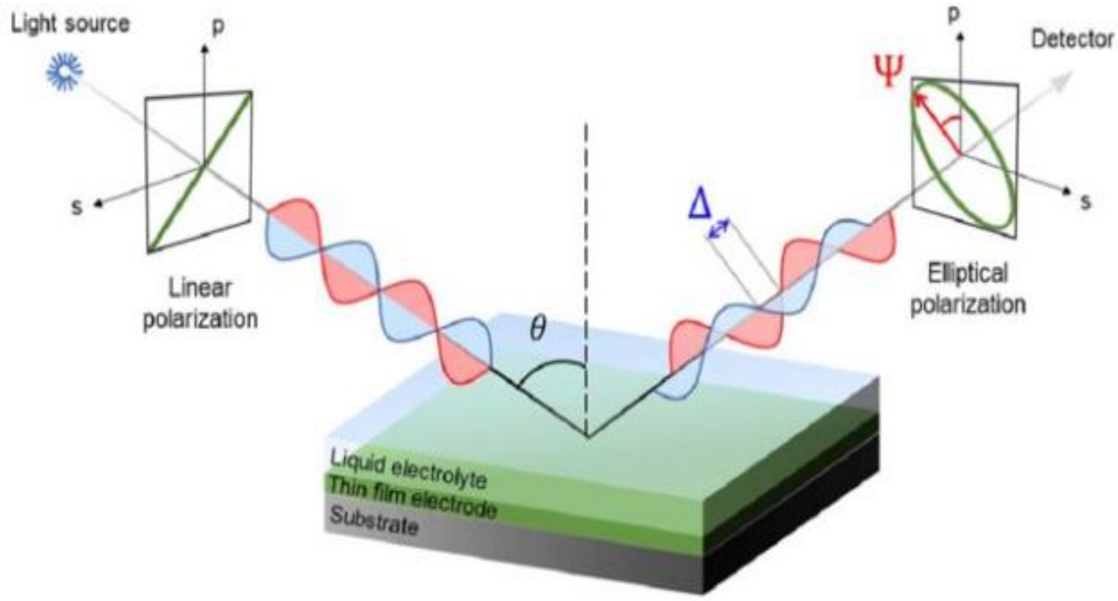

Figure II. 1: The ellipsometry measurement is depicted using incident linearly polarized light aligned with both p- and s-components. When this light interacts with the sample, it results in distinct amplitudes and phase shifts for the reflected p- and s-polarizations, ultimately generating elliptically polarized light. Ψ is the amplitude by degree, and Δ the phase difference by degree. [140]

The fundamental equation of ellipsometry that contains Ψ and Δ is [141, 142]:

$$\rho = \frac{R^p}{R^s} = \tan\psi \, e^{i\Delta} \tag{II.1}$$

Where ρ, R^p, R^s are the complex Fresnel reflection coefficient ratio, the Fresnel reflection coefficient of perpendicular and parallel wave components, respectively. The expression of this latter is related to layer number [141]. In our case, the samples were modelized with 3 layers model (air, AZO thin film, substrate). So, R^p and R^s are given by:

$$R^p = \frac{r_{12}^p + r_{13}^p \exp(-2i\,\beta)}{1 + r_{12}^p r_{23}^p \exp(-2i\,\beta)} \tag{II.2}$$

$$R^s = \frac{r_{12}^s + r_{13}^s \exp(-2i\,\beta)}{1 + r_{12}^s r_{23}^s \exp(-2i\,\beta)} \tag{II.3}$$

Where the quantities r_{ij}^{p}, r_{ij}^{s}, β, are the complex Fresnel reflections ratio for p-polarized, and s-polarized waves, and the complex coefficient, respectively.

What's remarkable about ellipsometry is its capability to perform both in-situ and ex-situ measurements, even from a remote location, making it particularly valuable for scrutinizing thin-film fabrication in confined areas.

To obtain on characteristics of thin film by SE it must pass through steps (we call by modeling process).

2.1 Data analysis procedure

Several important processes are involved in the modeling process in spectroscopic ellipsometry[143], as shown in Figure II.2. These steps are as follows:

Measurement: In this first stage, experimental data are gathered by measuring the ellipsometric parameters, usually psi (Ψ) and delta (Δ), at different wavelengths throughout a wide variety of spectral ranges. For this thesis, visible and near-infrared wavelengths are included in the measurement.

Modeling: At this point, a model is created to depict the sample's optical characteristics. Each layer or component of the model has its own distinct optical properties, such as thickness, extinction coefficient, and refractive index. The properties of the material and the necessary level of analytical precision determine the complexity of the model.

***Fitting*:** Finding the best-fitting model that most closely resembles the experimental data is the aim of this stage. In order to reduce the discrepancy between the observed and computed ellipsometric parameters (Ψ and Δ), the model's parameters must be adjusted. The goal of this optimization procedure is to provide the optical characteristics of the sample that are as exact as possible.

***Result*:** Critical information regarding the optical properties of the sample is provided by the final model, which is adjusted to best suit the observed data. This might comprise surface layers' or thin films' thickness, refractive index, and other material characteristics. The acquired data are crucial for comprehending and describing the sample, and they may be highly useful in domains such as surface research, materials science, and the semiconductor industry.

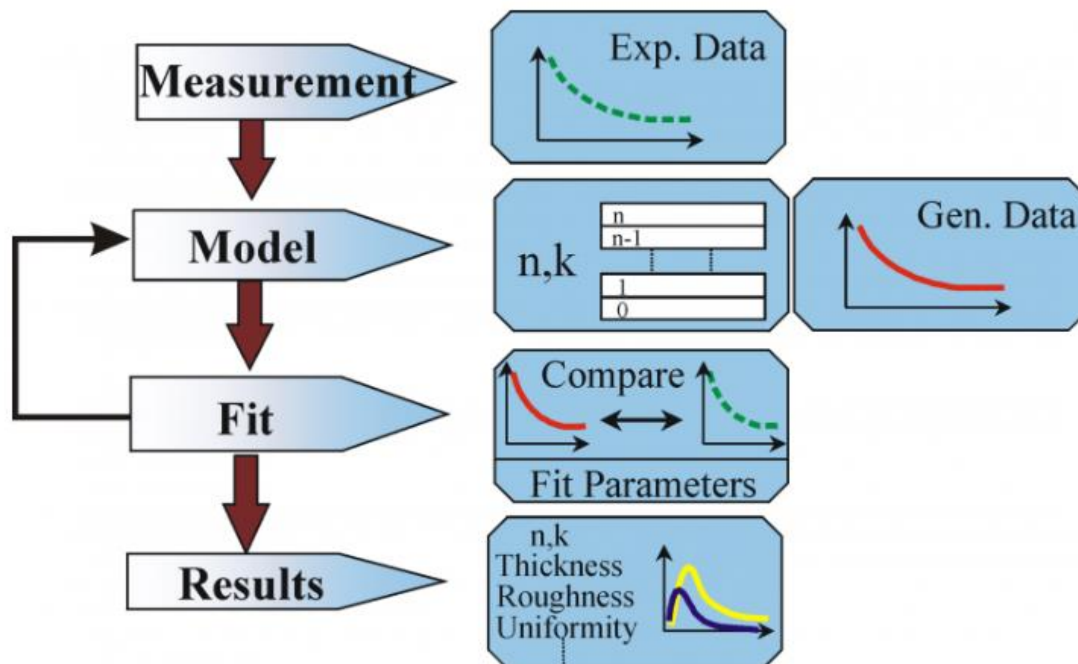

Figure II. 2: Flow chart of the data analysis procedure. Taken from ref [144].

2.2 Application of spectroscopic ellipsometry

Spectroscopic ellipsometry is a valuable method employed for the evaluation of optical constants and the determination of thin film thickness in various samples. Figure II.3 illustrates the diverse array of physical properties that can be extracted by employing spectroscopic ellipsometry.

The figure presented here offers an overview of characterization through ex-situ measurements. In this context, ex-situ measurements are those performed after the completion of sample preparation or processing.

Data analysis in ellipsometry enables the extraction of vital physical properties, notably the optical constants and the sample's film thickness. Ellipsometry distinguishes itself from traditional methods, like reflectance and transmittance measurements, by directly measuring key optical constants, such as the refractive index (n) and the extinction coefficient (k). The complex dielectric constant and absorption coefficient can also be obtained. These optical constants are essential for a comprehensive understanding of the material's optical characteristics.

Additionally, by utilizing the optical constants and film thickness data, one can compute the reflectance (R) and transmittance (T) at varying angles of incidence. This proves especially valuable in examining interbond transitions or band structures, particularly within the ultraviolet/visible spectral region. Notably, the bandgap (Eg) can be inferred from the variations in these parameters concerning photon energy (hv).

Understanding band structures is essential too, as they tend to exhibit changes contingent on factors like surface temperature, alloy composition, phase structure, and crystal grain size. These vital properties can also be ascertained through a thorough spectral analysis of optical constants, making spectroscopic ellipsometry an indispensable tool for in-depth material characterization.

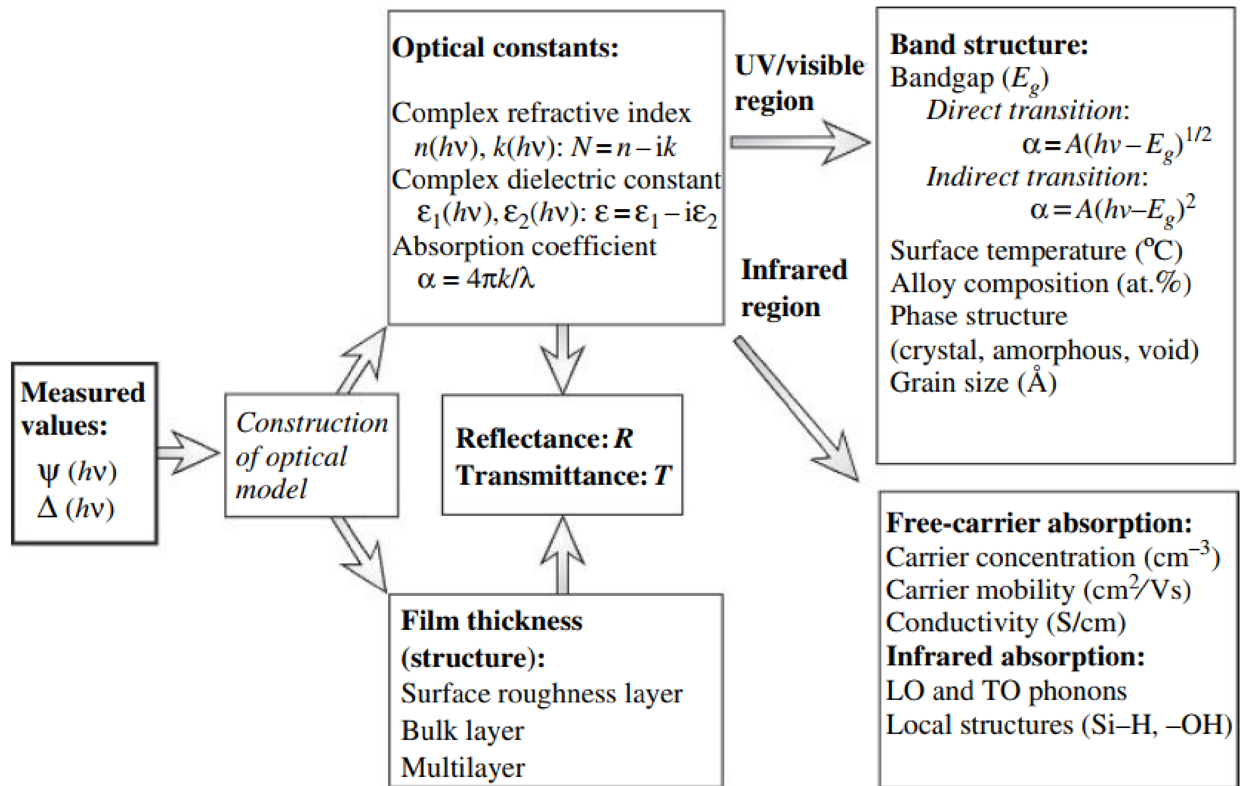

Figure II. 3: Characterization of physical properties by spectroscopic ellipsometry[139]

2.3 Advantages and drawbacks of spectroscopic ellipsometry

Spectroscopic ellipsometry technical has many benefits. Positively, it offers exceptional thickness sensitivity of about 0.1 Å along with great accuracy. Since the technique is nondestructive, measurements may be made without compromising the sample's integrity. Spectroscopic ellipsometry is a time-efficient option because of its reputation for quick measurements. Its extensive use with a variety of materials demonstrates its adaptability. The method enables various characterizations, such as optical constants and film thicknesses, and facilitates feedback controllable real-time monitoring.

Spectroscopic ellipsometry can have certain disadvantages, though. An optical model is necessary for its data interpretation, which adds an element of indirect characterization. Because of this, the analytical process may become complex and time-consuming. Spectroscopic ellipsometry has a rather limited spatial resolution, with a typical spot size of several millimeters. Furthermore,

precisely describing materials with low absorption coefficients below 100 cm^{-1} may provide difficulties for the approach [145].

Notwithstanding these drawbacks, the benefits of the approach frequently exceed the drawbacks, particularly in situations where accuracy and nondestructive analysis are crucial.

3 Spectrophotometry

A spectrophotometer is an instrument used to quantify the intensity of light absorbed or transmitted through a sample material, which may also involve scattering or reflection. In this thesis, the equipment employed is the Specord 200 PLUS from Analytic Jena.

The underlying principle of this technique revolves around measuring both the transmission (T) and reflection (R) of the sample, subsequently allowing for the calculation of the sample's absorbance (A) using the formula A = 1 - T - R. Absorbance is a crucial parameter that can be linked to the electronic properties of the sample, such as its band gap. Essentially, when a photon possesses enough energy to promote an electron from the valence to the conduction band, it will be absorbed by the sample. Conversely, if the photon's energy falls short of activating this transition, it will not be absorbed, resulting in sample transparency.

The Transfer Matrix Method (TMM [146]) was applied to align the experimental curves (R and T) for the determination of key material parameters. Through this method, the thickness (d), real refractive index (n), and extinction coefficient (k) of each material were obtained with precision.

3.1 Absorption coefficient

Optical absorption spectra play a crucial role in characterizing semiconducting materials, providing fundamental insights into their composition and optical bandgap.

The optical absorption spectra and the optical absorption coefficient (α) should be studied here. There are several ways to calculate the absorption coefficient, including the following:

- The absorption coefficient (α) can be determined from the corrected transmittance T(λ), and corrected reflectance R(λ), by using the Berr-Lambert law. The final formula is like [147]:

$$\alpha(\lambda)=\left(\frac{1}{d}\right)\ln\left[\frac{\left(1-R^{2}\right)}{2T}+\sqrt{\frac{\left(1-R\right)^{4}}{4T^{2}}+R^{2}}\right] \tag{II.4}$$

Where *d* is the film thickness, which in our case is constant.

This method has been used particularly with AZO thin films. Since, the reflectance of thin films were somewhat low. This made applying the relationship easier when the reflection was close to zero.

- The absorption coefficient (α) can be determined from the extinction coefficient (k) by the following equation [148]:

$$\alpha = \frac{4k\pi}{\lambda} \tag{II.5}$$

where λ is the incident radiation wavelength.

When the reflection and transmission of ZnO thin films were measured, the refractive index along with the extinction coefficient were estimated by TMM. Thanks to the previous formula, the absorption coefficient (α) was estimated typically for all ZnO samples.

The relation between the absorption coefficient (α) and the incident photon energy ($h\nu$) can be determined by using Tauc's relationship in the high absorption region of the semiconductor. The *Tauc plot* is a method originally developed to derive the optical gap of amorphous semiconductors such as amorphous zinc oxide or silicon [149].

The fundamental Tauc's relationship is as follows:

$$(\alpha h\nu)^{\frac{1}{n}} = K\left(h\nu - \mathrm{E_g}\right) \tag{II.6}$$

Where K is the proportionality factor, sometimes called the band tailing parameter, which is an energy-independent constant, h is the Planck constant, v is the incident photon frequency, and Eg is the band gap energy.

The value of the exponent n depends on the nature of the electronic transition [150]:

- for direct allowed transitions: n = 1/2
- for direct forbidden transitions: n = 3/2
- for indirect allowed transitions: n = 2
- for indirect forbidden transitions: n = 3

Usually, the primary absorption processes are governed by allowed transitions, resulting in either n = 1/2 for direct transitions or n = 2 for indirect transitions. As for ZnO n= 1/2, the relationship becomes like follows:

$$(\alpha h\nu)^2 = K\left(h\nu - \mathrm{E_g}\right) \tag{II.7}$$

To extract the band gap energy E_g, one must plot the evolution of $(\alpha hv)^2$ as a function of the energy hv (see Figure II.4), produce a linear fit to the $(\alpha hv)^2$ curve, and know when the line intersects the axis hν where, when $(\alpha hv)^2=0$, the band gap energy $E_g = hv$.

The Tauc's relation is not valid when $hv < Eg$ because $(\alpha hv)^2$ cannot be negative. the energy hv is not sufficient to free an electron and create a hole-electron pair

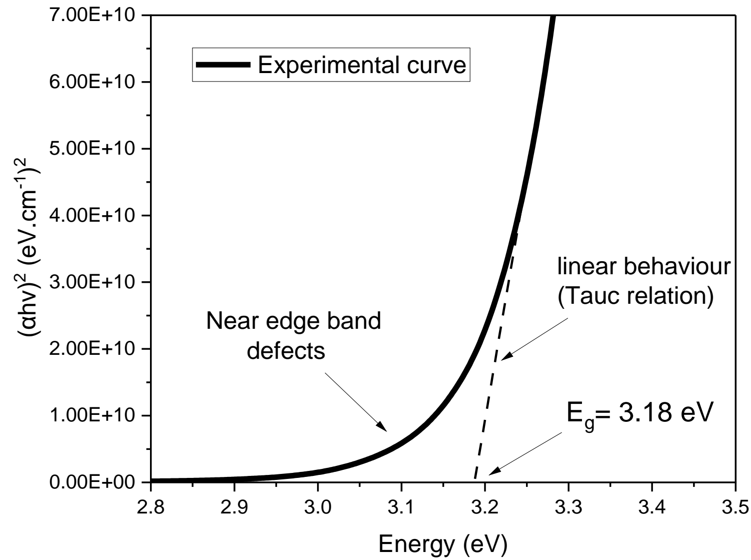

Figure II. 4: Explanation of the Tauc-plot method on the curve level thanks to the absorption coefficient.

There are many mechanisms for absorbing light by semiconductors. We will point out two of them related to our study. These mechanisms are related to the type of energy that can be extracted through them, such as:

- Gap energy: related to the interbond (fundamental) absorption mechanism. Bandgap energy can be extracted by Tauc's method, as we see previously.
- Urbach energy (absorption band tail width): It is related to the two absorption mechanisms; absorption through the crystal lattice, and doping absorption.

The Urbach energy is a quantity used in the analysis of absorption edges in the electronic structure of semiconductors and insulators. It is also known as the Urbach tail or Urbach edge. It bears the name Leonard E. Urbach in honor of the physicist who originally reported this phenomenon. The exponential rise in transmittance or absorbance close to a material's absorption edge is characterized by Urbach energy. It gives information about the disorder and structural defects in the material's bandgap and is mathematically related to the breadth of the tail in the exponential absorption tail of the material. A more organized and less faulty material is indicated by a lesser Urbach energy. For a clearer comprehension, refer to Figure II.5, which succinctly illustrates the Urbach tail concerning both energy and density of states.

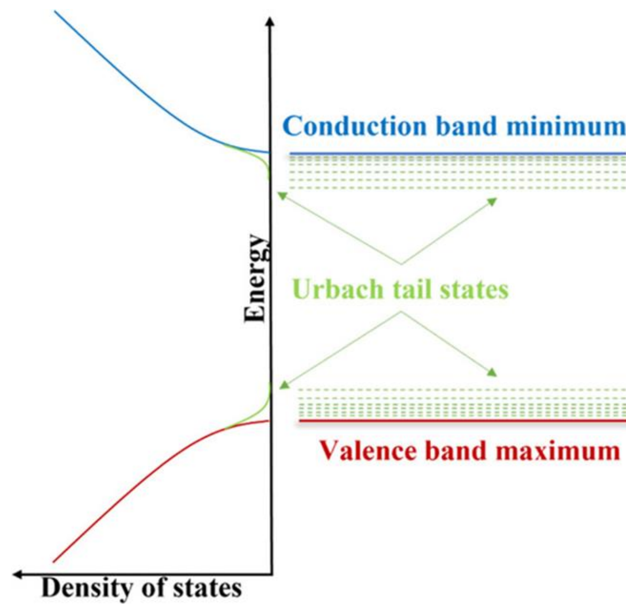

Figure II. 5: Schematic representation of Urbach tail states in a semiconductor system. Image taken from ref[151]

The Urbach empirical rule is given by the following equation:

$$\alpha = \alpha_0 \exp\left(\frac{h\nu - \mathrm{E_g}}{\mathrm{E_U}}\right) \tag{II.8}$$

Leading to:

$$\ln(\alpha) = \frac{h\nu}{\mathrm{E_U}} - \left(\frac{E_g}{E_U} - \ln(\alpha_0)\right) \tag{II.9}$$

Tail width E_u at the gap energy is obtained by plotting ln(α) as a function of $h\nu$. The inverse of the slope extracted from the linear part gives E_u to the film.

3.2 Refractive index

Light bending as it moves through a thin layer is measured by a thin film's refractive index. Variables such as thickness and composition can cause thin films to have a different refractive index than bulk materials. Controlling the refractive index affects light transmission and reflection, which makes it important in coatings and optics.

3.2.1 What advantages does the investigation of thin film refractive index offer?

Researching thin-film refractive indices is crucial for several reasons and has numerous uses in both science and technology. The following are some advantages of looking into thin-film refractive indices:

Optical Coatings: To regulate light absorption, transmission, and reflection, optical coatings frequently employ thin films with certain refractive indices. Designing coatings that improve the performance of optical equipment, such as lenses, mirrors, and filters, requires a thorough understanding of the refractive index.

Anti-reflective Coatings: When creating anti-reflective coatings, understanding the refractive index is crucial. The purpose of these coatings is to reduce reflections and enhance light transmission through optical surfaces, which is crucial for solar panels, camera lenses, and spectacles, among other products.

Interference Coatings: Thin films can be used to make interference coatings, which are optical effects with particular properties. Applications for these coatings include wavelength-selective mirrors, beam splitters, and interference filters. The optical characteristics of thin film coatings are largely determined by their refractive index.

Sensor Technologies: Thin films are employed in certain sensor technologies to alter how light interacts with the sensing components. Gaining an understanding of the refractive index enhances the sensitivity and accuracy of these sensors by optimizing their operation.

Photonic Devices: Thin films are essential parts of many photonic devices, including micro resonators, waveguides, and photonic crystals. The overall performance of the device is impacted by the way light propagates within these structures, which is determined by the refractive index of thin films.

By comprehending and adjusting thin-film refractive indices, scientists and engineers can customize a material's optical characteristics for particular uses. The development of cutting-edge technology in a variety of fields, including electronics, optics, sensors, and renewable energy, depends on this understanding.

3.2.2 The refractive index of thin film models

The refractive index of a thin film refers to the ratio of the speed of light in a vacuum to the speed of light within the thin film. It is denoted by the symbol "n" and is a fundamental optical property that describes how light propagates through the material.

Mathematically, the refractive index (n) is defined as:

$$n = \frac{c}{\mathrm{v}} \tag{II.10}$$

where: c and v are the speed of light in a vacuum, and in the material, respectively.

The refractive index of films, particularly those deposited on substrates, can be affected by several variables, such as the wavelength of light and the composition and thickness of the film. The refractive index of thin films can be described and predicted using several models:

3.2.2.1 Cauchy Equation

The Cauchy is an empirical model that comes before the Sellmeier equation. Nonetheless, it can be obtained by expanding a single Sellmeier term using a binomial series.

The Cauchy equation is a simple empirical model often used for thin films. It is represented as:

$$n(\lambda) = A + \frac{B}{\lambda^2} + \frac{C}{\lambda^4} + ... \quad \text{(II.11)}$$

where *A*, *C,* and *B* are material-dependent coefficients, and λ is the wavelength of light.

The Cauchy equation is the most popular model for transparent materials because of its ease of use and simplicity. Using the Cauchy equation is likewise straightforward: *A* determines the index's amplitude, while *B* and *C* add curvature to create normal dispersion.

Only when n(λ) follows normal dispersion is the Cauchy correct.

3.2.2.2 Sellmeier Equation

The Sellmeier equation [152], is another empirical model, commonly used for describing the wavelength-dependent refractive index in the context of dispersion. It is often expressed as a sum of terms, each involving coefficients specific to the material:

$$n^2(\lambda) = 1 + \sum_i \frac{B_i \lambda^2}{\lambda^2 - C_i} \quad \text{(II.12)}$$

Where, *C* parameters are the *square* of the resonant wavelengths (The resonant wavelengths are associated with specific features or transitions in the material, often related to electronic or vibrational resonances), and *B* some constant.

The Sellmeier model is effective in spectral regions without absorption. However, it is not applicable to our case, which involves an absorption factor, as will be discussed later.

3.2.2.3 Drude-Lorentz’s Model

The Drude-Lorentz model is more theoretical and is based on the classical oscillation of electrons in a material. It provides a more detailed description of the complex refractive index

($\check{n} = n + ik$), where *n* is the real part (related to the speed of light) and *k* is the imaginary part (related to absorption). The Drude-Lorentz model involves parameters like resonance frequency, damping factor, and strength of the oscillator.

3.2.2.4 Tauc-Lorentz's Model

This model is often used for materials with indirect bandgaps. It combines the Tauc optical gap theory with the Lorentz oscillator model to describe the absorption spectrum and, consequently, the refractive index.

3.2.2.5 Birouk's Model

This model was used in polysilicon thin film. like most models, Birouk's model is based on free carriers' absorption in the classical theory of Drude, the basic principle of the model was deduced from the complex permittivity, and assuming that n^2 is greater than k^2 (this is verified in our case: 0.45 µm < λ < 0.85 µm), and thanks to Taylor expansion, a model with distinct characteristics was created as follows [153]:

$$n^2 = n_{(0)}^2 - AB\lambda^2 \sum_{i=0}^{\infty} \left(-B\lambda^2\right)^i \tag{II.13}$$

Where:

$$k(\lambda) = 0$$

The expressions for the parameters A and B are as follows:

$$A = \frac{\mu^2 m^* N}{\varepsilon_0} \tag{II.14}$$

$$B = \frac{q^2}{4\pi^2 c^2 \mu^2 m^{*2}} \tag{II.15}$$

Where n, N, m^*, c, μ, and ε_0, represent respectively the refractive index, the concentration, the effective mass, the speed of light in vacuum, the mobility of the free carriers, and the permittivity of vacuum.

The simple form is like that:

$$n^2 = a - b\lambda^2 + c\lambda^4 - d\lambda^6 + g\lambda^8 - h\lambda^{10} + \ldots.. \tag{II.16}$$

The distinguishing characteristics of this model from the rest of the previous models are as follows:

- Suitable in the visible and near-infrared wavelength range.
- It has alternating signal parameters.
- The fitting parameters fall on Gaussian curves.

In the next chapter, we will study the refraction index of ZnO samples based on this model.

4 Hall measurement

When a magnetic field is supplied perpendicular to the current, a conductor (typically a metal or semiconductor) begins to generate an electric field that is perpendicular to the current flow. The type (positive or negative), concentration, and mobility of charge carriers (usually electrons or holes) in a material can all be studied and determined with the use of the Hall effect.

When a magnetic field is applied perpendicular to the direction of the current, the Lorentz force acts on the moving charge carriers, causing them to be deflected to one side of the conductor (Refer to Figure II.6). This accumulation of charge on one side creates an electric field that opposes the further flow of charge carriers. The resulting voltage across the conductor perpendicular to both the current and magnetic field is known as the Hall voltage.

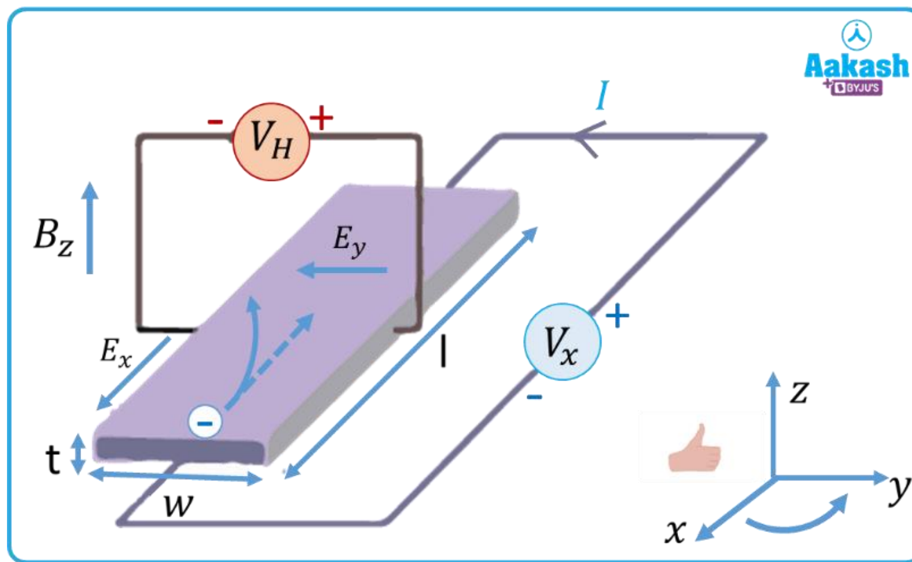

Figure II. 6: Schematic diagram of a Hall effect [154].

Utilizing Hall bars for measurements necessitates a complex patterning of the examined layer, which is not always feasible and involves additional processing steps.

The Hall coefficient R_H can be written as:

$$R_H = \frac{E_y}{I_x B_z} \tag{II.17}$$

Where, J_x current density, E_y Electric field established due to Hall Effect, B_z Applied magnetic field.

The Hall coefficient assumes a positive value when the quantity of positive charges surpasses the quantity of negative charges.

The Hall voltage gives the charge carrier density and the type of charge carrier (holes or electrons) depending on its sign, its relationship is written as follows:

$$V_H = \frac{I_x B_z}{n\,qt} \tag{II.18}$$

Although there is this previous method, there is an alternative approach, the Van der Pauw method, is more convenient as it can be applied to square samples, which are simpler to fabricate

Van der Pauw geometry

The Van der Pauw method is a technique used to measure the electrical resistivity and Hall coefficient of thin semiconductor samples, particularly those with arbitrary shapes or irregularities

Five requirements must be met in order for this strategy to be applied effectively [19]:

- The sample ought to have a consistent thickness and a flat shape.
- There must be no isolated holes in the sample.
- For the sample, homogeneity and isotropy are requirements.
- It is necessary to arrange all four contacts along the sample's edges.
- Every single contact area needs to be at least ten times smaller than the sample's overall area.

In this thesis, Hall measurements were conducted using an HMS-3000 apparatus from Microworld, employing the Van der Pauw geometry. The probes in this equipment are gold-plated to ensure reliable electrical contact. In cases where the contact with the probes is not sufficiently robust, metallic pads can be deposited at the corners of the square sample. It's noteworthy that, in the context of AZO samples, the contacts between the probes and the sample were found to be ohmic, obviating the need for the deposition of additional metallic pads.

In this setup, the sample is a square, and the contacts were placed in the recommended position at each corner of the sample (See Fig. II.7), labeled from 1 to 4 in a counterclockwise order. The current flowing between contacts n and m is denoted as I_{nm}, and the voltage is represented by $V_{nm} = V_m - V_n$.

To determine the charge carrier density and mobility, a magnetic field is introduced perpendicular to the sample. In this instance, a permanent magnet with a strength of 0.55 T was employed. The current is subsequently applied between opposing corners of the sample (e.g., 2 and 4), resulting in a transverse voltage emergence due to the magnetic field (observed between 1 and 3). The relationship between the transverse voltage (Hall voltage) and the carrier density is as follows:

$$V_{13} = V_H = \frac{IB}{n\,qt} \tag{II.19}$$

It's important to note that this relationship holds true in theory when the sample exhibits perfect symmetry, leading to $V_{13} = 0$ when $B = 0$. However, in practical scenarios, the transverse voltage arising from the asymmetry of the sample can significantly exceed the Hall voltage induced by the magnetic field.

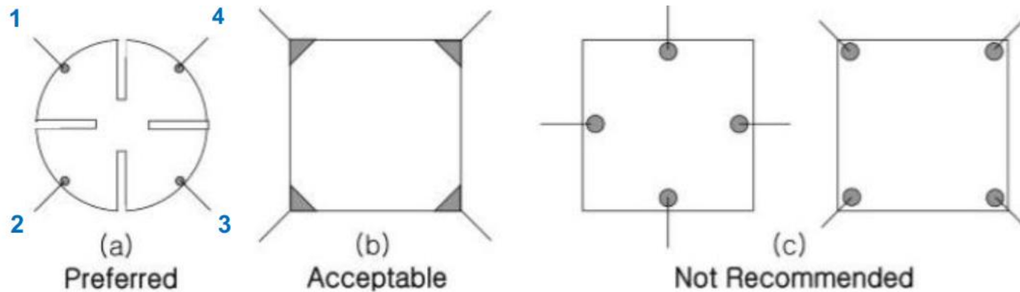

Figure II. 7: Contact positions of samples in Van der Pauw geometry.

5 Sputtering method

Sputtering is a method for depositing thin films of materials by placing a target in a vacuum chamber, introducing argon gas, and creating a plasma with a negative voltage applied to the target. Positively charged argon ions (Ar+) are accelerated toward the target, causing collisions that dislodge some of the target's atoms (See Fig. II.8). These sputtered atoms redeposit within the chamber, including on the sample placed in front of the target.

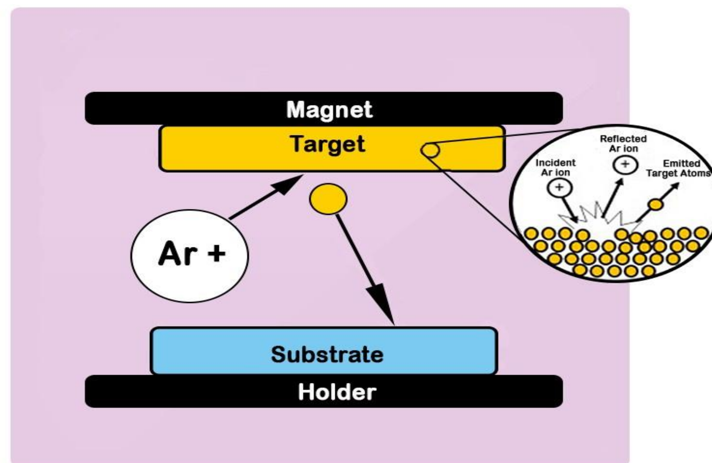

Figure II. 8: Working mechanism of sputtering technique [155].

The most straightforward and widely used magnetron configuration consists of a circular, planar target with motorized magnets positioned behind the target [156]. To maintain the target's neutral charge, an RF voltage is applied, causing alternating impacts by argon ions and electrons. The alternating radio frequency (RF) power couples with the motion of electrons within the plasma, leading to extended residence times within the plasma chamber. This prolonged interaction enhances collisional ionization processes, contributing to elevated plasma densities [157]. The

sputtering yield depends on the target material, and using argon as the sputtering gas results in a deposited material closely matching the target's composition.

Reactive sputtering, involving the addition of oxygen or nitrogen, is used to prevent target material reduction or to deposit compounds like oxides or nitrides. Even in reactive sputtering, argon is used due to its higher sputtering yield compared to oxygen or nitrogen.

A magnetic field can be employed to confine the plasma near the target's surface, using permanent magnets positioned beneath the target. These magnetic impacts the target's surface area, which changes as erosion occurs.

The magnetron employs robust magnetic fields, often generated by permanent magnets, to contain secondary electrons in the proximity of the target surface. This confinement significantly extends the residence time of these secondary electrons within the plasma. As a consequence, there is a heightened ionization of the sputter-gas atoms, leading to a denser plasma, increased plasma currents, and elevated deposition rates. The magnetic field configuration is usually designed so that the field lines are parallel to the target surface.

The target is connected via Oxygen-free High Conductivity (OFHC) copper, which helps in heat dissipation, and water circulates beneath the target to maintain a consistent temperature.

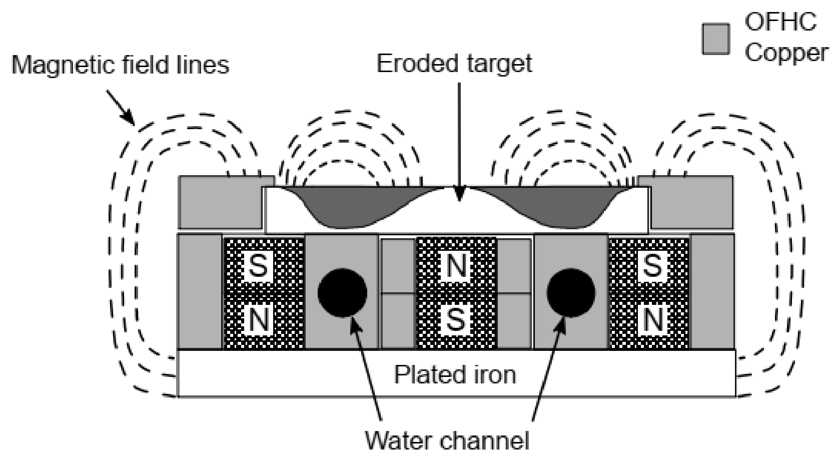

Figure II. 9: The sputtering machine employs a unique setup for its sputtering guns. This setup incorporates permanent magnets to confine the plasma close to the target material. Furthermore, a system of water channels is in place to efficiently cool the target. Additionally, Oxygen-free High Conductivity (OFHC) copper electrodes are utilized to apply voltage to the target [158].

The magnet arrangement shown in Figure II.9 is suitable for sputtering non-magnetic elements, providing strong confinement and a higher sputtering rate. However, for sputtering magnetic materials, such as nickel, adjustments to the central magnet can be made to allow the magnetic elements to escape, as the strong confinement may decrease the deposition rate.

Chapter III: ZnO Thin Films

1 Introduction

During the deposition of ZnO thin films, we intentionally adjusted the oxygen concentration in the sputtering chamber. This deliberate variation affected the stoichiometry, resulting in the production of zinc oxide samples with varying oxygen concentrations. The sputtering process operates in three distinct regimes: metallic mode, transition mode, and oxidized mode.

Changing the conditions in this experiment, especially with regard to the oxygen concentration rate, allows to expand the scope of the photoelectric study of this material. Knowing that this parameter (oxygen concentration) is of utmost importance for the photoelectric properties.

Reactive sputtering allows for altering these properties by varying stoichiometry, enabling the production of ZnOx where x values are less than 1.

It is known, as knowing that the defects play a dual role in influencing the electrical conductivity of iZnO. While defects contribute to the electrical conductivity, they simultaneously impede transparency, rendering it unsuitable for applications requiring transparent electrodes. Consequently, achieving both high conductivity and high transparency in the sample is challenging, as articulated by Tuyaerts et al [158].

In this chapter specifically and based on the above, our focus will be on examining the optical properties of pure zinc oxide. We won't delve into the electrical properties of zinc oxide in this chapter, as it does not inherently function as an electrode unless impurities, such as phosphorus (P), indium (In), boron, or aluminum (Al), are introduced. The next chapter will specifically explore the doping of zinc oxide, with a particular emphasis on the use of aluminum.

In summary, this chapter focuses on a detailed investigation of zinc oxide samples, specifically considering the variation in oxygen concentration from one sample to another. The objectives include:

- Analyzing ψ and Δ spectra to understand the impact of changing oxygen concentration on these optical spectra.
- Examining the effect of varying oxygen concentration on extinction k and absorption α.
- Calculating optical gap energy for different samples to observe the extent of its change.
- Evaluating the structural integrity of samples and identifying potential defects through the calculation of Urbach energy for various samples.
- Investigating the influence of oxygen concentration changes on optical conductivity in the visible and near-infrared range.
- Representing refractive index curves for different samples and assessing the alignment with Birouk's of refraction index model.
- Testing the accuracy of the Birouk's model in comparison to experimental results.

2 Deposition of ZnO thin films using a sputtering system

Sputtering offers the advantage of compatibility with nearly any substrate, given its capacity for deposition at room temperature. Sputtering operates in two modes: reactive, involving a Zn target in an Ar/O_2 plasma, and non-reactive, utilizing a ZnO target in an Ar plasma.

The reactive mode offers the flexibility to adjust stoichiometry, ranging from pure Zn to stoichiometric ZnO, by manipulating oxygen concentration in the plasma. This allows for the attainment of various compositions between these extremes.

Consequently, depending on the oxygen concentration, it becomes possible to alter the optical and electrical properties of the material, transitioning from a metallic state to an insulating and transparent one.

The sputtering tests for this thesis were performed in an AJA chamber equipped with a turbo-molecular pump that could pump up to 315 l/s. The ratio of the gas flow to the chamber pressure is used to determine the pumping speed. Positioned between the pump and the chamber, an automatic pressure control valve enables the modification of the effective pumping speed. Using a hot-filament ionization gauge, the base pressure in the chamber is roughly 10^{-7} mbar before to the deposition procedure.

Separate mass flow controllers are used for argon (Ar) and oxygen (O_2) to regulate the gas flow. A capacitance vacuum gauge is used to monitor and maintain the chamber's pressure at 2.7×10^{-3} mbar during the deposition process. Because it can detect pressure regardless of the kind of gas, this gauge was chosen for reactive sputtering techniques, which involve the simultaneous use of many gases in various amounts.

Samples are positioned at a rather large sputtering distance of 122 mm and rotated at 45 rpm to provide consistency in the deposition process. This considerable separation helps to reduce problems caused by bombardment by negative oxygen ions. Furthermore, oxygen is added to the chamber through tiny pores at the substrate level, which are far from the target where the plasma density is maximum, to further reduce the production of oxygen ions. Conversely, argon is introduced at the chamber's bottom. See the chamber schematic in Figure III.1

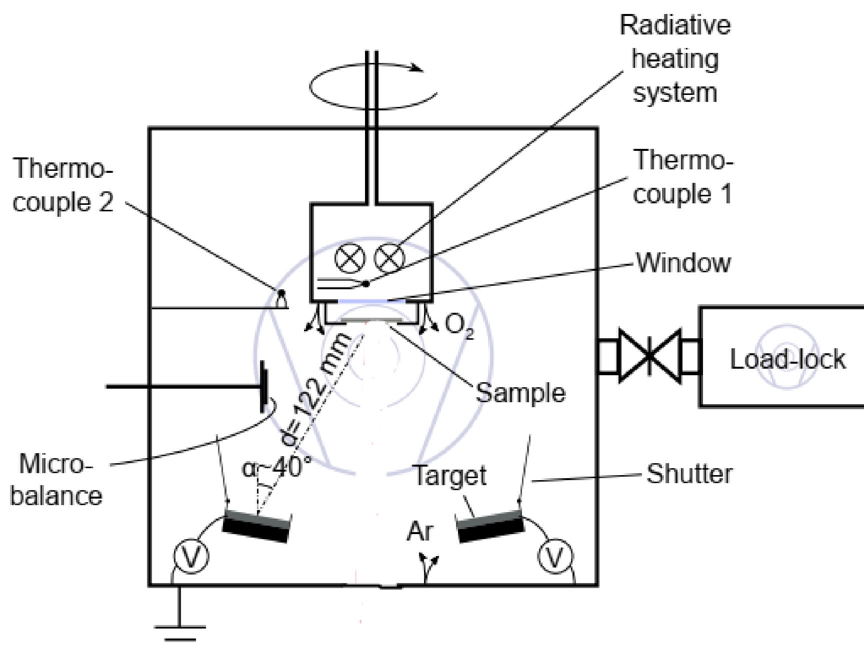

Figure III. 1: The sputtering chamber utilized for depositing ZnO, AZO thin films. A quartz microbalance was utilized to measure the deposition rate in real-time, and a thermocouple was integrated within the chamber to closely monitor temperature variations. Additionally, to achieve excellent uniformity, the samples were subjected to rotation at a speed of 45 revolutions per minute (rpm), Image taken from ref[159].

Reactive sputtering undergoes a transition mode when the oxygen partial pressure is changed, moving from a metallic mode (low oxygen concentration, target surface is metallic) to an oxidized mode (high oxygen concentration, target surface is oxidized).

In the previous section, we talked in detail about the working principle of the deposit mechanism, so in this part we will go directly into the synthesis of ZnO samples.

ZnO thin films were deposited by DC magnetron reactive sputtering with a 99.99% pure Zn target in an argon/oxygen gas combination. The substrates used were 380 µm-thick, 3-inch (7.62 cm) diameter oxidized silicon slabs. A 300 nm-thick layer of SiO_2 was produced as a result of wet oxidation at 1000°C.

The deposition process involved a continuous flow of O_2 and Ar gases at a rate of 30 standard cubic centimeters per minute (sccm), maintained under a pressure of 2 millitorrs (mTorrs).

The homogeneity of the samples is confirmed by ellipsometry tests, which show a maximum 3% variance in thickness between the center and the edge of the 7.62 centimeters substrates. After deposition, the overall thickness of the films on oxidized silicon substrates is measured using ellipsometry (SENTECH SE 850) (See table III.1), The spectra of Δ and ψ ellipsometry spectroscopic parameters were produced by it too. The samples' specular transmission (T) and

reflection (R) were assessed using a spectrophotometer, specifically the Specord 200 PLUS from Analytic Jena. Measurements were conducted across wavelengths ranging from 300 to 1,100 nm with a resolution of 1 nm. To derive the real refractive index (n) and the extinction coefficient (k), the transfer matrix method (TMM[160]) was employed to fit the experimental curves (R and T).

O_2 Concentration (%)	20	27	33	40	47	53
d (on SiO_2) (nm)	136	148	150	149	121	139

Table III. 1: Thickness d of ZnO thin films on silicon oxide substrate at different oxygen concentration.

3 Samples characteristics

3.1 Ellipsometry Spectra of the samples

Spectra recorded for thin films by spectroscopic ellipsometry typically display clear peaks and valleys, referred to as interference features, arising from constructive and destructive interference during light recombination. The quantity and placement of these interference features are contingent upon the film's thickness (t) and refractive index (n). An augmentation in either the thickness or the refractive index of the film results in an increased occurrence of interference features [138].

Spectroscopic ellipsometry measurements gave two main curves for all samples, one relating to the ratio change $\psi(\lambda)$, and the other relating to the phase difference $\Delta(\lambda)$ as a function of wavelength λ (See Figures III.2, and III.5). These curves correspond to the oxygen concentrations in the samples (20%, 27%, 33%, 40%, 47%, and 53%), with separate SE measurements conducted for each sample.

To perform a deep analysis of the spectrum $\psi(\lambda)$, we decided to take one exceptional point from each spectrum ψ, and that point was the maximum of the spectrum. In reality, we will analyze the effect of oxygen concentration on thin films based on changes in the ψ peaks

In detail, for $\psi(\lambda)$ spectrum, we made some steps to more analyze it:

- The peak of $\psi(\lambda)$ spectrum was called ψ_{max}, (ψ_{max1} for 1st sample at 20% oxygen concentration, and ψ_{max2} for 2nd sample at 27% oxygen concentration…..).
- We plotted ψ curves as a function of oxygen concentration.

Note that we took the big peaks from spectra, which are spreading out over the wavelength range (400-600nm), in visible domain.

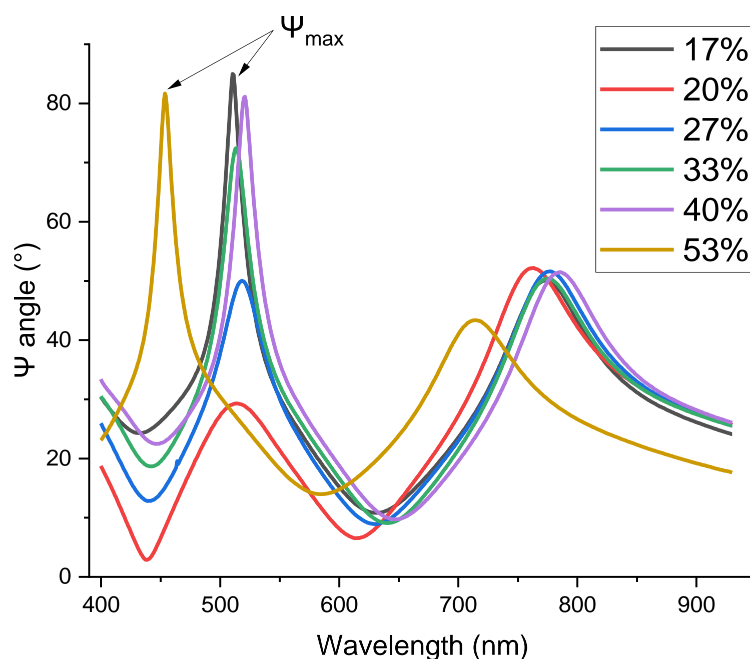

Figure III. 2: Evolutions of ellipsometry ratio ψ as a function of wavelength for different samples of ZnO thin films, the peaks in the spectra of the samples are denoted by ψ_{max}.

Before proceeding with the explanation, we would like to point out that the sample with an oxygen concentration of 47% does not appear in the ψ and Δ curves, although it is mentioned in the optical properties later. This is because this sample exhibited abnormal and distorted results in the spectroscopic measurements. Conversely, the sample with an oxygen concentration of 17% showed a good spectrum in the spectroscopy but produced abnormal and illogical results in the optical properties measurements. This explains why it appears in the spectroscopic measurements but is subsequently absent.

From Figure III.2, we can see a variation in the ψ spectra of the samples, of course, this variation is due to the different composition of the material first. The change in the oxygen concentration during deposition plays a major role in this matter.

To investigate a precise observation, we plot ψ_{max} versus oxygen concentration of thin films (see Figure. III.3). This graph indicates that the spectral peak was influenced by varying oxygen concentrations. It exhibited a higher intensity at low concentrations, decreased at intermediate concentrations, and gradually increased again with higher levels of oxygen in the samples. However, when considering thickness, ψ_{max} presents a different perspective (refer to figure. III.4), showing fluctuations in the property that are not fully explained. Typically, changes in thickness affect the peaks of the ψ spectra, but in this case, the difference in thickness between the thin films (d_{max} - d_{min} = 39 nm) was relatively small. These unexplained fluctuations could be attributed to various factors, including variations in oxygen concentration that may accompany changes in thickness.

This is consistent with the understanding that when multiple factors are at play, the causes can be diverse.

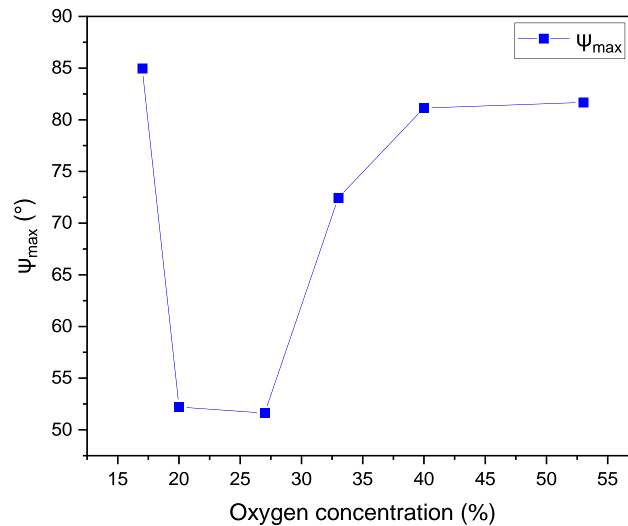

Figure III. 3: Evolution of the ellipsometry parameter ψ_{max} as a function of varying oxygen concentrations.

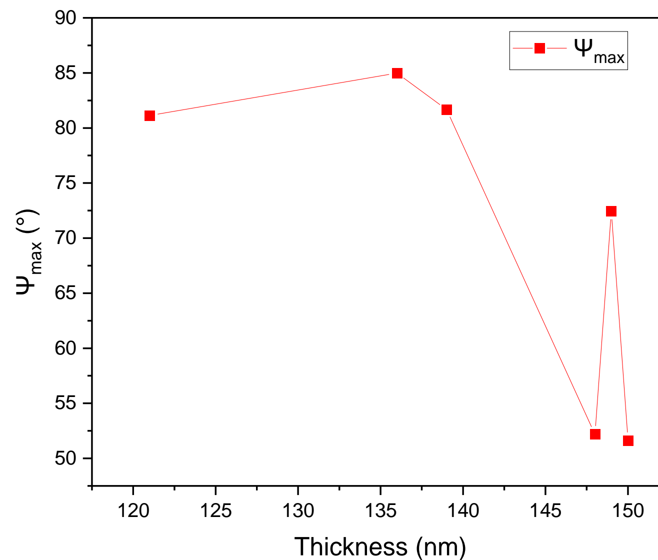

Figure III. 4: Evolution of the ellipsometry parameter ψ_{max} versus thickness of ZnO samples.

Figure III.5 illustrates the variation in ellipsometry phase difference Δ across different wavelengths for various samples of ZnO thin films. The observed differences in spectra are attributed to varying oxygen concentrations among the samples. These thin films were produced using three main

methods: metallic, transitional, and isolated modes. Different modifications to the material's structure and essential elements were brought about by these modes. These adjustments show a high degree of responsiveness in delta spectra. The material's effect on the light traveling through the thin layer is what causes this sensitivity. As a result, this effect varies in proportion to any modification made to the material's basic characteristics, such as its structure. Sub-properties, like as roughness and thickness, also affect the changes that are seen.

Typically, the Δ spectrum shows the same λ values for the successive higher and lower portions, meaning that $\lambda_{\Delta min} = \lambda_{\Delta max}$. As such, we will handle this as a singular number in order to explore some parameter features of ZnO thin films in all samples as a function of that wavelength.

Where, there are two parts of λ_{Δ}, ($\lambda_{\Delta 1}$, and $\lambda_{\Delta 2}$), see Figure III.5.

To view the displacement of Δ spectrum as a function of oxygen concentrations it suffices to plotted $\lambda_{\Delta 1}$ part of samples as a function of oxygen concentration, see Figure III.6.

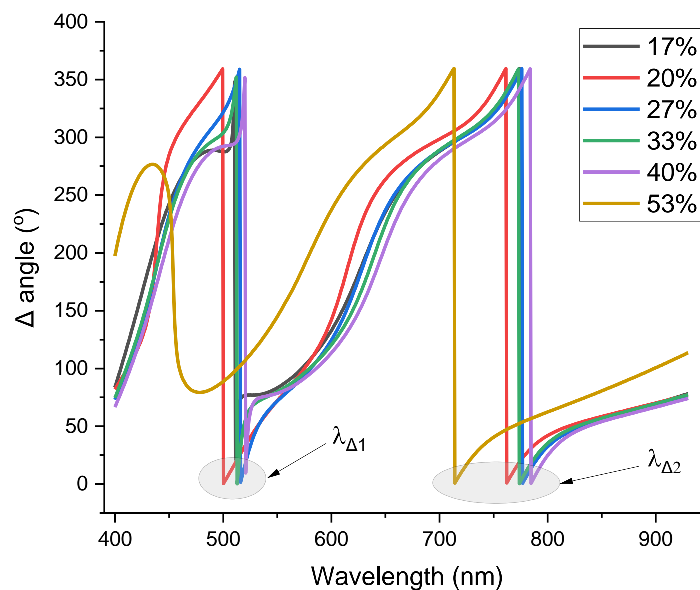

Figure III. 5: Evolutions of ellipsometry phase difference Δ as a function of wavelength for different samples of ZnO thin films, the wavelengths at peaks and downs in the spectra of the samples are denoted by $\lambda_{\Delta 1}$ for part 1, and $\lambda_{\Delta 2}$ for part 2.

When we see the evolutions of $\lambda_{\Delta 1}$, and $\lambda_{\Delta 2}$ values as a function of oxygen concentration in Figure III.6, it becomes clear to us that the spectra shift very slightly (they may appear to be very stable at first glance) towards longer wavelengths as the oxygen concentration in the sample increases, but in the last sample with a 53% oxygen concentration the spectra move towards longer wavelengths.

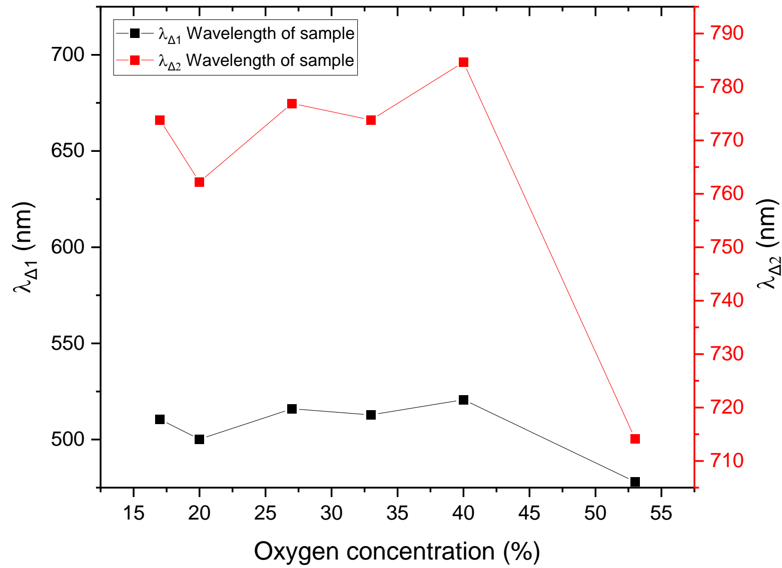

Figure III. 6: $\lambda_{\Delta 1}$, and $\lambda_{\Delta 1}$ values as a function of oxygen concentration for ZnO thin films

Generally, one of the remarkable features of spectroscopic ellipsometry is the high precision of the measurement, and very high thickness sensitivity (~0.1 Å) [139]. That is so clear when looking at Figure III.7 and III.8. The effect of thickness on $\lambda_{\Delta 1}$, and $\lambda_{\Delta 2}$ was different, where $\lambda_{\Delta 1}$ decreased and then increased, but $\lambda_{\Delta 2}$ was still stable then decreased as a function of thickness. As we explained previously, those phenomena may depend on several parameters among them: variation in oxygen concentration, and differences of thickness together.

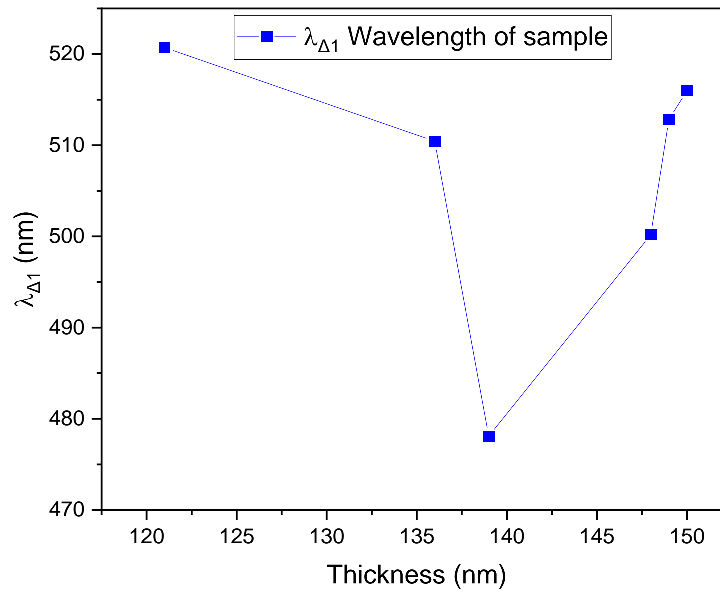

Figure III. 7: $\lambda_{\Delta1}$ comportment values versus ZnO thin film thicknesses.

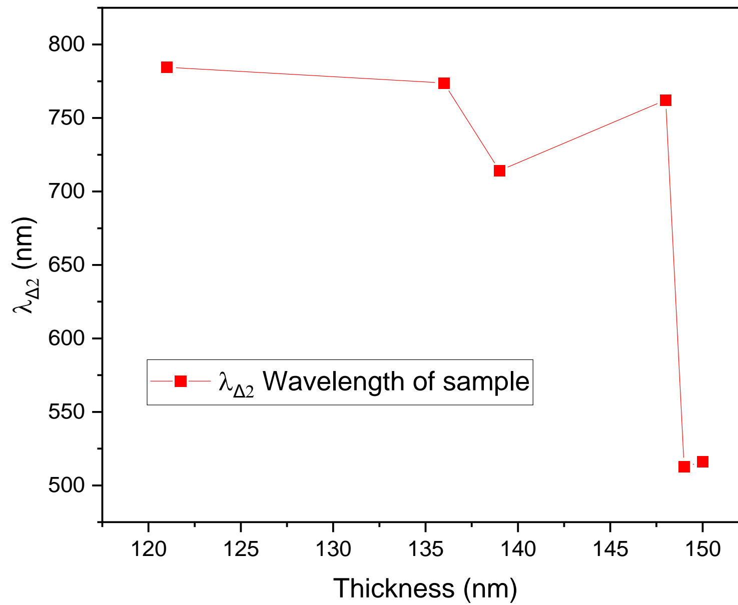

Figure III. 8: $\lambda_{\Delta2}$ comportment values as a function of the thickness of ZnO thin films.

3.2 Absorption coefficient of thin films

The investigation of optical properties in semiconductor thin films plays a crucial role in comprehending the film's optoelectronic nature. These properties find interpretation through the interaction between incident photons and the semiconducting films. Moreover, the optical properties of thin films can alter or influence the characteristic spectrum of incident light passing through them. While the light spectrum provides an overview of physical processes specific to the study of samples, optical properties have the potential to modify the propagation vector or the intensity of incident waves. Optical absorption studies offer a straightforward method for determining the band gap energy and elucidating certain optical characteristics of semiconductors and non-metallic materials.

Usually, the extinction coefficient k is represented and analyzed with refractive index, but this time, we will represent it separately with absorption coefficient, optical conductivity, bandgap energy, and Urbech energy. The refractive index will be analyzed later because it takes a long separate study somewhat.

Figure III.9 represents the comportment of the extinction coefficient k as a function of incident radiation wavelength. Generally, we can see that the extinction coefficient does not exceed 0.5 at low wavelength, and k begins to decrease at 400nm, then stables low as long of visible and NIR range. The extinction coefficient of ZnO thin films varies with oxidation levels. As oxidation increases, the extinction coefficient tends to decrease. This change may be attributed to the reduction in Zn clusters, resulting in increased transparency. That explanation even includes the absorption coefficient α as seen in Figure III.10. Because there is a proportional relationship between absorption coefficient α, and the extinction coefficient k, as we mentioned in Eq II.5.

The absorption characteristics of the electromagnetic wave spectrum in thin films rely on various parameters, such as the type of material, doping materials, their ratios, film thickness, photoconductivity, and the extinction coefficient of the films. In spectral regions characterized by substantial absorption, a semiconductor sample absorbs all incoming energy, leaving only the portion that is reflected at the surface. As a result, specific features and important parameters are linked to the absorption of photons within the structure of thin films. This includes key factors such as Bandgap and Urbach energy, which will be discussed in the next section.

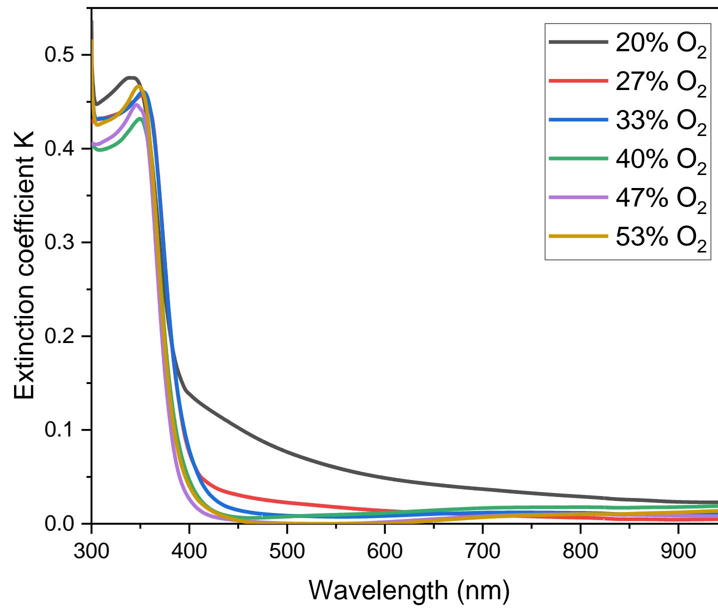

Figure III. 9: Extinction coefficient variations as functions of incident radiation wavelength for different ZnO thin films.

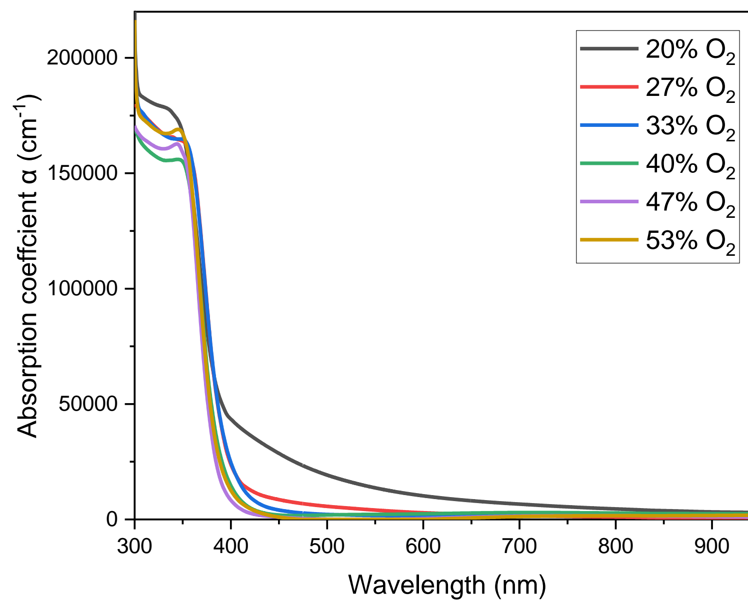

Figure III. 10: Absorption coefficient variations as functions of incident radiation wavelength for different ZnO thin films.

3.3 Bandgap and Urbach energy

Figure III.11 illustrates the variation of $(\alpha h\upsilon)^2$ as a function of the photon energy ($h\upsilon$) for different ZnO thin films. The bandgap energy Eg is obtained through the Tauc-plot method, as mentioned earlier in the previous chapter in Section 2.2. The bandgap energy varied between 3.18 and 3.32 eV. To investigate the effect of oxygen concentration on Eg, we created the curve in Figure III.12. It can be seen that Eg parameter decreases then increases with increasing oxygen concentration. At first glance, this behavior profile looks like Figure III.3 of ψ_{max} as a function of wavelength.

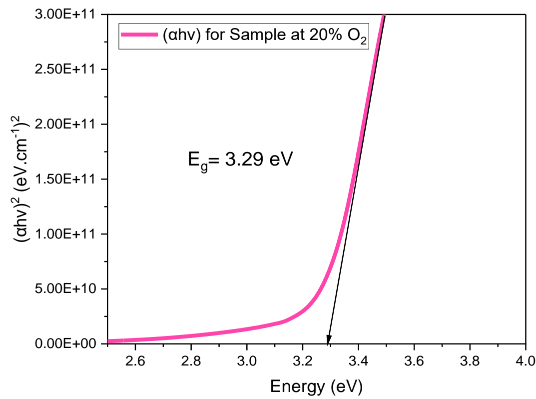

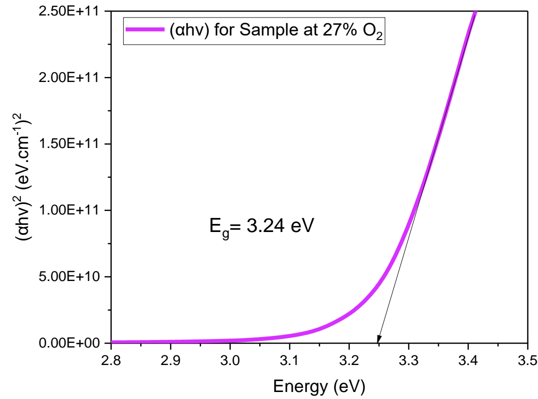

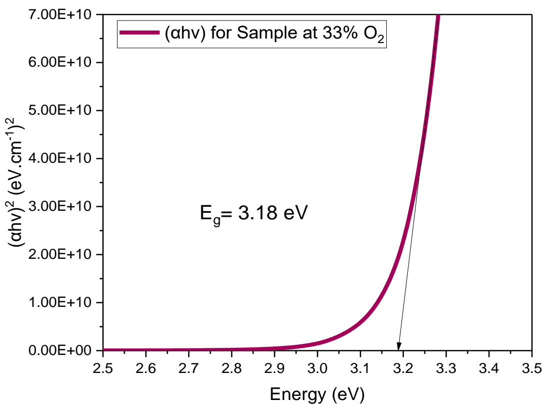

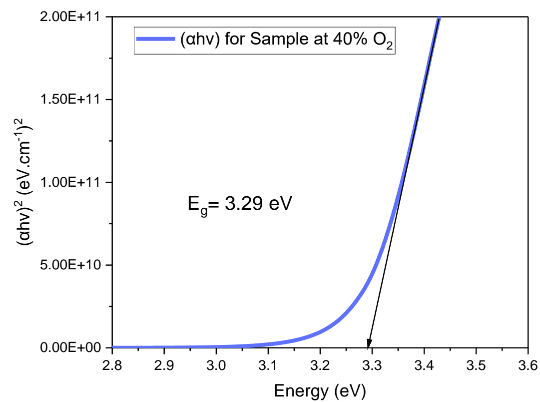

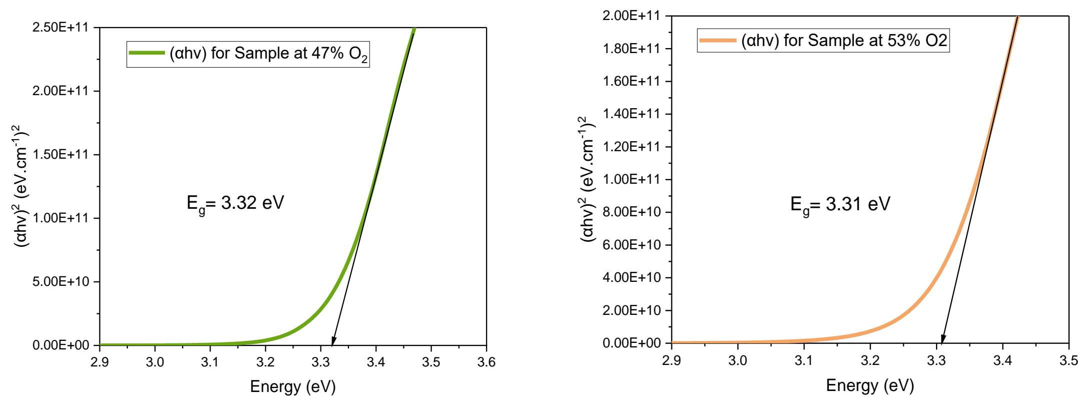

Figure III. 11: Variation of $(\alpha h\upsilon)^2$ with the photon energy ($h\upsilon$) for different ZnO thin films (Thin arrow represents the linear behavior according to Tauc's relationship)

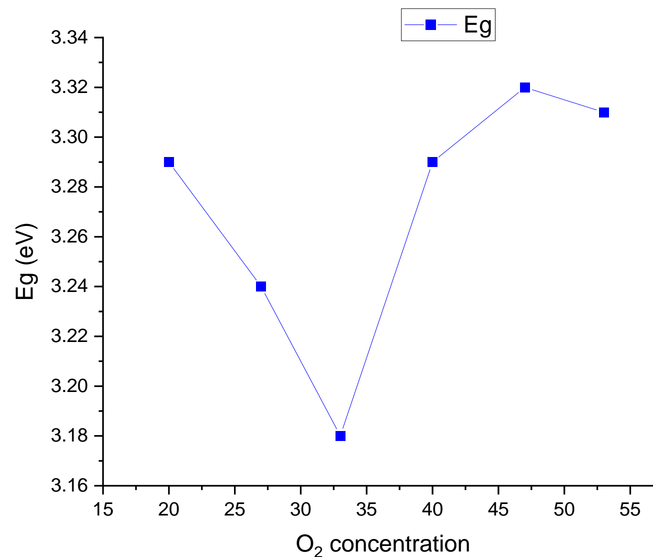

Figure III. 12: Bandgap energy variation as a function of different oxygen concentrations of ZnO thin films.

The optical absorption spectra of semiconducting materials play a crucial role as they provide fundamental information about the composition and optical band gap. These spectra can be categorized into three primary regions:

- Weak Absorption Region: Originating from defects and impurities, this region reflects a weak absorption component in the optical absorption spectra.
- Absorption Edge Region: Resulting from structural perturbations and system disorder, this region is characterized by an absorption edge in the optical absorption spectra.

- Strong Absorption Region: Determining the optical energy gap, this region signifies strong absorption features in the spectra.

Near the optical band edge, the absorption coefficient curve exhibits an exponential portion known as the Urbach tail. This tail is evident in low crystalline, poor crystalline, disordered, and amorphous materials due to the presence of localized states extending into the band gap [161].

Figure III.13 represent the Urbach energy variation as a function of different oxygen concentrations of ZnO thin films. Initially, as oxygen concentration increases, the formation of defects in the zinc oxide lattice may occur, leading to a reduction in Urbach energy. The subsequent stabilization of Urbach energy suggests a point where the addition of more oxygen does not significantly alter the structural properties of the zinc oxide thin films.

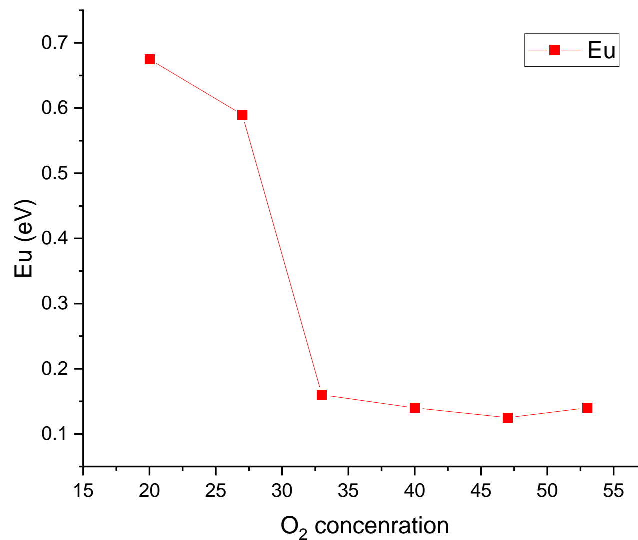

Figure III. 13: Urbach energy variation as a function of different oxygen concentrations of ZnO thin films.

3.4 Optical conductivity

The absorption characteristics of the electromagnetic wave spectrum in thin films rely on various parameters, such as the type of material, doping materials, their ratios, film thickness, photoconductivity, and the extinction coefficient of the films. In spectral regions with significant absorption, all the energy entering a semiconductor sample is absorbed, and the only remaining portion of incident energy is that which is reflected at the surface. Consequently, certain features and crucial parameters are associated with the absorption of photons within the texture of thin films, including optical conductivity.

Optical conductivity in semiconductors refers to the material's ability to conduct electric current in response to the absorption of light. It is a measure of how well the semiconductor can carry an electric current under the influence of optical excitation, typically in the presence of photons.

The optical conductivity (σ) in semiconductors is closely tied to the optical band gap. In the case of thin films, various factors influence optical conductivity, including the absorption coefficient, refractive index, incident photon frequency, and extinction coefficient. The calculation of optical conductivity can be performed using the following relationship [162, 163]:

$$\sigma = \frac{\alpha \, n \, c}{4\pi k} \qquad \text{(III.1)}$$

where (c) is the speed of light in air or free space

Figure III.14 demonstrates how the optical conductivity varies with the wavelength of incident photons in the thin films studied in this investigation. It can be observed that the optical conductivity experiences an increase at higher photon energies. This is attributed to the pronounced absorbent characteristics of thin films in that specific region, and it may also be attributed to the excitation of electrons by the energy carried by photons. Globally, the optical conductivity also decreases with the addition of more O_2 to the thin films, (See Fig. III.15).

The effect of oxidation on optical conductivity is not notably substantial or sufficiently evident, while the impact of wavelength is much more distinct. This claim is substantiated by the data depicted in Fig. III.16.

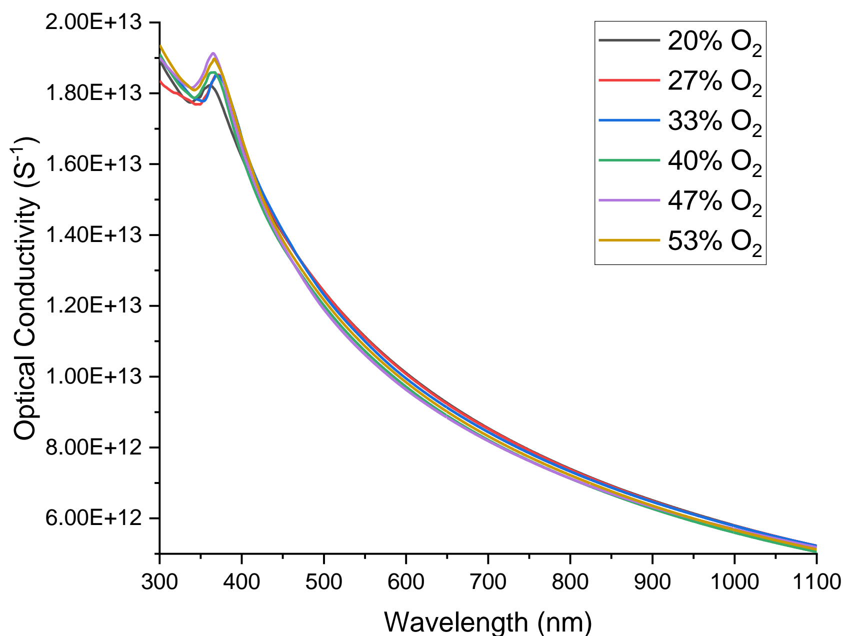

Figure III. 14: Dependence of optical conductivity upon the wavelength of the incident photon for ZnO thin films.

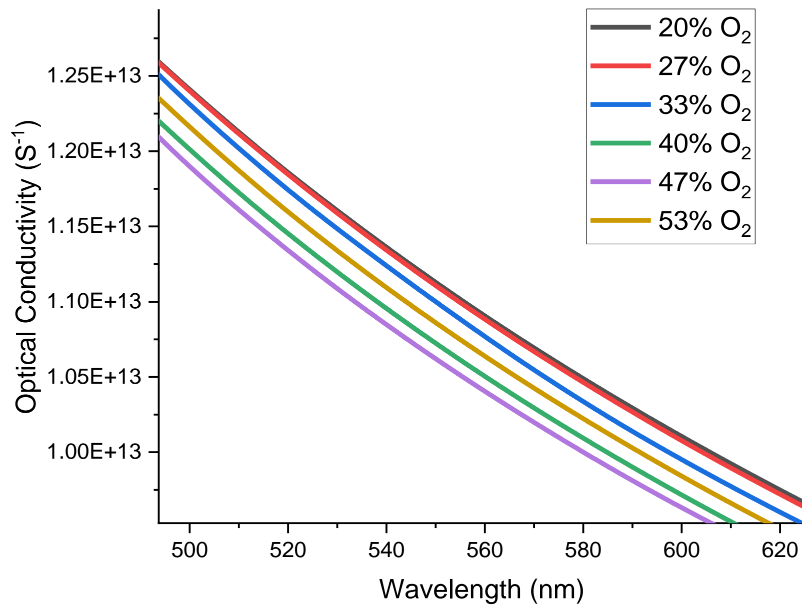

Figure III. 15: Optical conductivity versus wavelength of the incident photon at a small range wavelength.

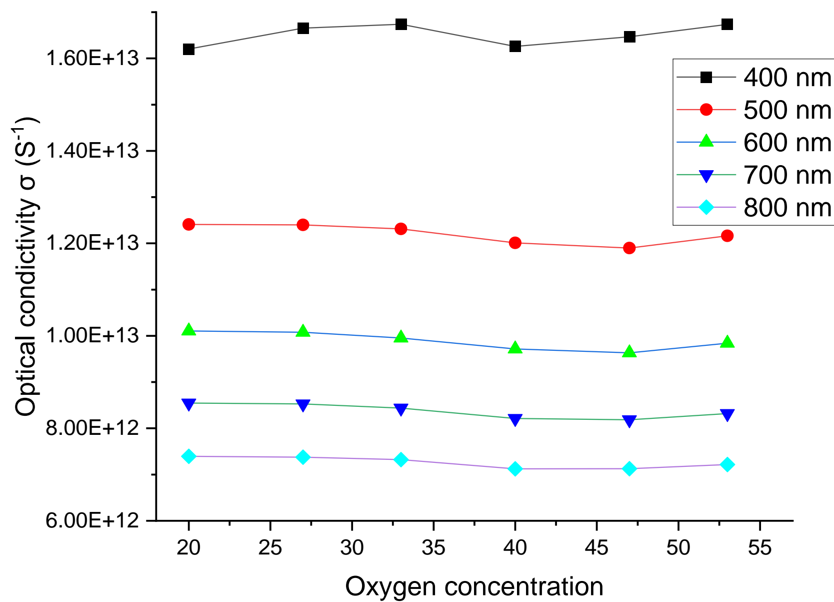

Figure III. 16: Optical conductivity as a function of oxygen concentration at several specific wavelength.

4 Analyzing the refractive index through modeling

Figure III.17 shows the variation of the refractive index of ZnO thin films with wavelength. As depicted in the figure, the refractive index decreases as the wavelength increases. This phenomenon occurs because photons with higher energy (shorter wavelengths) travel faster through the material. The different refractive indexes of samples exhibit a decrease whenever the oxygen concentration increases. This is due to the tendency of the material towards the oxidized state. As oxidation increases, the refractive index of the sample decreases. What further demonstrates this phenomenon is the study of the evolution of extinction k in the same wavelength range (See Fig. III.18).

Figure III.18 illustrates a consistently low extinction coefficient, which leads to values close to zero across multiple samples. Typically, the coefficient value tends to rise with reduced oxidation, as evident in the sample of 20% oxygen concentration, which still exhibits a somewhat metallic character.

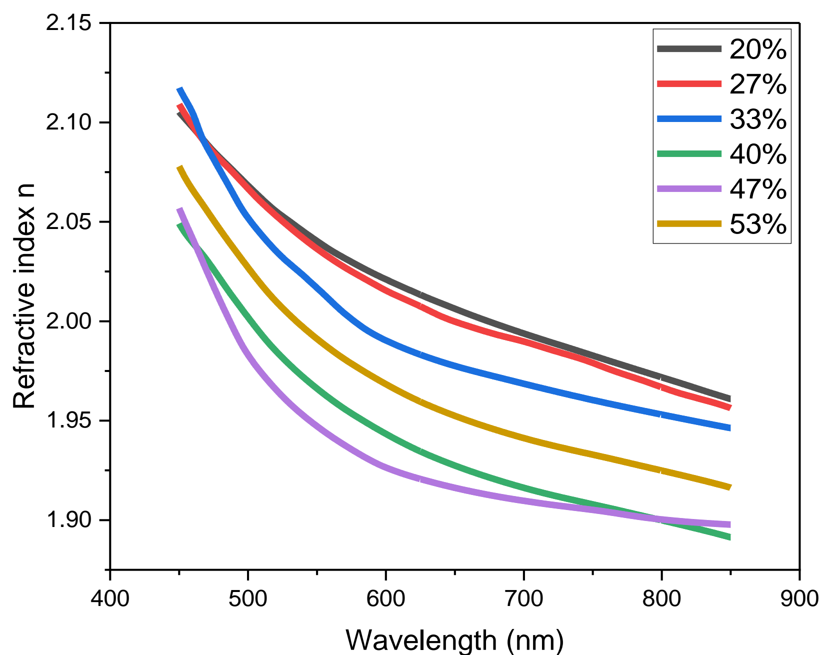

Figure III. 17: Refractive index development of ZnO thin films versus wavelength at visible and near-infrared range.

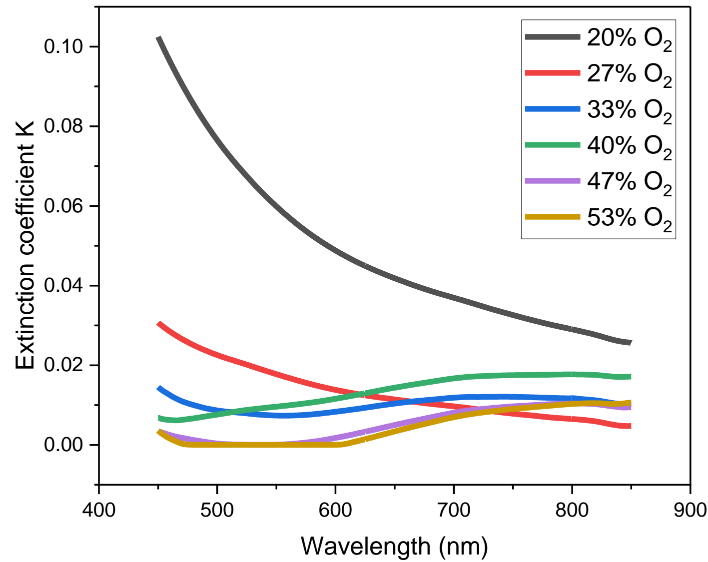

Figure III. 18: Development extinction coefficient k for ZnO thin films versus wavelength at visible and near-infrared range.

In the previous section, we mentioned that there are many models to represent the refractive index, one of those models was a Birouk's model (See Eq.II.13). In this section, we will analyze our refractive index result based on this model, and also examine the extent to which this model fits with our results.

The standard relation III.2 represents the square of the refractive index based on that model. where, a, b, c, d, e, f are different parameters (coefficients), that depend on different characteristics of the thin film. In brief, to analyze the results of refractive index based on this model we will perform the following steps for all samples:

- We will plot $n^2 = f(\lambda^2)$; (the square refractive index n^2 of the sample as a function of λ^2).
- We will do the polynomial fitting for $n^2 = f(\lambda^2)$ curve to extract the values of different parameters: a, b, c…
- To see the shape of the parameter's values (coefficients a, b, c…) more clearly, we will represent them on a graphic curve as a function of each coefficient letter a, b, c….

$$n^2 = a - b\,\lambda^2 + c\,\lambda^4 - d\,\lambda^6 + e\,\lambda^8 - f\,\lambda^{10} + \ldots.. \quad \text{(III.2)}$$

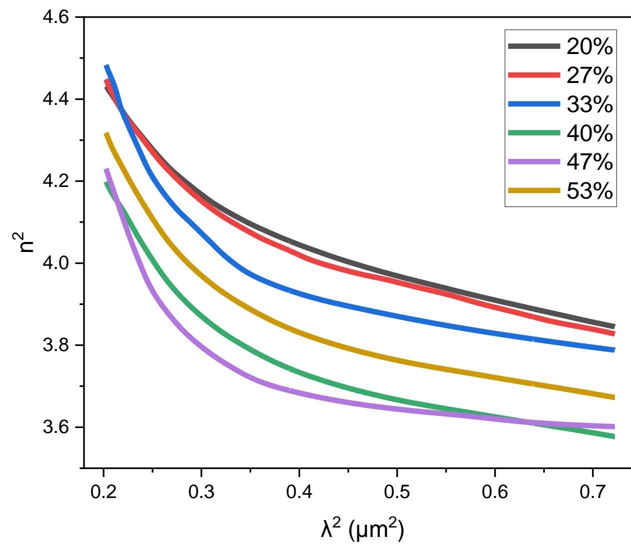

Figure III. 19: Variation of refractive index square of ZnO thin films versus wavelength square.

The function $n^2 = f(\lambda^2)$ in Eq. II.13 has theoretically an unlimited number of terms. Still, in practice, just a few numbers of these terms are sufficient to model well the refractive index variation (when i is high enough (more than 4 in practice)) [153]. In our case, to obtain more accurate results we will take $i = 9$.

Figure III.19 represents the comportment of the square of refractive index n^2 as a function of wavelength square λ^2. The fitting of those curves by a polynomial at 9 degrees gives numeral relationships that have been represented in the table III.2.

Oxygen concentrations of samples	20%	27%	33%	40%	47%	53%
	n^2	n^2	n^2	n^2	n^2	n^2
$n^2(\lambda^2) = a - b\lambda^2 + c\lambda^4 - d\lambda^6 + e\lambda^8 - f\lambda^{10} + g\lambda^{12} - h\lambda^{14} + i\lambda^{16} - j\lambda^{18}$						
Intercept = a	-0.2655	9.14851	35.57692	-35.7471	-13.26432	-13.33135
b	123.31852	-69.00136	-586.57576	918.19195	513.11345	428.82388
c	-1232.05637	472.54734	4865.70631	-8960.33358	-5826.25166	-4290.2509
d	6543.18787	-2078.01886	-23169.05037	49197.31943	35549.26171	23736.03694
e	-21186.70263	6341.94184	68917.86035	-168901.95962	-132329.46255	-81459.42654
f	43998.53008	-13920.77164	-131779.97074	377507.29819	315779.69935	181191.40349
g	-59005.47948	21845.15225	160864.99045	-550656.77369	-486537.0361	-262298.53303
h	49462.12939	-23163.12746	-119803.33432	506404.53852	468830.3952	238958.54531
i	-23570.27794	14654.57944	48648.78779	-266827.15071	-257205.04511	-124576.28293
j	4871.52774	-4116.53363	-7957.19677	61453.54071	61360.55052	28365.21416

Table III. 2: Data of polynomial fitting of refractive index models for different ZnO thin films at 9 degrees (10 terms).

Like the theoretical form of the square refractive index (Equation III.2), the parameters take an alternating sign. (See Table III.2).

From Figure III.20, we can see that when reporting the parameters values according to their position in the equation, all of the parameters give a turbulent wave between negative and positive with its peak in the middle, begins with a value very close to zero and ends with a low value. To make it clearer we plot the absolute values of the parameters (See Fig. III.21).

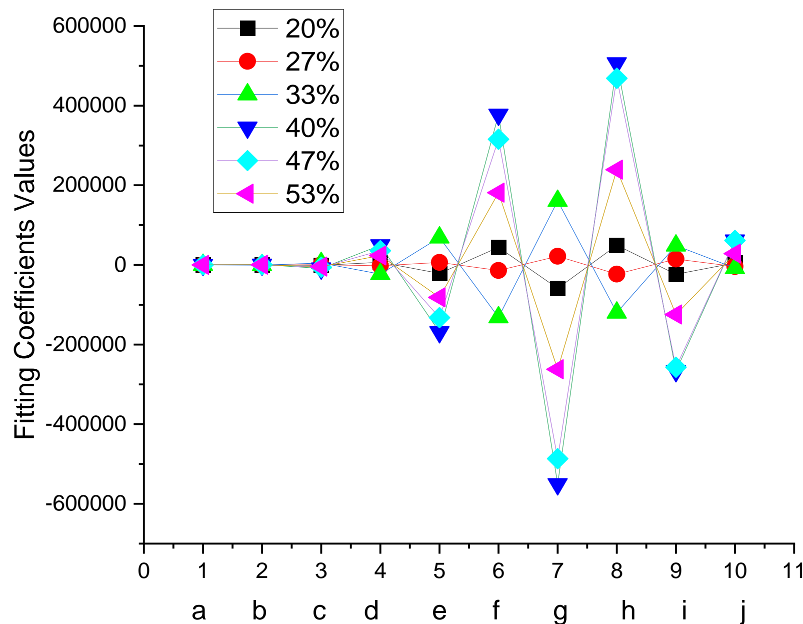

Figure III. 20: values of the parameters extracted from the fit equation as a function of their position in the equation, for ZnO deposits (one curve per sample characterized by its different oxygen concentration).

When looking at Figure (III.21), the peaks become clearer. Which is also confirmed by the figure that the beginning of the factors is very close to zero and that their end is not somewhat close to zero. This is explained by the fact that the last parameter of the model approaches zero when

$i \approx \infty$, and at this value the model has the most accurate case. This hypothesis is fulfilled in many models, such as the Drude's model, and the Sellmeier's model. From the same figure (figure III.21), it is evident that variations in oxygen sample concentrations contribute to contrasting the model parameters. The parameter values show an increase with rising oxygen concentrations up to 40%, after which they decrease again with decreasing oxygen concentrations in the thin film.

The figure III.21 adds also, a particular and additional information upon figure III.20: all the parameters absolute values of each sample, fall on a Gaussian curve.

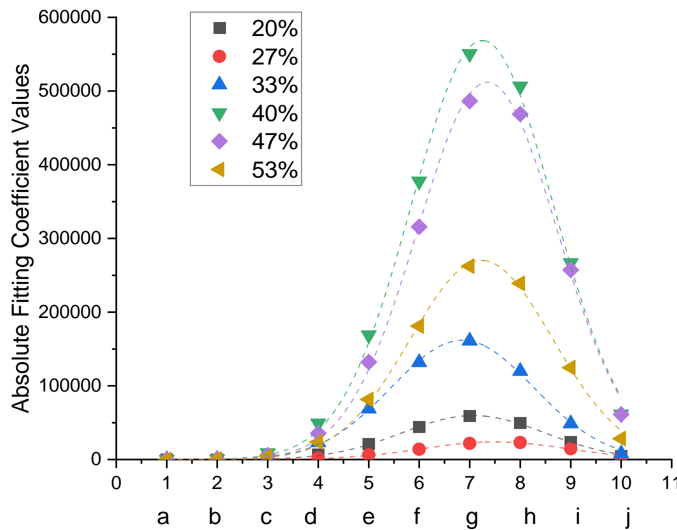

Figure III. 21: Absolute values of the parameters extracted from the fit equation as a function of their position in the equation, for ZnO deposits (one curve per sample characterized by its oxygen concentration), the dashed lines are Gaussian fittings.

Figure III.22 displays the comportment of each parameter individually as a function of the oxygen concentration of each sample, we can see that the parameter “a” increases as oxygen concentration increases, then it stabilizes after 40% from oxygen concentration, as is the case with the rest of the parameters in different samples models approximately. The shaded vertical area at the curve represents the different fitting parameters for the 20% oxygen concentration in the sample, and in the same context, the different parameters for other samples can be seen.

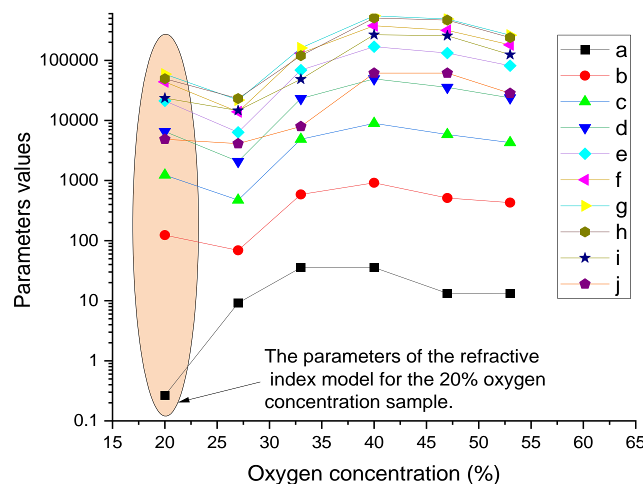

Figure III. 22: Different fitting parameters as a function of ZnO oxygen concentration (One curve per one parameter).

Figure III.23 depicts the refractive indices plotted versus wavelength for various ZnO samples within the visible to near-infrared (Vis - NIR) wavelength range, and incorporating both experimental data and Birouk's model. we can see that the consistency between the refractive index curve generated by the model and the experimental refraction index curve is apparent across all samples and throughout the investigated wavelength range. We can notice, because of the close match, that the model curve does not generally appear as it lies beneath the experimental curve. However, an anomaly emerges towards the end of the wavelength spectrum in sample curve of 47% oxygen concentration, revealing a discernible deviation between the two curves. The exact cause of this disparity remains unclear. It's possible that factors relating to the experimental conditions could contribute to this difference, although no abnormalities were found in this particular sample compared to the others during previous analyses.

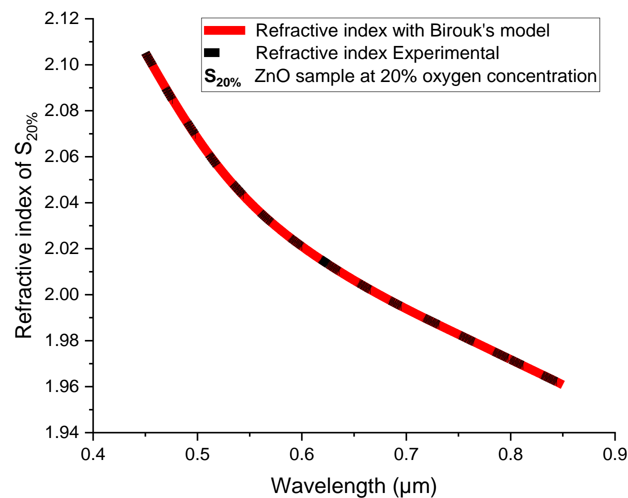

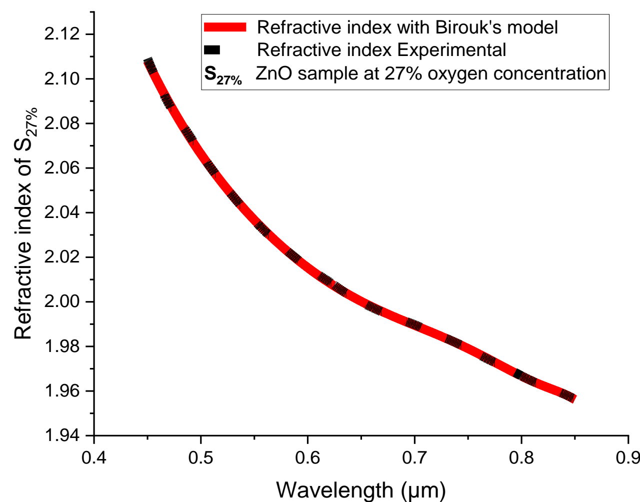

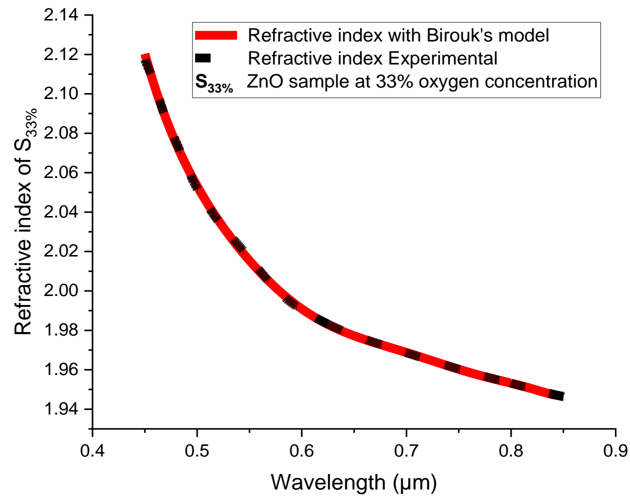
Refractive index with Birouk's model
Refractive index Experimental
S33% ZnO sample at 33% oxygen concentration
Refractive index of S33%
Wavelength (µm)
2.14
2.12
2.10
2.08
2.06
2.04
2.02
2.00
1.98
1.96
1.94
0.4
0.5
0.6
0.7
0.8
0.9

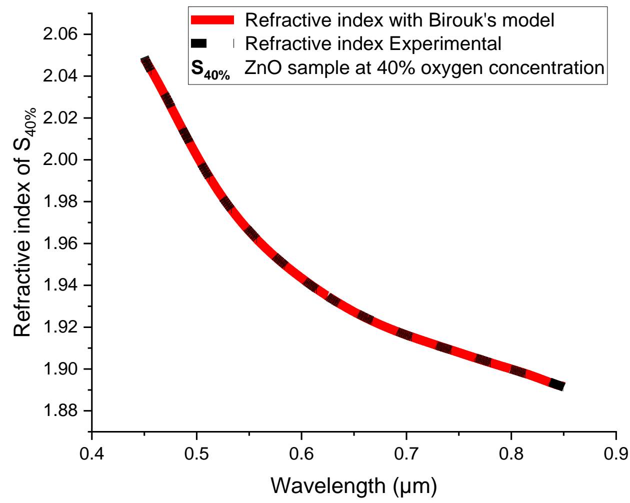
Refractive index with Birouk's model
Refractive index Experimental
S40% ZnO sample at 40% oxygen concentration
Refractive index of S40%
Wavelength (µm)
2.06
2.04
2.02
2.00
1.98
1.96
1.94
1.92
1.90
1.88
0.4
0.5
0.6
0.7
0.8
0.9

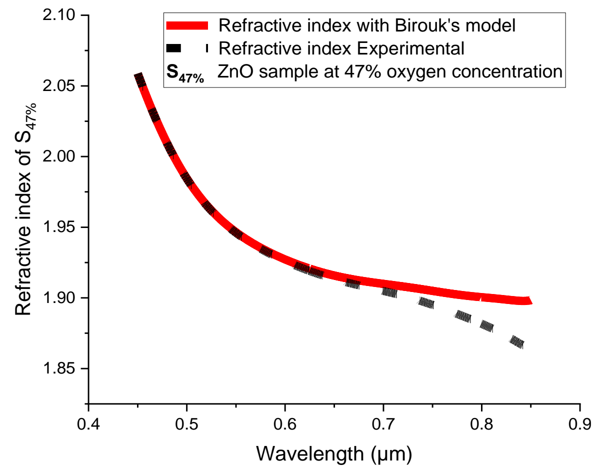

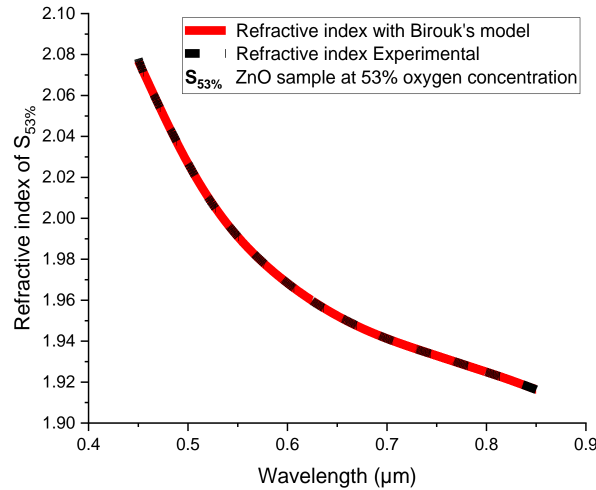

Figure III. 17: Refractive indices versus wavelength for different ZnO samples within the visible to near-infrared (Vis-NIR) wavelength range. Both experimental data and Birouk's model are included in the comparison.

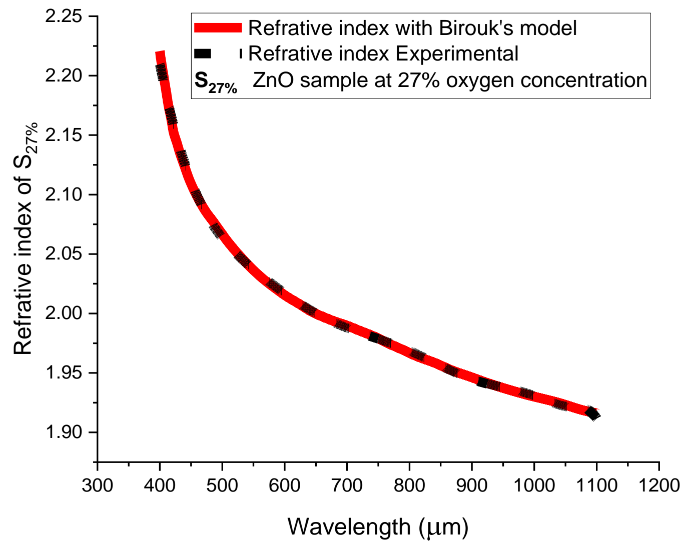

Figure III. 24: Refractive indices versus wavelength for ZnO sample at 27 % oxygen concentration within wider wavelength range. Both experimental data and Birouk's model are included in the comparison.

Figure III.24 illustrates the relationship between refractive indices and wavelength for a ZnO sample with a 27% oxygen concentration across an extended wavelength range. The comparison includes both experimental data and Birouk's model. The graph clearly illustrates a correlation between the two refractive index curves, yet a minor inconsistency persists. This could be attributed to the range and width of the wavelength, and possibly its proximity to the red spectrum wavelengths. As observed in Figure III.23, neither the concentration of oxygen nor the type of sample contributes to this discrepancy.

5 Conclusion

Modifying the oxygen concentration exerts a notable influence on the optical characteristics of zinc oxide samples, a fact evident in the examination of ψ and Δ spectra.

The evidence indicates that heightened oxidation leads to a reduction in the extinction coefficient k values, particularly evident in absorption curves. This phenomenon is a direct result of the diminishing zinc cluster as oxidation intensifies, consequently enhancing transparency. Supporting this hypothesis, the Urbach energy, a marker for the presence of defects, demonstrated a consistent decrease in energy curves with the rise in oxygen concentration.

The continuous oxidation of the samples contributed to the fluctuation of the gap energy and its change from one sample to another, as this energy ranged from 3.18 to 3.32 eV.

While it is commonly understood that the optical conductivity (σ) value rises with the energy of absorbed photons, our findings indicate that it is also significantly influenced by the intensity of

oxidation. Specifically, we observed a decrease in optical conductivity as the oxidation level increased.

The refractive index curves exhibited typical patterns within the optical range and below red spectrum wavelengths. Additionally, it was demonstrated that the values of the refractive index decrease with an increase in oxidation levels.

Birouk's index of refraction model aligned with our findings for zinc oxide samples in the following ways:

- Proved consistency in the frequencies of coefficient signals for a polynomial of degree 9 in all samples.
- Consistency was observed in the appearance of Gaussian shapes when representing the coefficients' values in relation to their positions. This consistency held true for all samples.
- The refractive index curves of the Birouk's model show a high degree of alignment and resemblance with the experimental refractive index curves in the visible and near-infrared wavelength range.

In summary, the optical factors examined in this study (refractive index n, absorption α, extinction k, optical conductivity σ, gap energy Eg, and Urbach energy E_U) are interconnected and complementary. They collectively indicate a consistent trend: as oxidation increases, absorption and excitation decrease, while optical conductivity and refractive index increase. This coherent behavior is attributed to the decrease in zinc cluster content, a phenomenon well-documented in the literature.

Chapter IV: AZO Thin Films

1 Introduction

In the preceding chapter, we carefully controlled the oxygen concentration during the sputtering process of zinc oxide films, allowing us to obtain films in varying states, ranging from oxide to metal. As observed previously and well-established in the literature[164], increasing oxidation enhances transparency while significantly decreasing conductivity. Conversely, reducing oxidation moves the material toward a metallic state, where conductivity increases at the expense of transparency. To address this dilemma and achieve practical photoelectric properties, we opted for a well-known approach: doping zinc oxide with an electron-donating material, specifically aluminum.

Before delving into the details of this chapter, it's important to highlight the rationale behind selecting aluminum as the doping material. The choice was motivated by several factors, including its cost-effectiveness, natural abundance, compatibility with zinc oxide, and its stability, transparency, and excellent electrical conductivity, as substantiated in existing literature[165].

The introduction of the doping agent enabled a more nuanced study of zinc oxide samples, leading to the following investigations in this chapter (published as Ref.[166]):

- Prove that there is a mathematical relationship between spectroscopic parameters (ψ and Δ) and photoelectric properties (mobility, charge density, resistivity, gap energy).
- Analyzing ψ and Δ spectra of zinc oxide samples to understand the impact of varying oxygen concentrations on these spectra.
- Representing photoelectric properties of zinc oxide films in terms of ψ and Δ, emphasizing the influence of changing oxygen concentration on these properties.
- Deriving experimental mathematical relationships for optoelectrical properties as a function of ψ and Δ, followed by validating the accuracy of these relationships through comparison with experimental results.
- Generating additional samples of zinc oxide at a fixed oxygen concentration and different deposition temperatures, and then conducting similar studies to assess the impact of temperature variation on the properties under consideration.

2 Experimental method of AZO thin film deposition

We introduced the general idea about the sputtering technique in the previous chapters, whereas, in this section, we want to go into detail about AZO thin film growth via that technique.

AZO thin films were meticulously engineered using the DC magnetron reactive sputtering method. In this process, oxygen gas was introduced, while argon played the role of the sputtering gas during each deposition. Independent mass flow controllers diligently managed and maintained a constant flow rate of 30 standard cubic centimeters per minute (sccm) for both of these gases. To ensure precision, a capacitance vacuum gauge was put to use to monitor and regulate the pressure within

the chamber, consistently maintaining it at a precise 2 (mTorr). Notably, the AJA chamber was equipped with a turbo-molecular pump capable of a maximum pumping speed of 315 liters per second (l/s).

In the pursuit of top-notch uniformity and as a means to mitigate any negative impacts from the bombardment of oxygen ions, the samples were strategically placed at a relatively substantial sputtering distance of 122 millimeters. Moreover, they were set into rotational motion at a speed of 45 (rpm).

Two series of AZO involved the utilization of a specific target: $Zn_{98.68}Al_{1.32}$, boasting a remarkable purity level of 99.99%.

- First series is AZO, composed of samples deposited under different oxygen concentrations (10, 15, 20, 25, 30, and 35%), all depositions took place at room temperature. In the sputtering process, a precise mixture of argon and oxygen was employed, with individual mass flow controllers governing the flow rates of O_2 and Ar gases.
- Second series, like the first one, is composed of AZO samples which were deposited under different temperatures (20, 60, 100, 140, 180 and 220ºC). The oxygen concentration was maintained constant (20%) for all the deposits of this series.

Notably, the electric current was kept at a constant value of 125 mA. These thin films were meticulously deposited onto 2.5x2.5 $cm^2$and 380-micrometer tick oxidized silicon substrates. Following the deposition process, the thickness of the films was accurately determined using an advanced Zeiss Ultra 55 field emission gun scanning electron microscope (FEGSEM).

For the first series, the thin film thickness is shown in Table IV.1:

AZO deposits	S_1	S_2	S_3	S_4	S_5	S_6
$O_2/(Ar+O_2)$ (%)	10	15	20	25	30	35
Thickness d (nm)	343	347	337	333	339	384

Table IV. 1: Thickness of AZO samples (Sn) deposited at ambient temperature, and various oxygen concentrations, by DC magnetron reactive sputtering method.

The samples, denoted as S_1, S_2, … S_6 are labeled in accordance with their respective oxygen concentrations. These designations will be consistently used throughout the entirety of this study.

Table IV.1 displays the thickness of AZO samples that were deposited under different oxygen concentration levels. The samples S_1, S_2, S_3, S_4, and S_5 are close to each other in terms of thickness, with an average of 339.8 nm. This average value enables us to write for all the series:
d = (340 ± 7) nm. So, we will consider the value of the thickness to be constant over the entire experiment ($Error_{max}$ = 2%). As for sample S6 at 35% oxygen concentration, it has a high thickness, but we'll maintain it and consider it as a control point and see through it the effect of

the thickness on each studied parameter. For a clear view of the different thicknesses of samples, see Fig IV.1.

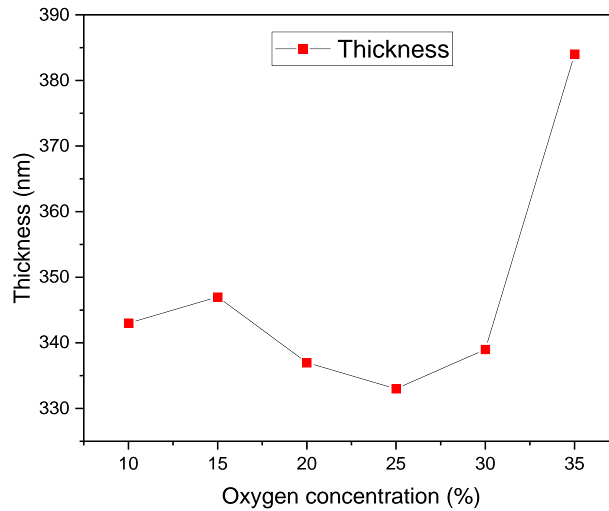

Figure IV. 1: Thickness of AZO samples parameterized as a function of oxygen concentration.

Table 4.2 shows the thickness of the second series of thin films. As we mentioned previously the thickness varies slightly, except for S5 and S6 samples (See Fig. IV.2). Let us assume that it is constant throughout the experiment to remove the thickness difference factor.

AZO deposits	S_1	S_2	S_3	S_4	S_5	S_6
Deposition temperature T_d (°C)	20	60	100	140	180	220
Layer thickness d (nm)	328	334	325	328	355	355

Table IV. 2: Thickness of AZO samples (Sn) deposited at various temperatures, with a 20% oxygen concentration.

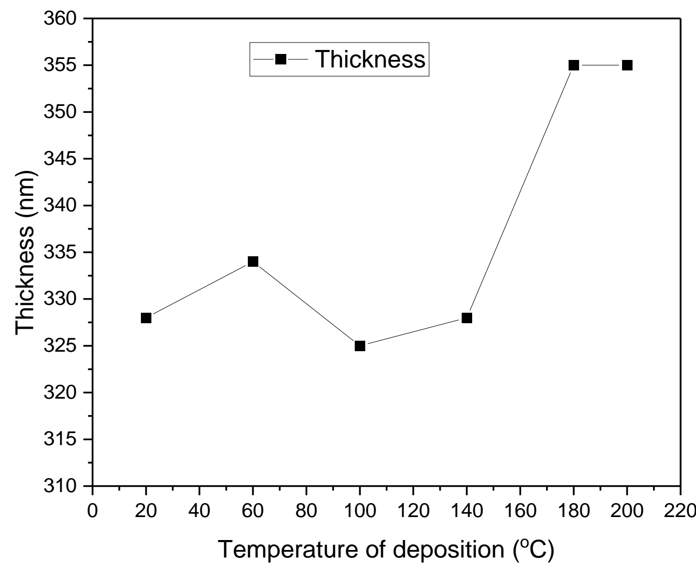

Figure IV. 2: Plot of AZO samples thickness versus deposition temperature, with a 20% oxygen concentration.

To delve deeper into the study of these thin films, critical measurements were taken to extract the charge carrier density and mobility. This involved conducting Hall measurements in the van der Pauw geometry, by using a magnetic field of precisely 0.55 Tesla (T), generated by a permanent magnet. These measurements were skillfully carried out using the high-precision HMS-3000 equipment from Microworld.

3 Results and discussions

Like the ZnO thin films in the previous chapter, SE measurement on AZO thin films produced two main spectra as a function of λ wavelength, the first was about the angle ψ(λ), and the second was the phase difference Δ(λ), (See Fig IV.3 and Fig IV.4). Our study has primarily concentrated on analyzing spectra, specifically investigating the impact of varying oxygen concentrations on thin films. This involves examining changes in the ψ peaks and the displacement λ of Δ at both the peaks and the base of the Δ spectra. The Δ spectrum usually has the same λ value of the successive lower and upper parts of the spectrum, this means that $\lambda_{\Delta max}=\lambda_{\Delta min}$. For that, we will consider it a distinctive value to study the different parameter characteristics of AZO thin film as a function of that wavelength for all samples and extract some interesting relationships.

To do so, we get (ψ_{max1}, ψ_{max2}…., ψ_{min1}, ψ_{min2}….) from ψ spectrum, and we get ($\lambda_{\Delta 1}$, $\lambda_{\Delta 2}$) from Δ spectrum, and we will merge them with the optoelectrical properties (resistivity, mobility, bandgap energy….), then we will make the analyze and discussion of the results.

We would like to emphasize that our discussion is currently focused solely on the first series. We acknowledge that the identical steps will be applied to the second series, and therefore, we may not delve into it in the upcoming chapter dedicated to the second series.

Overall, in this chapter, we will follow the following steps:

- The optoelectrical properties of the samples were measured as a function of the oxygen concentration for each sample.
- Spectroscopic ellipsometry measurements were performed on all the samples, to obtain $\Delta(\lambda)$ and $\psi(\lambda)$ spectra.

As for $\psi(\lambda)$ spectra:

- The $\psi(\lambda)$ peaks spectra were plotted as a function of oxygen concentrations using the same plotting steps in Fig III.3 in the previous chapter.
- Now there are two curves with the same function (1st curve is ψ_{max} versus O_2, and the 2nd is property versus O_2). Taking the oxygen concentration as an intermediary between the two curves. Therefore, we can obtain curves for ψ_{max} as a function of optoelectrical properties.

As for $\Delta(\lambda)$spectra:

- The $\Delta(\lambda)$ spectra displacement was plotted as a function of oxygen concentration using the same plotting steps as in Fig III.6 in the previous chapter.
- Now there are two curves with the same function ($\lambda\Delta$ versus O_2 curve, and electrical property versus O_2 curve).
- Taking the oxygen concentration as an intermediary between the two curves, we can obtain curves for $\lambda_\Delta$as a function of electrical properties.

Since the hybrid curves of (ψ_{max} as a function of the electro-optical properties, λ_Δ as a function of the electrical properties) have familiar shapes, we perform a fitting to extract the relationship between the ellipsometric ellipse scaling parameter (ψ_{max}, or wavelength λ_Δ) and the photo-optical properties of the AZO thin film. However, these relationships can be used as a basis for calculating the optoelectrical properties of the AZO thin film under our experimental conditions. Subsequently, after extracting the equations, we consider the method that infers the properties of thin films via our relationships and then compare them with the experimental results.

Before all of that, there's a physical or mathematical relation between SE parameters and the optoelectrical properties of the thin film?

3.1 Spectroscopic ellipsometry and optoelectrical properties at the theoretical level

From the fundamental equations SE in the previous chapter, we can get a link between SE parameters (ψ, Δ) and optoelectrical properties (resistivity, mobility, bandgap energy, refractive index, light absorbance, etc.).

The film phase thickness is defined by the complex coefficient β from Eq. (II.2), as follows[167]:

$$\beta = 2\pi\left(\frac{d}{\lambda}\right)N\ \cos\varphi \tag{IV.1}$$

where d is the film thickness, λ is the wavelength, N = n ± ik is the complex refractive index, and φ is the incidence angle [138].

That equation is linked to:

- Charge carrier's density (n), and mobility (μ) by Drude's model:
  Drude's model allows us to express the complex permittivity of a dielectric medium $\tilde{\varepsilon}$, as a function of the charge carrier's density, and mobility [3],as follows:

$$\varepsilon_{(\omega)} = N^{2} = \varepsilon + \frac{-1 + i\ /\tau\omega}{1+\omega^{2}\tau^{2}}\ \frac{n\,\mu^{2}m^{*}}{\varepsilon_{0}} \tag{IV.2}$$

  Where ω, τ, μ, n, ε_o and m* are pulsation of radiation, relaxation time, mobility, charge carrier's density, permittivity of free space, and free carrier effective mass, respectively.

- Bandgap by Reddy's relation[168], as follows:

$$Eg = 154\ \mathrm{n}^{-4} + 0.356 \tag{IV.3}$$

  Where n and Eg are respectively the refractive index and energy gap.

  Such a relation is reliable in the range 1.1 eV < Eg < 6.2 eV. About that, it is noticeable that AZO is a material with a wide bandgap (3.3-3.8 eV) [169].This means that our semiconductor's gap energy is within the validity interval.

Creating a precise mathematical equation that links thin film photoelectric properties with spectroscopic ellipsometry is a significant challenge. It becomes more complex when aiming to establish easily applicable relationships for calculations instead of traditional measurements. Achieving this requires advanced mathematical techniques, and the potential for success in the near future is promising with the integration of artificial intelligence.

The complexity of the task increases with the number of layers in the sample. In our exploration of such relationships, like those connecting spectroscopic ellipsometry to charge concentration, mobility, or energy gap, we have developed detailed equations.

The process for obtaining these relationships can be summarized as follows:

From Eq. IV.1:

$$\frac{|R^p|}{|R^s|} = \tan\psi \tag{IV.4}$$

Where: (All parameters are named in Chapter II, section 2)

- To extract ψ (n, μ) relationship:
  with considering Equation IV.2 and Equation IV.1, Eq. IV.4 became:

$$\frac{|R^p|}{|R^s|} = \frac{\left|\dfrac{\tilde{r}_{12}^{\,p} + \tilde{r}_{23}^{\,p}\exp(-2i\beta)}{1+\tilde{r}_{12}^{\,p}\tilde{r}_{23}^{\,p}\exp(-2i\beta)}\right|}{\left|\dfrac{\tilde{r}_{12}^{\,s} + \tilde{r}_{23}^{\,s}\exp(-2i\beta)}{1+\tilde{r}_{12}^{\,s}\tilde{r}_{23}^{\,s}\exp(-2i\beta)}\right|} = \frac{\left|\dfrac{\tilde{r}_{12}^{\,p} + \tilde{r}_{23}^{\,p}\exp\left(-4i\pi\left(\frac{d}{\lambda}\right)N\cos\varphi\right)}{1+\tilde{r}_{12}^{\,p}\tilde{r}_{23}^{\,p}\exp\left(-4i\pi\left(\frac{d}{\lambda}\right)N\cos\varphi\right)}\right|}{\left|\dfrac{\tilde{r}_{12}^{\,s} + \tilde{r}_{23}^{\,s}\exp\left(-4i\pi\left(\frac{d}{\lambda}\right)N\cos\varphi\right)}{1+\tilde{r}_{12}^{\,s}\tilde{r}_{23}^{\,s}\exp\left(-4i\pi\left(\frac{d}{\lambda}\right)\widetilde{N\cos\varphi}\right)}\right|} \tag{IV.5}$$

With relation IV.2, Eq IV.5 became:

$$\psi(n,\mu) = \arctan\frac{\left|\left(\tilde{r}_{12}^{\,p} + \tilde{r}_{23}^{\,p}\exp\left(\frac{-4i\pi d}{\lambda}\sqrt{\varepsilon + \frac{-1+{}^{i}\!/_{\tau\omega}}{1+\tau^2\omega^2}\frac{n\mu^2 m^*}{\varepsilon_0}}\cos\varphi\right)\right)\left(1+\tilde{r}_{12}^{\,s}\tilde{r}_{23}^{\,s}\exp\left(\frac{-4i\pi d}{\lambda}\sqrt{\varepsilon + \frac{-1+{}^{i}\!/_{\tau\omega}}{1+\tau^2\omega^2}\frac{n\mu^2 m^*}{\varepsilon_0}}\cos\varphi\right)\right)\right|}{\left|\left(1+\tilde{r}_{12}^{\,p}\tilde{r}_{23}^{\,p}\exp\left(\frac{-4i\pi d}{\lambda}\sqrt{\varepsilon + \frac{-1+{}^{i}\!/_{\tau\omega}}{1+\tau^2\omega^2}\frac{n\mu^2 m^*}{\varepsilon_0}}\cos\varphi\right)\right)\left(\tilde{r}_{12}^{\,s} + \tilde{r}_{23}^{\,s}\exp\left(\frac{-4i\pi d}{\lambda}\sqrt{\varepsilon + \frac{-1+{}^{i}\!/_{\tau\omega}}{1+\tau^2\omega^2}\frac{n\mu^2 m^*}{\varepsilon_0}}\cos\varphi\right)\right)\right|} \tag{IV.6}$$

Equation IV.6: Represent the theoretical relationship of ψ as a function of charge carriers density n, and mobility μ. From this relationship, the ψ as a function of conductivity property (σ)can also be extracted.

- To extract ψ(Eg) relationship, we use the Reddy's relation Eq IV.3 and Eq IV.5:

$$\psi(Eg) = \arctan\frac{\left|\left(\tilde{r}_{12}^{\,p} + \tilde{r}_{23}^{\,p}\exp\left(-4i\pi d\cos\varphi\frac{(Eg-0.356)^{-\frac{1}{4}}}{154^{-\frac{1}{4}}\lambda}\right)\right)\left(1+\tilde{r}_{12}^{\,s}\tilde{r}_{23}^{\,s}\exp\left(-4i\pi d\cos\varphi\frac{(Eg-0.356)^{-\frac{1}{4}}}{154^{-\frac{1}{4}}\lambda}\right)\right)\right|}{\left|\left(1+\tilde{r}_{12}^{\,p}\tilde{r}_{23}^{\,p}\exp\left(-4i\pi d\cos\varphi\frac{(Eg-0.356)^{-\frac{1}{4}}}{154^{-\frac{1}{4}}\lambda}\right)\right)\left(\tilde{r}_{12}^{\,s} + \tilde{r}_{23}^{\,s}\exp\left(-4i\pi d\cos\varphi\frac{(Eg-0.356)^{-\frac{1}{4}}}{154^{-\frac{1}{4}}\lambda}\right)\right)\right|} \tag{IV.7}$$

Equation IV.7: Represent the theoretical relationship of ψ as a function of gap energy.

In three-layer samples similar to ours, obtaining a mathematical derivation would be easy if ψ were a function of the property. However, when the property is expressed as a function of ψ, the challenge arises. Finding the relationship of the property as a function of ψ is our primary objective. This connection is crucial for directly extracting thin film properties from the SE measurement. Consequently, fitting will be employed to establish ψ relationships in terms of electro-optical properties.

Taking into account that the same procedure applies to property relations as a function of λ_{Δ}, or vice versa. Since Δ is inherently proportional to ψ, the connection of Δ to photoelectric properties has become evident too, eliminating the need for further demonstration as the same steps can be followed.

3.2 Variation of oxygen concentrations

3.2.1 Spectroscopic ellipsometry measurement

Ellipsometry experiments were performed on AZO samples, to record the Ψ and Δ spectra. For the first series, the resulting curves are parameterized with the oxygen concentration during the deposition process.

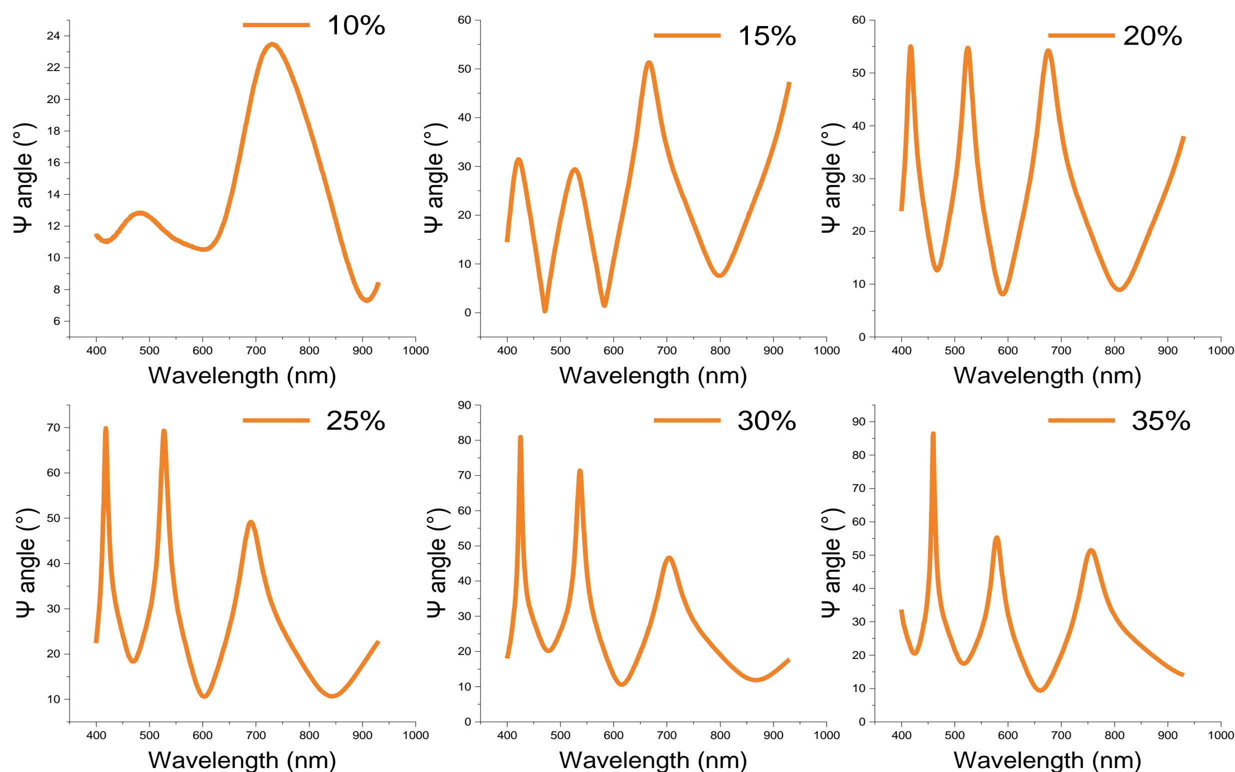

Figure IV. 3: Different curves of ellipsometric ψ angles versus wavelength λ of AZO thin films prepared at different O_2 concentrations.

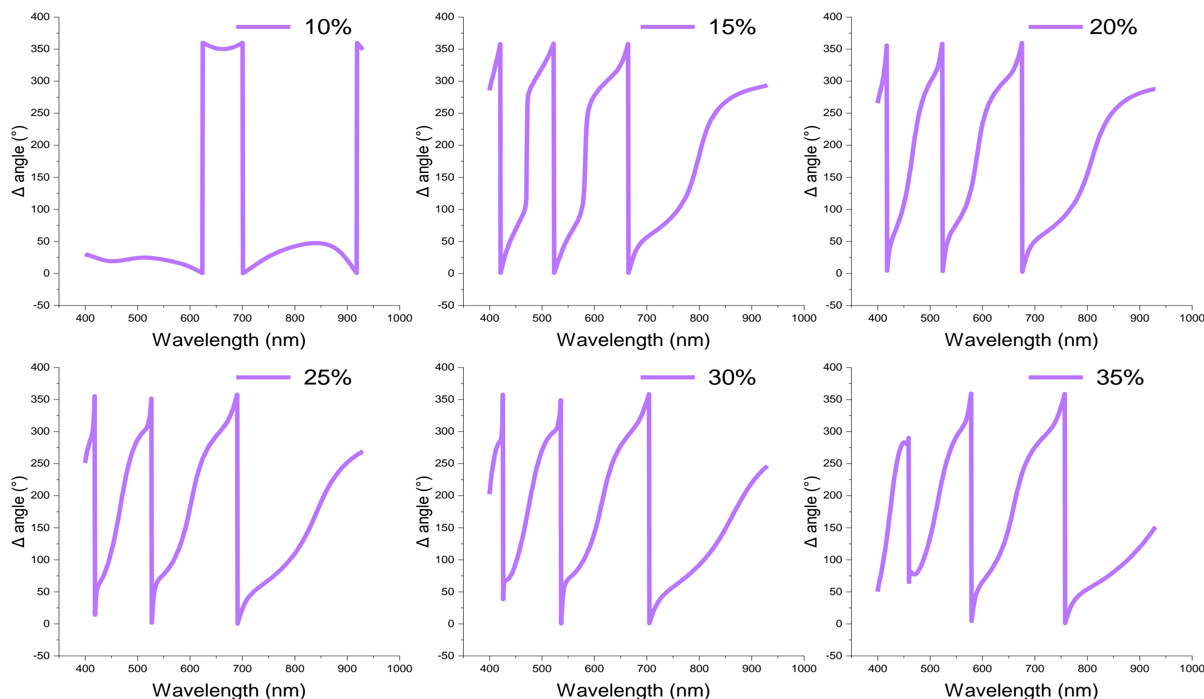

Figure IV. 4: Different curves of ellipsometry Δ angles versus wavelength λ of AZO thin films prepared at different oxygen concentrations.

The amplitude ψ spectra curves show a dissimilarity in evolution, number of oscitations, and their disparity of peaks. Also, there is a difference in the breadth between peaks. That dissimilarity mainly rests on the increase of oxygen concentration during deposition (see Figure IV.3).

However, this phenomenon occurred at Δ curves but was less severe. When the spectra are grouped in one curve, the differences between them appear more clearly, as will be seen later. When taking a look at ψ and Δ spectra sample of 10% oxygen concentration Figures IV.3 and IV.4, we can see a big difference shape from the rest of the spectra. This is maybe due to the great number of Zn clusters in the sample structure, and moreover the material still owns a metal mode.

Let's plot together on the same ψ-λ frame of reference, the different curves of ellipsometric ψ angles of AZO thin films, elaborated at different O_2 concentrations, as shown in the figure below (Figure IV.5).

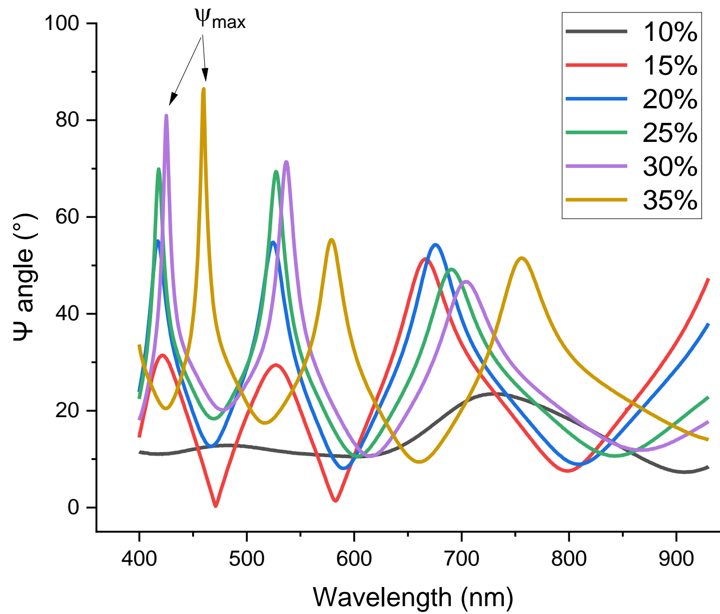

Figure IV. 5: Ellipsometry ψ angles taken from AZO thin films prepared at different O_2 concentrations.

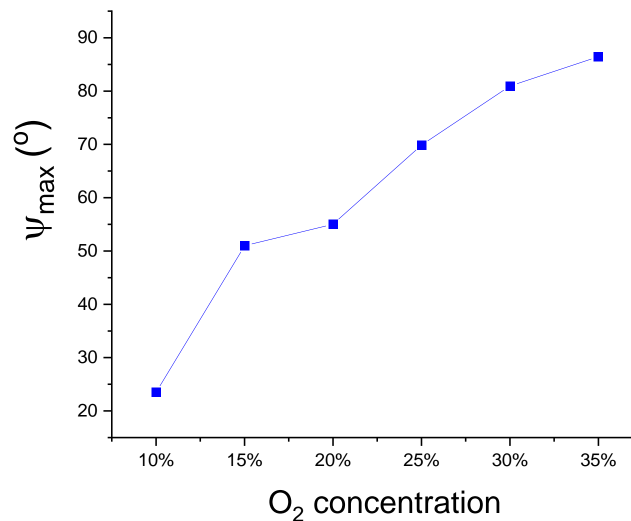

Figure IV. 6: ψ_{max} values of AZO thin films spectra as a function of oxygen concentration.

From Figure IV.5 we can see that there are different oscillations on Ψ spectral evolution. As the wavelength changes, the interference position shifts, giving rise to the up-and-down data fluctuations[167]. The number and position of interference features depend mainly on film characteristics like thickness and refractive index, where the increase in either thickness or film

index produces more interference features[138]. The variation in the position of the interference features is very clear as in Figure IV.5.

To further clarify the vision, we have plotted the peak values of Ψ spectra (Ψ_{max}) versus oxygen concentration (see Fig. IV.6), It gives a clearer picture of the fact that oxygen concentration in the sample is related to Ψ_{max}. More than that, it shows indirectly the effect of the increasing of oxygen rate on the structure of the samples. Indeed, when oxygen rate is raised it gives rise to increasing of oxygen-zinc bonds number leading to a better surface reflectivity. The relationship between the two phenomena can be translated into a simple a mathematical relationship. To do so, we plot the neperian logarithm of the oxygen concentration rate versus Ψ angle maxima values (Figure IV.7).

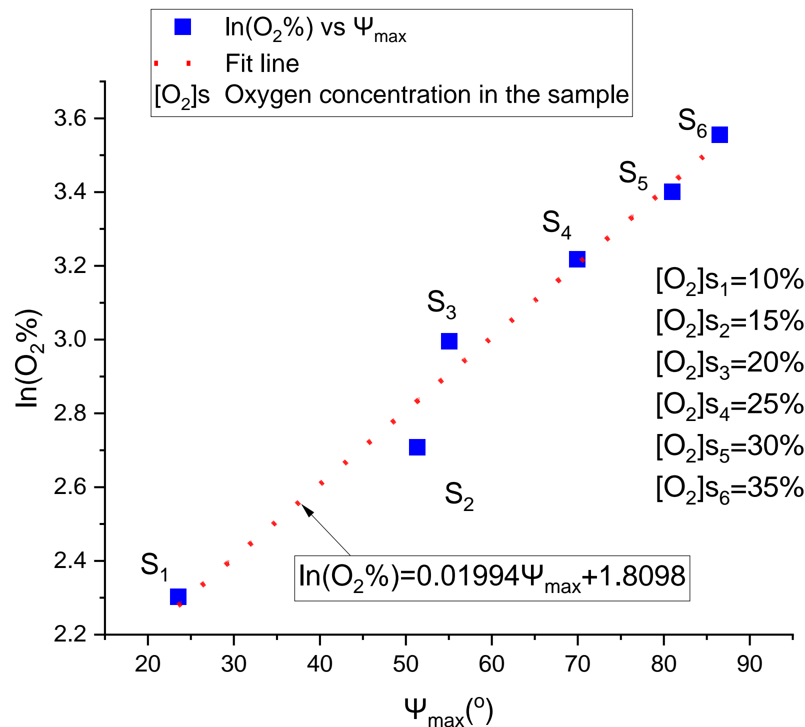

Figure IV. 7: Logarithm of oxygen concentration evolution versus Ψ angle extrema.

As shown in Figure IV.7, The evolution of the of oxygen concentration logarithm as a function of Ψ_{max} angle maxima values gives an interesting form, from which a simple and useful equation can be derived:

$$\ln(O_2\%) = 1.8098 + 0.01994\ \psi_{max} \tag{IV.8}$$

Taking into account that this equation is valid under experimental conditions, the wavelength range is from 417 to 730nm, Ψ_{max} angles range is [23.50°, 80.96°], and average thickness is 340nm with uncertainty error of 4.81%. The accuracy of this relationship is analyzed in Table IV.3

Sample	Ln(O_2%)$_{meas}$	Ln(O_2%) withΨ_{max} method	Relative error (%)
S1$_{10\%\ O2}$	2.3	2.27	1.3
S2$_{15\%\ O2}$	2.7	2.83	4.81
S3$_{20\%\ O2}$	2.99	2.9	3.01
S4$_{25\%\ O2}$	3.21	3.2	0.31
S5$_{30\%\ O2}$	3.40	3.42	0.58

Table IV. 3: Comparison between measured and calculated AZO thin film oxygen concentration for "Ψ_{max} method".

From the above, it may be possible to rely on the change of Ψ_{max} and consider it in a sensor for the oxygen concentration variation. It makes also possible to incorporate the device inside the depositing chamber through in-situ non-contact ellipsometry measurement on the samples. If we plot together on the same Δ-λ frame of reference, the different curves of ellipsometric Δ angles of AZO thin films, elaborated at different O_2 concentrations, we'll obtain the figure below (Figure IV.8)

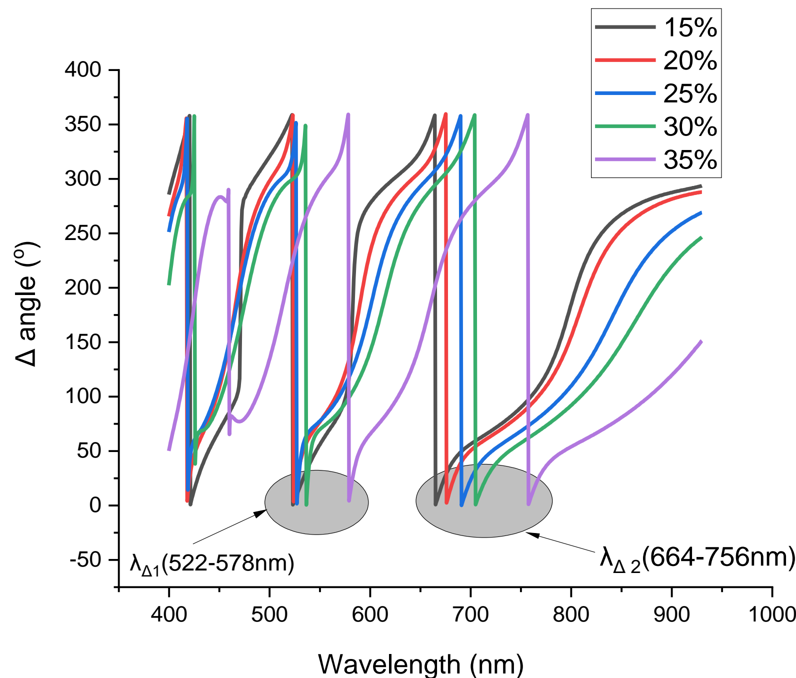

Figure IV. 8: Delta spectra as function of wavelength, of different AZO samples made with several oxygen concentration.

Figure IV.8 represents the curves of ellipsometric phase difference Δ spectra, as function of wavelength λ, for different AZO samples produced under several oxygen concentrations. We can see that Δ spectra pull back towards the long wavelength whenever an oxygen rate increases. Actually, the increase in the amount of oxidation has an effect on the morphology of the material, and this is evident through the change in the Δ spectra from one sample to another. because the phase Δ is very susceptible to changes when modifying the structure of matter.

From Figure IV.8, we can raise two lambda particular values ($\lambda_{\Delta 1}$ and $\lambda_{\Delta 2}$), set on wavelength intervals ranging from 664 to756 nm, and from 522 to 578 nm respectively.

3.2.2 Electrical properties

As commonly understood, the electrical resistivity in semiconductors is inversely proportional to the product of carrier concentration (n) and mobility (μ). The influence of oxygen concentration on the electrical characteristics of AZO thin films has been extensively documented in the literature [170, 171].

In our discussion, we haven't touched upon acceptor impurities or holes. This is because, it's well-known that when Aluminium (Al) is incorporated into Zinc Oxide, it behaves as a donor impurity, contributing extra electrons[172].These surplus electrons enhance the electron concentration in the substance, leading to n-type characteristics[173].

The primary motivation for this study stems from the recognized interdependence between electrical and optical properties, as indicated by Drude's model of the complex refractive index [174]. The observed variations in charge carrier density, resistivity, and corresponding fluctuations in mobility concerning the Ψ_{max} angle are attributed to variations in oxygen concentration, as illustrated in Figures (IV.9), (IV.10), and (IV.11).

At low oxygen concentration levels, the charge carrier density is high, due to the presence of zinc cluster groups in the samples. This diminishes resistivity because zinc clusters act as defects that impede electron movement, thus reducing mobility. With an increase in oxygen concentration, there is an apparent decrease in charge carrier density due to a reduction in zinc clusters. This contributes to enhanced conductivity and an improvement in electron mobility.

Further elevation in oxygen concentration leads to the formation of Al_2O_3 clusters while reducing zinc clusters. This results in an increased resistivity of the samples, accompanied by a subsequent decline in mobility. The intricate relationship between oxygen concentration, the presence of clusters, and the resulting impact on the electrical properties of AZO thin films underscores the complexity of these interactions.

The evolution of charge carrier density versus ellipsometric angle maxima values Ψ_{max} for AZO deposits, parameterized with oxygen concentration rate, is plotted in Figure IV.9 below:

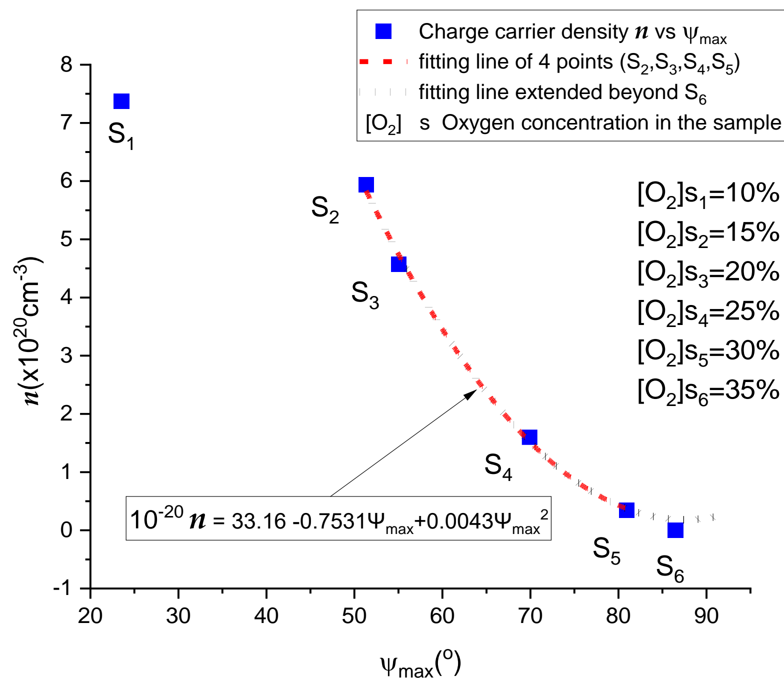

Figure IV. 9: Evolution of charge carrier density versus Ψ_{max} angles for different AZO samples, showing the equation of the fitting curve.

Figure IV.9 illustrates the relationship between the charge carrier density and the maximum values of the Ψ angle. It is noteworthy that the charge carrier density for the first sample was excluded from the fitting process due to its considerable deviation from the others, indicative of a metallic behavior. Notably, the experimental point for the last sample, S_6 (the control sample), closely aligns with the fitted line and exhibits a similar pattern to the other thin films, despite variations in thickness. The polynomial equation derived from the curve, providing the optimal fit for the experimental data, is expressed as follows:

$$n = 33.16 - 0.7531\ \psi_{max} + 0.0043\ \psi_{max}^{2} \qquad (x10^{20}cm^{-3}) \tag{IV.9}$$

The validity limits of this relationship are from 417 to 665 nm for wavelength, and [51.32°; 80.96°] for Ψ_{max}, with fairly acceptable accuracy (relative error below 9 %) as shown in Table IV.4.

The evolution of resistivity versus ellipsometric angle maxima values Ψ_{max} for AZO deposits, parameterized with oxygen concentration rate, is plotted in Figure IV.9 below:

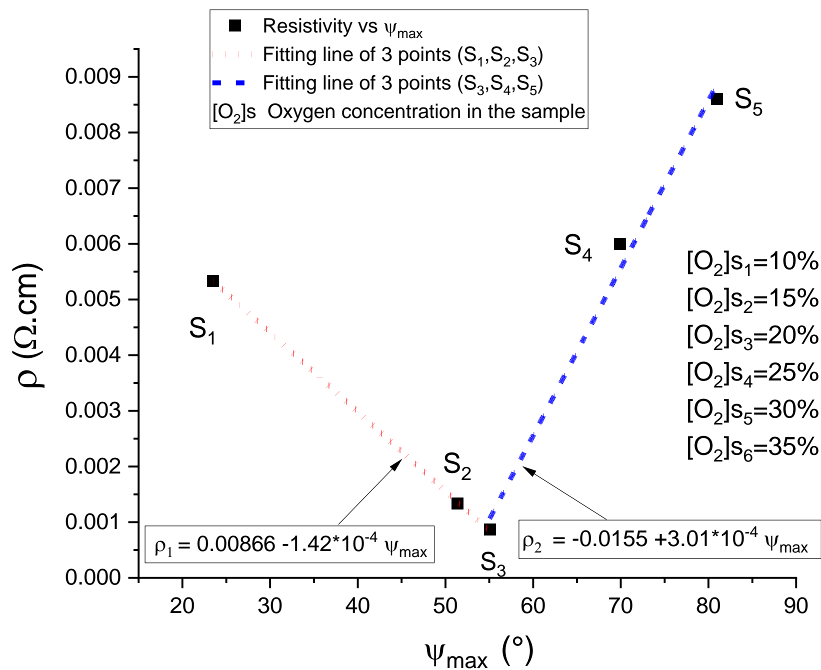

Figure IV. 10: Evolution of resistivity as a function of Ψ_{max} angles for different AZO samples without S6 (resistive behavior).

Figure IV.10 represents the resistivity of AZO thin film versus Ψ_{max} angles for different samples (without control sample S_6). The resistivity value of the latter sample was excluded due to its significantly larger magnitude compared to the other samples. Including it would distort the overall curve shape, so we only mention its value here (ρS6 = 6 Ω.cm).

To simplify the shape of the curve, we divided it into two straight lines with opposite slopes, as it is clearly shown in Figure IV.10. Then we fit each slit separately to get the following two linear equations:

$$\rho_1 = 0.0086 - 1.42 * 10^{-4}\, \psi_{max} \quad (\Omega.\text{cm}) \tag{IV.10}$$

$$\rho_2 = -0.155 + 3.01 * 10^{-4}\, \psi_{max} \quad (\Omega.\text{cm}) \tag{IV.10'}$$

Validity limits of Eq. IV.10 are from 417 to 730 nm for wavelength and [23.5°;55.05°] for Ψ_{max}, with accuracy is considered average. (Relative error below 9 %, see Table IV.4), and intervals validity of Eq. IV.10' is from 417 to 425 nm for wavelength, and [55.05°; 80.96°] for Ψ_{max}, with good accuracy (relative error bellow 4 %) as shown in Table IV.4

The evolution of mobility versus ellipsometric angle maxima values Ψmax for AZO deposits, parameterized with oxygen concentration rate, is plotted in Figure IV.11 below:

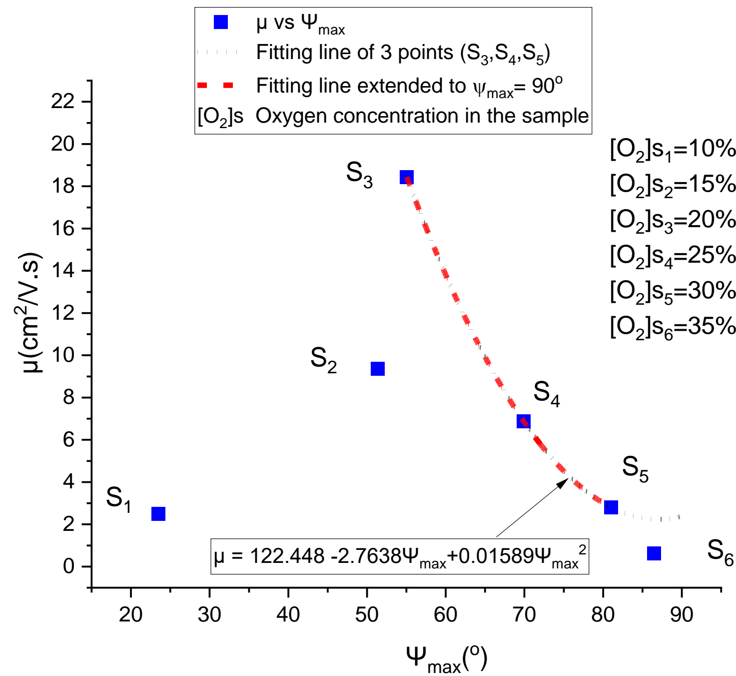

Figure IV. 11: Evolution of mobility as a function of ellipsometric Ψ_{max} angles for different AZO samples.

Figure IV.11 points out that the evolution of electron mobility curve, as function of Ψ_{max} angles, for Aluminum-doped ZnO deposits is divided into two parts increasing and decreasing. Since this mobility curve is rather complicated, we fit only decreasing part of the curve (S3, S4, and S5), because they are in the same pattern, while the fit of the remaining experimental points gives a complex and not well-known equation. The polynomial equation derived from the curve which shows the best fit of the experimental points is as follows:

$$\mu = 122.448 - 2.7638\ \psi_{max} + 0.01589\ \psi_{max}^2 \qquad (cm^2/V.s) \qquad \text{(IV.11)}$$

The interval of validity limits for this relationship is like Eq. IV.10, with good accuracy (relative error does not exceed 1.06 %) as shown in Tables IV.4

Sample	n charge carrier's density measured (10^{20} cm^{-3})	n charge carrier's density calculatedwith Ψ_{max} method (10^{20} cm^{-3})	Relative error (%)
S1$_{10\%\ O2}$	/	/	/
S2$_{15\%\ O2}$	5.94	5.83	1.85
S3$_{20\%\ O2}$	4.57	4.73	3.5
S4$_{25\%\ O2}$	1.6	1.52	5
S5$_{30\%\ O2}$	0.34	0.37	8.82
Ψ_{max}intrvalles	[51.32°;80°]		

Sample	ρ resistivity measured (Ω.cm)	ρ resistivity calculated with Ψ_{max} method (Ω.cm)	Relative error (%) of ρ
S1$_{10\%\ O2}$	$5.333 * 10^{-3}$	$5.332 * 10^{-3}$	0.01
S2$_{15\%\ O2}$	$1.33 * 10^{-3}$	$1.34 * 10^{-3}$	0.75
S3$_{20\%\ O2}$	$8.66 * 10^{-4}$	$8.4 * 10^{-4}$	3
S4$_{25\%\ O2}$	$6 * 10^{-3}$	$5.5 * 10^{-3}$	8.33
S5$_{30\%\ O2}$	$8.6 * 10^{-3}$	$8.8 * 10^{-3}$	2.32
Ψ_{max}intrvalles	[51.32°;80.96°]		

Sample	μ mobility measured (cm^2/V.s)	μ mobility calculated with Ψ_{max} method (cm^2/V.s)	Relative error (%)
S1$_{10\%\ O2}$	/	/	/
S2$_{15\%\ O2}$	/	/	/
S3$_{20\%\ O2}$	18.44	18.45	0.05
S4$_{25\%\ O2}$	6.87	6.89	0.29
S5$_{30\%\ O2}$	2.81	2.84	1.06
Ψ_{max}intrvalles	[55.05°;80.96°]		

Table IV. 4: Comparison between measured values and calculated ones with the "Ψ_{max} method", of the various AZO deposits. charge carrier density (top), resistivity (middle), and mobility (bottom)

We did not get all the curves clear and smooth, but several curves were distorted and were not suitable for analysis due to the complexity of their shapes. This explains why some characteristic curves are overlooked as function of Ψ_{min} or as function of $\lambda\Delta$ (like resistivity versus $\lambda\Delta$, charge carrier's density versus Ψ_{min}….), as we will see some of them later.

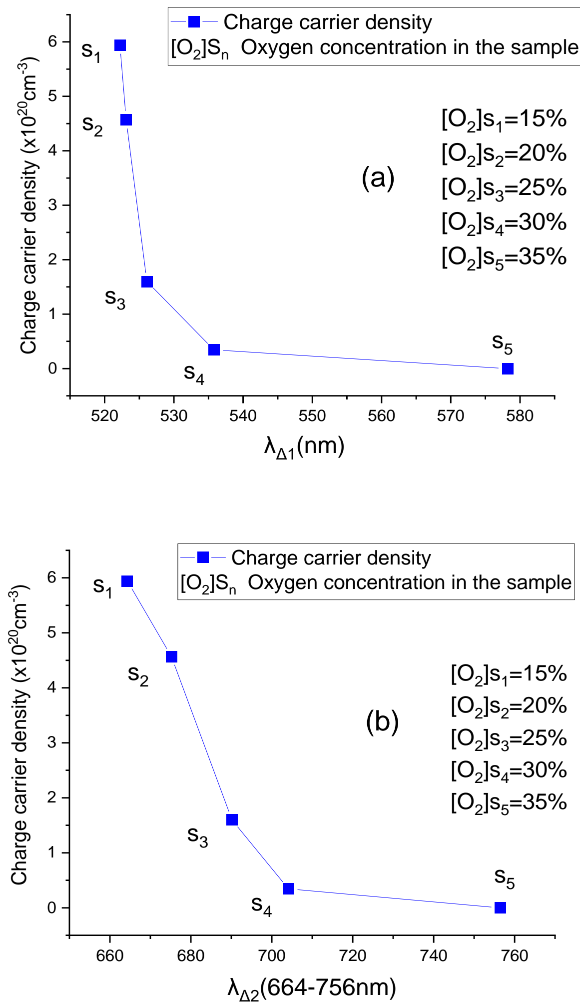

Figure IV. 12: a and b are Curves of Charge carrier density as function of $\lambda_{\Delta 1}$ and $\lambda_{\Delta 2}$ oscillations peaks respectively, for different AZO deposits with different oxygen concentrations.

From Figure IV.12 We can see that the number of charge carriers decreases continuously when the oxygen concentration is increased. Curves (a and b) have the same shape, so what we see in curve (a) is similar to what we see in curve (b).

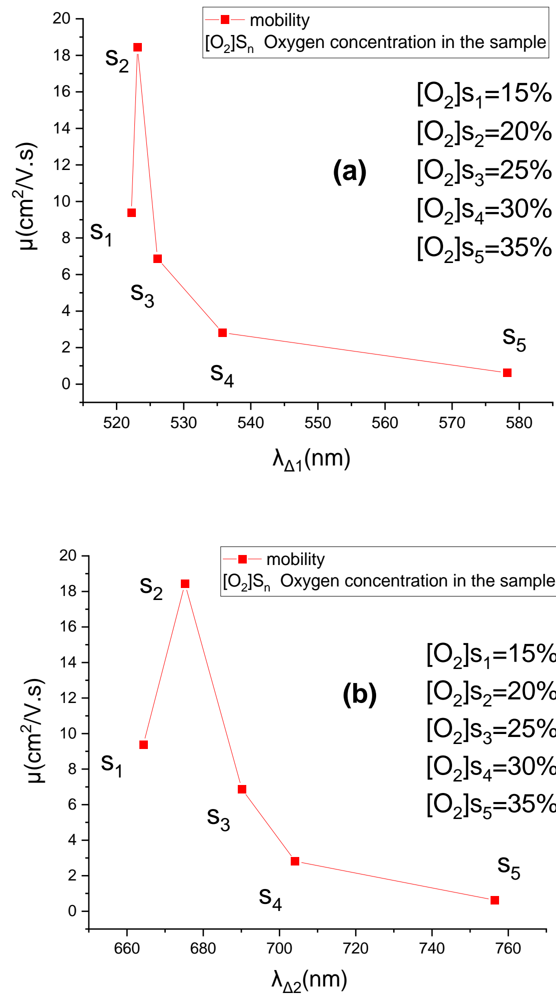

Figure IV. 13: (a and b) are Curves of mobility as function of $\lambda_{\Delta1}$ and $\lambda_{\Delta2}$ oscillations peaks respectively, for different AZO deposits with different oxygen concentrations.

As we explained previously, the changes in charge carrier density and mobility in curves

Figures (IV.12, and IV.13) are explained by the following[169]:

In the first samples, there are small clusters of metallic Zn with a low amount of oxygen. When the concentration of oxygen is increased, these metallic defects decrease significantly, resulting in enhanced mobility. Additionally, the Al atoms continue to function as dopants, contributing to a high electronic density. This increased electronic density facilitates effective screening of the defects, further boosting mobility. On the other hand, when the oxygen concentration is further increased, reaching the oxidized state, a portion of the aluminum forms clusters of Al_2O_3 instead of substituting in the Zn lattice[166]. In this configuration, aluminum no longer acts as a dopant, leading to a decrease in electronic density. Consequently, the reduced electronic density hinders the effective screening of defects, resulting in decreased electronic mobility.

Figures IV.14 (a, b) represent the curves of charge carrier density and resistivity, as function of Ψ_{min} respectively, for different AZO samples with different oxygen concentrations. On the level of curves, the representation of electrical properties versus Ψ_{min} gives no well-interesting curves compared to previous curves which are as function of Ψ_{max}, $\lambda_{\Delta 1}$ and $\lambda_{\Delta 2}$. Indeed, there is no clear specific means to increasing or decreasing properties as a function of Ψ_{min}.

The final sample S_6 was excluded from the resistivity curve due to its exceptionally high resistivity ($\rho_{S6} = 6\ \Omega$.cm), which, if included, would distort the overall curve. Similarly, in the charge carrier density curve, this particular sample exhibited an extremely small value compared to the others ($n_{S6} = 2\text{x}10^{18}$ cm^{-3}), and its inclusion would further distort the curve. Consequently, it was also removed from the charge carrier density curve.

When seeing Fig. IV.14, we may see something strange at first glance, which is that the names of the samples are not arranged in the curves, and this is true because their codes S_1, S_2, ..., S_5, were arranged based on oxygen concentrations (as we saw in Table IV.1) and not arranged on the basis of ψ_{min} values. Therefore, their position in the curves will be according to the order of its coordinates with respect to ψ_{min}, not according to the oxygen concentration.

We only note that this matter may be repeated in some of the following section.

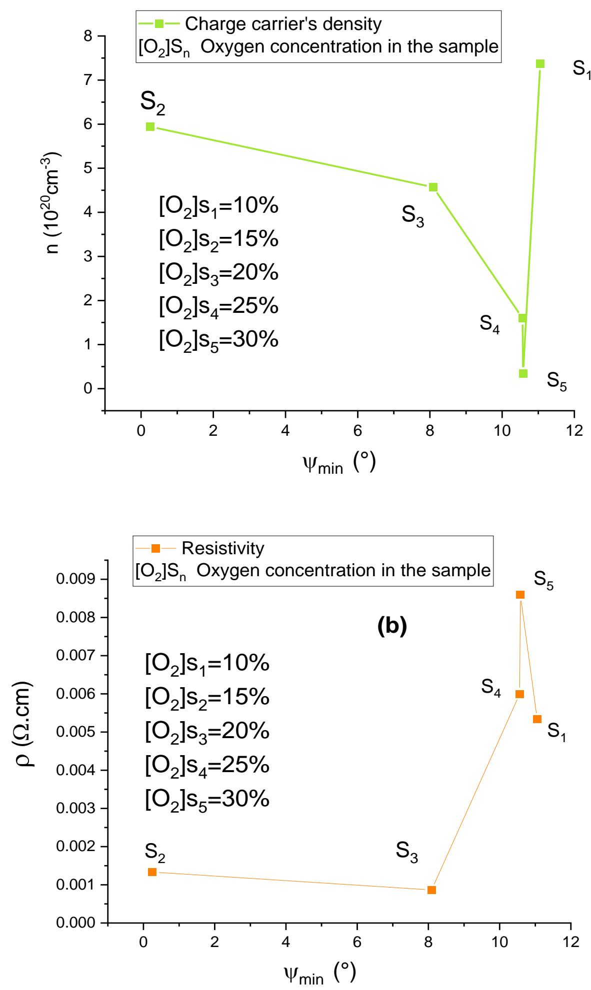

Figure IV. 14: (a, b) are Curves of Charge carrier density and Resistivity, respectively, as function of Ψmin, for different AZO deposits with different oxygen concentrations.

3.2.3 Optical properties

The band gap of AZO was obtained from the optical absorption using Tauc's formula [171]:

$$(\alpha h\nu)^{\frac{1}{k}} = A(h\nu - Eg) \tag{IV.12}$$

Where α is the absorption coefficient, hν is the photon energy, A is a constant, Eg is the optical bandgap, and k is a number relating to the transition process and the energy dependence of the band edge, which equals 1/2 for the direct transitions of AZO thin films [175].
Tauc's plot method was used in all of the cases of the samples. The absorbance was calculated based on the transmission and reflection spectra as shown in reference [176].

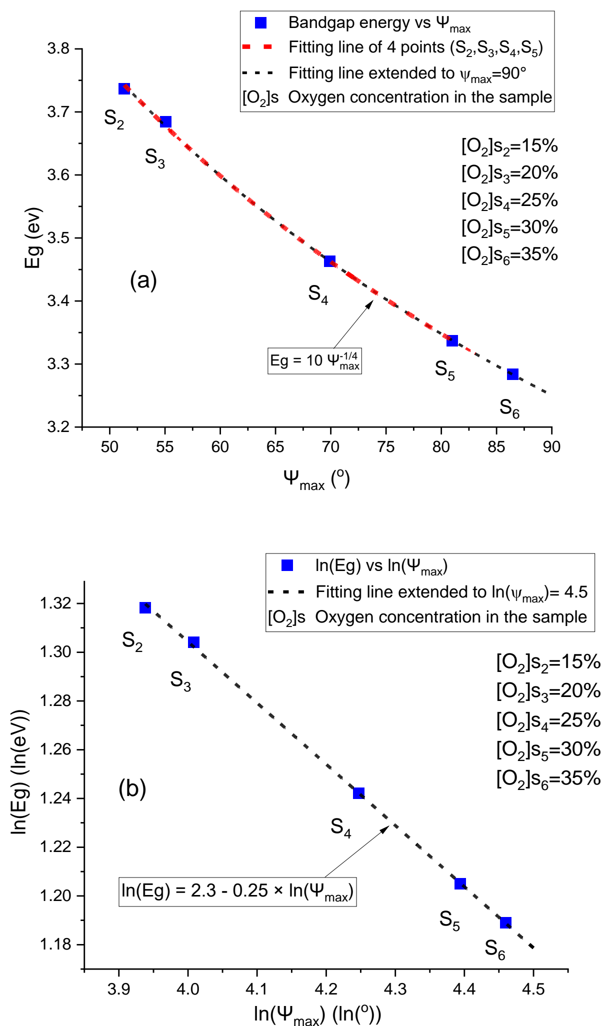

Figure IV. 15: Optical Bandgap energy versus Ψ_{max} for AZO thin films: (a) Experimental points; (b) log-log scale.

Extracted AZO samples Eg values as a function of Ψ_{max} are reported in Figure IV.15 We can see that Eg decreases with increasing of Ψ_{max}. This means that Eg decreases with an increase in oxygen concentration in the plasma. This is due to a significant decrease in charge carrier density, as it has been raised in the present study (see Fig. IV.9). However, this latter is linked to a drop in the Fermi level, and therefore a decrease in the optical bandgap, which is explained by the Burstein–Moss effect, that was observed in degenerate semiconductors[177, 178]. The Burstein-Moss effect refers to the phenomenon in semiconductor physics where the bandgap of a material increases as the charge carrier concentration in the material increases.

Although it has been shown elsewhere[179]that is demonstrated that thickness contributes to an increase in the bandgap energy in AZO, but Figure IV.15 does not reveal a corresponding elevation in the Eg value for the last sample compared to the others. This discrepancy might be attributed to the pronounced influence of oxygen concentration on the bandgap energy, particularly given the relatively small difference in thickness between the last sample and the remaining samples (merely 12% of the overall value).

The curves Fitting (a) and (b) give simple interesting formulas between the two quantities Eg and Ψ_{max}, in one hand, ln (Eg) and ln(Ψ_{max}), in the other hand, as follows:

$$\ln(Eg) = 2.3 - 0.25 * \ln(\psi_{max}) \quad \text{(IV.13)}$$

$$Eg = 10\,\psi_{max}^{-1/4} \quad \text{(IV.14)}$$

Equation IV.13 proves highly accurate, maintaining a relative error within 0.3% across all scenarios (refer to Table IV.5). The Validity range of Equations IV.13 and IV.14, is like equation IV.9. The Bandgap value of the first sample is absent in curve because the latter does not behave like a semiconductor, but like a metal (low Eg).

Sample	Eg(eV) measured	Eg(eV) with Ψ_{max} method	Relative error (%)
S2$_{15\%\ O2}$	3.7368	3.736	0.02
S3$_{20\%\ O2}$	3.68	3.67	0.27
S4$_{25\%\ O2}$	3.46	3.45	0.28
S5$_{30\%\ O2}$	3.336	3.333	0.08
S6$_{35\%\ O2}$	3.28	3.27	0.3

Table IV. 5: Comparison between measured and calculated AZO thin film bandgap energy Eg, in "Ψ_{max} method" case.

Depending on the results of Table IV.5, we can consider that this contactless method is effective and simple at the same time to calculate the bandgap energy Eg.

For example, when taking the linear relationship (Eq. IV.13), it's enough to take two samples from the series and measure their bandgaps energy Eg_1 and Eg_2 by another method, and extract their Ψmax1 and Ψ_{max2} from ellipsometry measurements for the two samples, then draw the straight-line linking the two points ($\ln(Eg_1)$, $\ln(\Psi_{max1})$) and ($\ln(Eg_2)$, $\ln(\Psi_{max2})$), on a xy plane. Next, to extract the bandgap energy Eg_3 value of a third sample, just place the $\ln(\Psi_{max3})$ on the curve.

Amongnumerous advantages of this measurement method, compared to others, is its ease and speed, in-situ or ex-situ implementation, to find the bandgap energy of a large series of samples, with a great accuracy.

Now, if we take the ellipsometric angle minima Ψ_{min}, instead of the maxima values, the experimental points will be distributed like it is shown in Figure IV.16 below

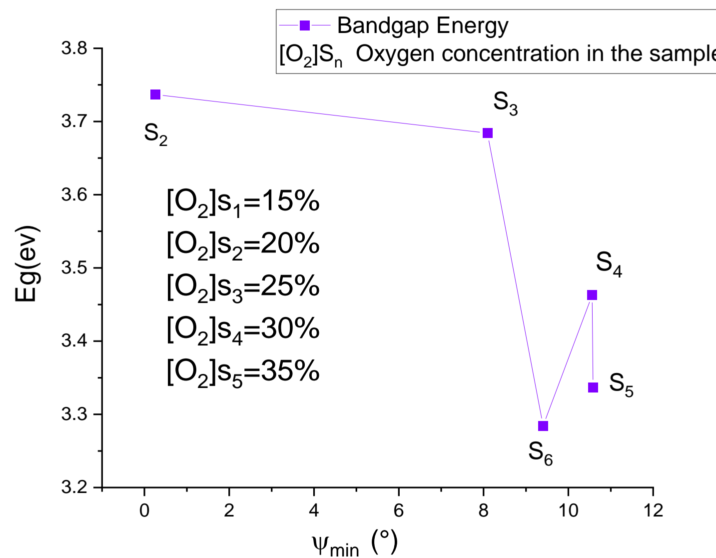

Figure IV. 16: Experimental points of bandgap energy versus Ψ_{min} for AZO thin films.

Figure 4.16 represents the evolution of bandgap energy as function of the ellipsometry parameter Ψ_{min}. Oppositely to the $Eg(\Psi_{max})$ curve, this curve shows a nonregular evolution at bandgap values, which makes analyzing it or extracting the correlation from it not completely clear. This is maybe due to the narrowing of Ψ_{min} range [0.24° to 11°]. Although, as we saw previously, there is a strong theoretical correlation between Eg and Ψ angle.

3.3 Variation of deposition temperature

In the second series of AZO, the oxygen concentration was set to 20%, and was placed around the midpoint of the transition regime, at which level the most desirable properties were available, including high transparency and conductivity (as shown in Figures IV.9, IV.10, and IV.11). Therefore, we will see how its properties are affected by temperature during deposition.

The impact of temperature is more pronounced during deposition compared to annealing as it enhances the mobility of particles at a free surface. In contrast, post-deposition annealing boosts the mobility of atoms embedded in a three-dimensional lattice[169].

Heating during the deposition of AZO thin films using the reactive sputtering magnetron technique offers several benefits[180]:

Enhanced Mobility of Particles[181]*:*

Heating increases the kinetic energy of particles, promoting their mobility on the substrate. This improved mobility contributes to a more uniform and dense deposition of zinc oxide thin films.

Improved Nucleation and Growth[182]*:*

Elevated temperatures during deposition facilitate better nucleation and growth of the thin films. This is essential for achieving a well-defined crystalline structure and desired film properties.

Control of Microstructure[183]*:*

Heating allows for better control over the microstructure of the deposited films. It influences factors such as grain size and orientation, which are crucial for determining the optical and electrical properties of the zinc oxide thin films.

Reduction of Defects[184]*:*

The application of heat can help reduce defects in the thin films by promoting the diffusion and rearrangement of atoms on the substrate surface. This, in turn, contributes to improved film quality.

Enhanced Adhesion[184]*:*

Heating promotes better adhesion between the deposited zinc oxide layer and the substrate. This is particularly important for ensuring the long-term stability and durability of the thin films.

Optimization of Film Properties[185]*:*

Temperature control during deposition allows for the optimization of various film properties, including thickness, roughness, and optical characteristics. This is crucial for tailoring the thin films to specific application requirements.

Increased Reaction Rates:

Higher temperatures can enhance reaction rates between the sputtered zinc atoms and reactive gases, leading to more efficient deposition processes and the formation of high-quality films.

The ellipsometry measurements on the aluminum doped zinc oxide (AZO) films deposited at different temperatures have been taken. The values of amplitude angle Ψ and phase difference Δ, of the polarized reflected light, have been collected and plotted like it is shown in Figure IV.17 (a, b).

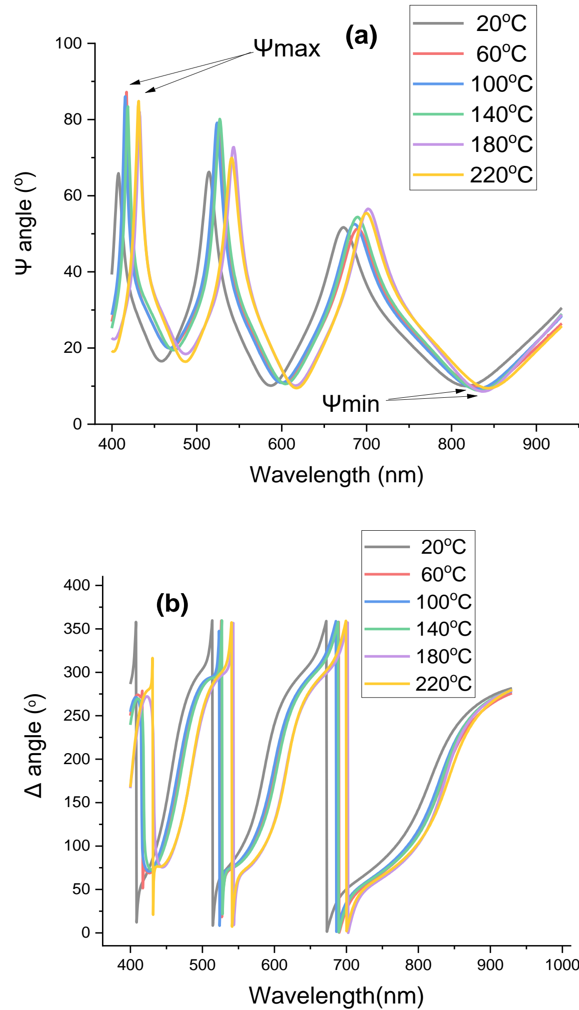

Figure IV. 17: Experimental (a) amplitude component Ψ, and (b) phase difference Δ, of the polarized reflected light from the surface of AZO films deposited at different temperatures.

From the curve in Figure IV.17 (a), it can be seen that the angle Ψ spectrum of different samples is shifted to the long wavelengths by increasing the heating temperature of the samples during deposition. This is shown most clearly in the Δ spectrum in Figure IV.17 (b), which indicates that the heat factor during deposition affects the structure and reflection optical properties of the thin films. It is known that the growth rate of the deposited layers increases with increasing deposition temperature, and this directly controls the molecular structure of the thin films. An improvement in the microstructure of thin films enhances optical and electrical properties, knowing that the amplitude ratio tan (ψ) is closely related to refractive index n, while Δ represents light absorption described by k or the absorption coefficient α[139].

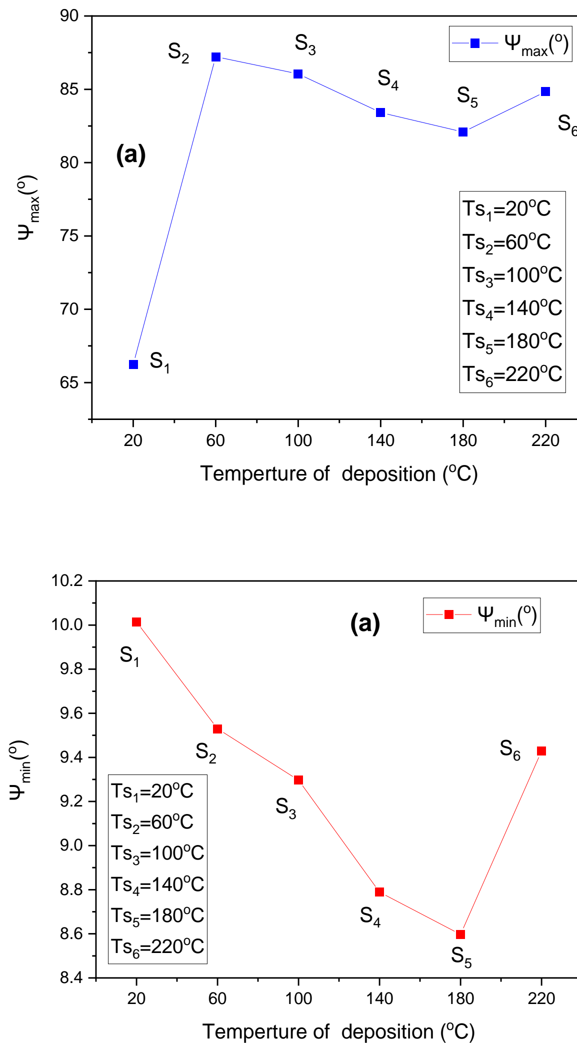

Figure IV. 18: Experimental results collected from the polarized reflected light on the surface of AZO films and plotted as a function of the deposition temperature: (a) maximum amplitude component Ψ_{max}; (b) minimum amplitude component Ψ_{min}.

The increase in temperature does not only affect the withdrawal of the Ψ spectra towards the longer wavelength, as we saw in Figure IV.17, but can also affect the maxima and minima Ψ values.

In general, it may take the form of a linear function, allowing it to be easily studied (Figure IV.18 (a, b)).

3.3.1 Electrical properties

In this part, we will see the mobility and resistivity curves in terms of Ψ. Since our curves are in terms of Ψ (and since one of the purposes of creating them is to extract easy relationships), they will not explain the correlation between optoelectrical properties and temperatures enough. But we are talking about the general case only.

Regarding the examination of the influence of temperature variations on the mobility and resistivity levels in samples, as outlined in reference[180], the electronic properties of zinc oxide samples undergo alterations based on the temperature conditions during the deposition process.

This phenomenon can be attributed to various internal factors, primarily stemming from defects such as interstitial Zn and grain boundaries, as well as the activation of aluminum dopants[169].

The reduction in resistivity is explicable through the concurrent increase in charge carrier density and mobility [184]. Consequently, the minimum resistivity is achieved when the presence of point defects and alumina clusters is minimized, which is consistent with high mobility [169].

This proportionality between resistivity and mobility may somewhat correspond to our curves. We will see this in Figures (IV.19 and IV.20 (a)), whereas mobility decreases, there is an increase in resistivity[186].

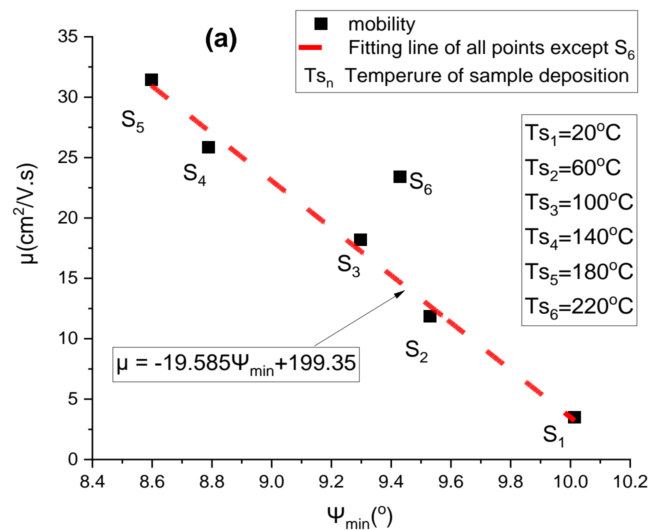

Figure IV. 19: Mobility of AZO thin films versus the minimal value of ellipsometric angle Ψ_{min}.

Figure IV.19 illustrates the comportment of mobility as a function of Ψ_{min}. First, by examining the figure, it appears that the samples are not in the same arrangement. This is because the numbering of the samples was initially based on deposition temperatures. Since each sample has a different Ψ_{min}.

For the numbering to be arranged automatically, as in the curves of the oxygen change series (like Figures. IV. (2, 3, and 4)), the increase in temperature must be consistent with the increase in Ψ_{min} values.

The polynomial equation derived from Figure IV.19 which shows the best fit of the experimental points is as follows:

$$\mu = -19.585\,\psi_{min} + 199.35 \tag{IV.15}$$

For a simplified relationship (IV.15) we did not include the point of S_6 in the fit because it is somewhat distant and does not follow a linear pattern like the rest of the points.

Validity limits of Eq. IV.15 are from 400 to 900 nm for wavelength and [3.49°;31.46°] of Ψ_{min}, with average accuracy (relative error below 8.4 %), see Table IV.6

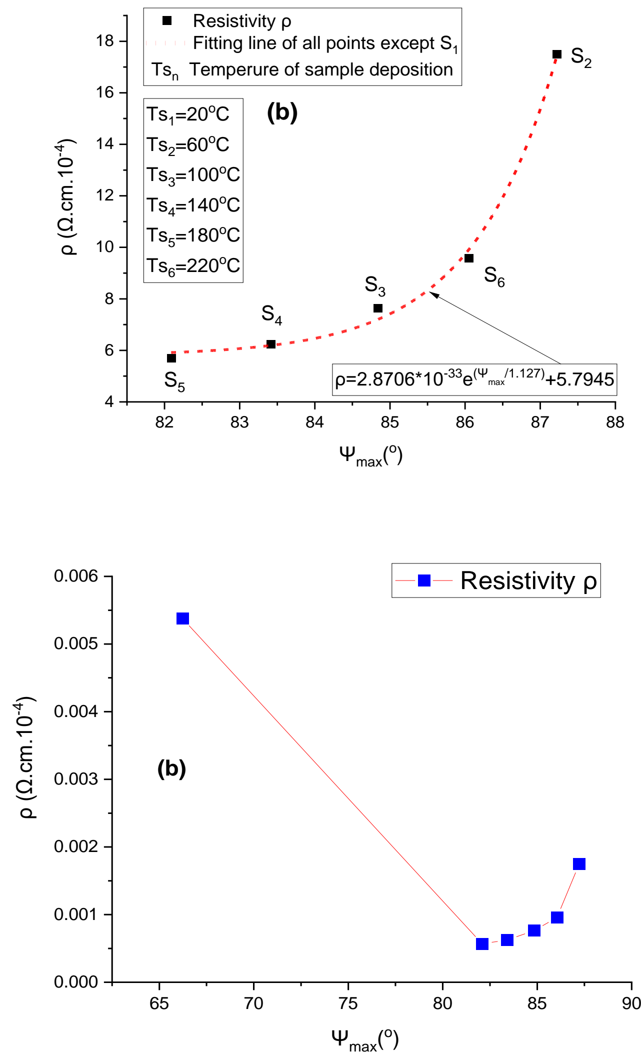

Figure IV. 20: Resistivity of AZO deposits versus Ψ_{max} angle at different deposition temperatures:(a) without S_1 sample; (b) with S_1sample.

Figure IV.20 exhibits the evolution of resistivity as function of Ψ_{max} angle at different temperatures of deposition. As we can see, the experimental point associated to S_1 is very far from the other points because its Ψ_{max} is so low (see Fig. IV.20 (b)), and it has a high resistivity compared to the rest of the films. That may be due to the presence of point defects and alumina clusters.

As before, to obtain the simplest relationship we will not include the first sample in the fit process. One comes to the following relationship:

$$\rho = 2.87 * 10^{-33} e^{(0.89\,\psi_{max})} + 5.7945 \qquad \text{(IV.16)}$$

Interval validity of Eq. IV.16 is from 400 to 900 nm for wavelength and [83.4°;87.2°] for Ψ_{max}, with average accuracy (relative error does not exceed 5.9 %), see Table IV.6

Sample	ρ resistivity measured (Ω.cm)	ρ resistivity calculated with Ψ_{max} method (Ω.cm)	Relative error (%) of ρ	μ mobility measured (cm^2/V.s)	μ mobility calculated with Ψ_{min} method (cm^2/V.s)	Relative error (%)
S1 20 °C	/	/	/	3.49	3.22	8.38
S2 60 °C	17.51	17.5	0.06	11.88	12.7	6.44
S3 100 °C	9.9	9.58	3.7	18.18	17.27	5.27
S4 **140** °C	6.19	6.25	0.89	25.87	27.21	4.92
S5 **180** °C	5.91	5.69	3.77	31.46	30.98	1.57
S6 **220** °C	7.21	7.63	5.94	/	/	/

Table IV. 6: Comparison between measured and calculated, charge carrier density and mobility, of AZO thin films deposited at different temperatures of deposition.

3.3.2 Optical property

Figure IV.21 represents the variation of bandgap energy as a function of Ψ_{min}. From that curve, we can see that the bandgap energy decreases with decreasing of Ψ_{min}. It is noteworthy that it increases with the increasing of deposition temperature, and since the charge carriers' density increases almost, which is due to the Boorstin-Moss effect. Based on this effect, the band gap decreases due to the decrease in charge carrier density (we mentioned this in the previous section with series 1).

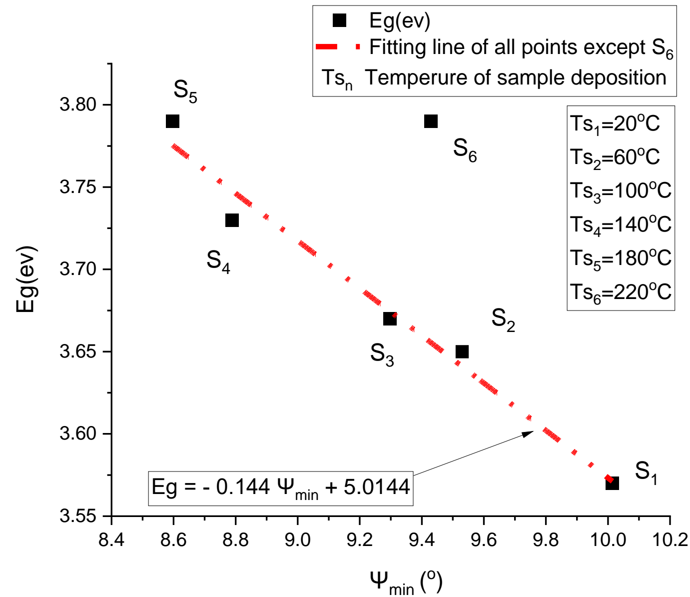

Figure IV. 21: Bandgap energy of AZO thin films deposited at different temperatures, as function of minimal values of ellipsometric angle Ψ_{min}.

The fit curve of the experimental points S_1 to S_5 is in agreement with the following relationship:

$$Eg = -0.144\,\psi_{min} + 5.0144 \tag{IV.17}$$

Interval validity of Eq. IV.17 is from 400 to 900 nm for wavelength and [3.49°; 31.46°] for Ψ_{min}, with excellent accuracy (the bigger relative error is 0.5 %), see Table IV.7. One can note that we did not include the last sample in the fitting because it appears to be more extreme than the rest.

Sample	Eg(eV) measured	Eg(eV) with Ψ_{min} method	Relative error (%)
S1$_{20}$ ^{o}C	3.57	3.572	0.06
S2$_{60}$ ^{o}C	3.65	3.64	0.21
S3$_{100}$ ^{o}C	3.67	3.675	0.15
S4$_{140}$ ^{o}C	3.73	3.74	0.5
S5$_{180}$ ^{o}C	3.79	3.77	0.35

Table IV. 7: Comparison between measured and calculated bandgap energy of AZO thin films deposited at different temperatures of deposition, in case of "Ψ_{min} method".

4 Conclusion

The primary objective of this chapter was to devise a mathematical approach for theoretically deriving the photoelectric properties of zinc oxide films. This involved integrating the well-established and fundamental spectroscopic ellipsometry equation with the renowned equations governing the optoelectrical properties of the material. However, due to the resulting equations being intricate and impractical, we opted for an experimental approach. We graphically plotted the curves of photoelectric properties in terms of ψ and Δ and subsequently extracted the experimental relationships from these curves.

Additionally, we conducted a comprehensive study of these properties as a function of:

- Oxygen concentration (at room temperature).
- Variation of deposition temperature (at a constant oxygen concentration 20%. We chose this sample for identification because it has good properties through transparency and conductivity, as shown in Table IV.8).

The obtained results are succinctly summarized in two tables (IV.8, and IV.9), aligning with existing literature.

Charge carriers density (n)						
Resistivity (ρ)						
Mobility (μ)						
Zn cluster (defect)						
Al2O3 (defect): Alumina cluster						
Bandgap energy (Eg)						
Oxygen concentration (%)	10	15	20	25	30	35
Regime of AZO Thin film	Metalic regime		Transition regime		Oxidised regime	

Table IV. 8: A table summarizing the optoelectrical properties of AZO thin films in relation to variations in oxygen concentration across three modes, along with the factors influencing these changes (The results are consistent with the literatures [169, 187–189])

Resistivity (ρ)						
Mobility (μ)						
Bandgap energy (Eg)						
Zn cluster						
Alumina cluster: Al_2O_3						
Temperature of Deposition (oC)	20	60	100	140	180	220

Table IV. 9: A table presenting a concise summary of select optoelectrical properties of AZO thin films with varying temperatures of deposition while maintaining a constant oxygen concentration, along with the influencing factors behind these changes (The results are consistent with the literatures [169, 189])

Furthermore, we fine-tuned the extracted equations within specific wavelength ranges and rigorously tested their accuracy against experimental results. The outcomes of this testing process are presented as follows:

➢ Series one: AZO with different oxygen concentration:

- Bandgap energy (Eg): The most reliable parameter, exhibiting a relative error of no more than 0.3%.
- Mobility (μ): Slightly less accurate but still good, with a maximum relative error of approximately 1.06%.
- Resistivity (ρ): The resistivity curve is divided into two parts. Overall, the equations demonstrate moderate accuracy, with a relative error below 9% for the first part and below 3% for the second part.
- Charge carrier density (n): The least accurate among the parameters but still fairly acceptable, with a relative error below 9 %.

Another derived relationship expressing the variation in oxygen concentration in AZO thin films as a function of ψ_{max} exhibits a relative error that does not exceed 5%.

- Series two: AZO with temperature deposition:

- The relative error in resistivity shows moderate accuracy, remaining under 5.9%.
- Mobility demonstrates moderate accuracy with a relative error less than 8.4%
- Bandgap energy showcases excellent accuracy, with the maximum relative error being 0.5%.

General Conclusion

General Conclusion:

The investigation focused on ZnO and AZO samples deposited through the magnetron sputtering technique, exploring variations in material composition and enabling a comprehensive examination across three principal modes (metallic, transition, and oxidized). Numerous valuable insights were drawn from this study, leading to several meaningful conclusions.

ZnO samples:

We used the sputtering technique to deposits these samples with different oxygen concentrations. The samples had remarkable optical properties in the visible and near-infrared regions, but they also had some defects that altered the optical condition like the absorption, optical resistivity, and extinction. These defects varied according to the changes in oxygen concentrations among the samples.

The excitation k and optical conductivity σ changed significantly due to the oxygen concentration. The defects were a key factor for this change.

We tested a new model (Birouk's model) based on the refraction index of the samples, by applying it to our experimental results. It emerges from this testing an outstanding fit of the results in every stage and every feature of this model.

AZO samples:

We deposited these samples with sputtering technique, by varying the oxygen concentration, and on another side, we deposited other samples, with same technique, by fixing oxygen rate, and varying the deposition temperature. We found a pure mathematical formula that connected the material optoelectrical properties and spectroscopic ellipsometry parameters, but somewhat long and complex. We used spectroscopic ellipsometry parameters (ψ, and Δ) to examine the optoelectrical results of the samples. In this case, doping enhanced the electrical properties of the material, regardless of the changes in oxygen concentration and deposition temperature. These two factors affected the samples as follows:

- The oxygen concentration growth made the samples more transparent and slightly more resistant; while it reduced the electron mobility and concentration (see Table 3);

- The resistivity of the samples decreased with the temperature, from 17.5 to 7.2 Ωcm, in some cases; meanwhile, the electron mobility increased, from 3.49 to 31.46 cm2/V s. However, the gap energy did not change much overall.

The manipulation of oxygen concentration in the sample facilitated the identification of samples with varying characteristics. Within the initial series, the most robust sample, exhibiting high-quality properties such as elevated conductivity and transparency, was the one with a 20 % oxygen concentration. This particular sample demonstrated a notable absence of defects that typically impede transparency reduction and absorption increase. Additionally, it exhibited low electrical resistivity (high conductivity), accompanied by a substantial charge density and exceptionally high electron mobility (See Table IV.8).

These distinctive features qualified this sample for further study under the influence of deposition temperature.

Altering the deposition temperature setting led to notable alterations in the properties of the sample with a 20 % oxygen concentration. Among the various temperatures tested, 180°C stood out as the optimal setting. At this specific temperature, the sample exhibited the lowest electrical resistivity (indicative of high conductivity) and the highest electron mobility observed thus far. Additionally, there was a substantial increase in the gap energy, further corroborating the notion that temperature plays a pivotal role in enhancing the optoelectrical properties of zinc oxide thin films.

Numerous experimental mathematical equations in polynomial form have been derived, offering a direct means to calculate the properties of AZO samples and streamlining the investigation process. The accuracy of many of these equations was substantiated through rigorous testing under experimental conditions.

In essence, the research has successfully accomplished its stated objectives outlined in the introduction, which were:

- Conducting a more in-depth analysis of ZnO and AZO films.
- Formulating equations to facilitate the determination of optoelectrical properties for AZO films.
- Demonstrating the viability of the new refractive index model and its compatibility with the obtained results.

This investigation holds significant implications for the scientific community as it introduces a novel perspective on examining the optoelectrical properties of films by incorporating a spectroscopic factor.

However, it is crucial to acknowledge certain limitations within this study, particularly the constraints imposed on the generalizability of results. For instance, the study is confined to specific limits within the optical and infrared domains. It is hoped that future research will expand these findings, potentially across various wave spectra, leading to the derivation of comprehensive mathematical equations.

In conclusion, this study delved into the analysis of ZnO and AZO thin films, providing a more profound understanding of the material's properties at both electrical and optical levels.

References

1. Reimann K, Steube M (1998) Experimental determination of the electronic band structure of SnO2. Solid State Commun 105:649–652. https://doi.org/10.1016/S0038-1098(97)10151-X

2. Sharmin A, Tabassum S, Bashar MS, Mahmood ZH (2019) Depositions and characterization of sol–gel processed Al-doped ZnO (AZO) as transparent conducting oxide (TCO) for solar cell application. Journal of Theoretical and Applied Physics 13:123–132. https://doi.org/10.1007/S40094-019-0329-0/FIGURES/11

3. Kemiha A, Birouk B, Raskin JP (2018) Ellipsometry-based conductivity extraction in case of phosphorus doped polysilicon. Journal of Materials Science: Materials in Electronics 29:11627–11636. https://doi.org/10.1007/S10854-018-9260-4/METRICS

4. King PDC, Veal TD (2011) Conductivity in transparent oxide semiconductors. Journal of Physics: Condensed Matter 23:334214. https://doi.org/10.1088/0953-8984/23/33/334214

5. Hogarth CA (1951) Hall Constant of Cadmium Oxide. Nature 1951 167:4248 167:521–522. https://doi.org/10.1038/167521a0

6. Afre RA, Sharma N, Sharon M, Sharon M (2018) Transparent conducting oxide films for various applications: A review. Reviews on Advanced Materials Science 53:79–89. https://doi.org/10.1515/RAMS-2018-0006/MACHINEREADABLECITATION/RIS

7. Sabeeh SH, Jassam RH (2018) The effect of annealing temperature and Al dopant on characterization of ZnO thin films prepared by sol-gel method. Results Phys 10:212–216. https://doi.org/10.1016/J.RINP.2018.05.033

8. Dixon SC, Scanlon DO, Carmalt CJ, Parkin IP (2016) n-Type doped transparent conducting binary oxides: an overview. J Mater Chem C Mater 4:6946–6961. https://doi.org/10.1039/C6TC01881E

9. Pasquarelli RM, Ginley DS, O’hayre R (2011) Solution processing of transparent conductors: from flask to film. Chem Soc Rev 40:5406–5441. https://doi.org/10.1039/C1CS15065K

10. V VT (2011) Highly conductive and transparent ZnO thin film using Chemical Spray Pyrolysis technique: Effect of doping and deposition parameters

11. Özgür Ü, Alivov YI, Liu C, et al (2005) A comprehensive review of ZnO materials and devices. J Appl Phys 98:1–103. https://doi.org/10.1063/1.1992666/151856

12. Segura A, Sans JA, Manjón FJ, et al (2003) Optical properties and electronic structure of rock-salt ZnO under pressure. Appl Phys Lett 83:278–280. https://doi.org/10.1063/1.1591995

13. Ludovica Intilla (2016) Study of ZnO Properties Applied to Thin Film Transistors. University College London

14. Schröer P, Krüger P, Pollmann J (1993) First-principles calculation of the electronic structure of the wurtzite semiconductors ZnO and ZnS. Phys Rev B 47:6971. https://doi.org/10.1103/PhysRevB.47.6971

15. Li L, Wang W, Liu H, et al (2009) First Principles Calculations of Electronic Band Structure and Optical Properties of Cr-Doped ZnO. Journal of Physical Chemistry C 113:8460–8464. https://doi.org/10.1021/JP811507R

16. Ramachandra Rao MS, Okada T (2014) ZnO Nanocrystals and Allied Materials. Springer Series in Materials Science 180:. https://doi.org/10.1007/978-81-322-1160-0/COVER

17. Janotti A, Van De Walle CG (2009) Fundamentals of zinc oxide as a semiconductor. Reports on Progress in Physics 72:126501. https://doi.org/10.1088/0034-4885/72/12/126501

18. Nagar S, Chakrabarti S Optimisation of ZnO thin films : implants, properties, and device fabrication. 83

19. Yu F, Song T, Wang B, et al (2019) The effects of intrinsic defects on the structural and optical properties of ZnO thin film prepared via a sol-gel method. Mater Res Express 6:115901. https://doi.org/10.1088/2053-1591/AB4394

20. Güell F, Martínez-Alanis PR (2019) Tailoring the Green, Yellow and Red defect emission bands in ZnO nanowires via the growth parameters. J Lumin 210:128–134. https://doi.org/10.1016/J.JLUMIN.2019.02.017

21. Janotti A, Van De Walle CG (2007) Native point defects in ZnO. Phys Rev B Condens Matter Mater Phys 76:165202. https://doi.org/10.1103/PHYSREVB.76.165202/FIGURES/13/MEDIUM

22. Mohammad A, Fallatah H, Shrotriya P, et al Morphology controlled oxide nanostructures and their effect on biosensing capabilities and photocatalytic activity

23. Jin BJ, Bae SH, Lee SY, Im S (2000) Effects of native defects on optical and electrical properties of ZnO prepared by pulsed laser deposition. Materials Science and Engineering: B 71:301–305. https://doi.org/10.1016/S0921-5107(99)00395-5

24. Van De Walle CG (2001) Defect analysis and engineering in ZnO. Physica B Condens Matter 308–310:899–903. https://doi.org/10.1016/S0921-4526(01)00830-4

25. Kayaci F, Vempati S, Donmez I, et al (2014) Role of zinc interstitials and oxygen vacancies of ZnO in photocatalysis: a bottom-up approach to control defect density. Nanoscale 6:10224–10234. https://doi.org/10.1039/C4NR01887G

26. Alaie S, Goettler DF, Su M, et al (2015) Thermal transport in phononic crystals and the observation of coherent phonon scattering at room temperature. Nature Communications 2015 6:1 6:1–8. https://doi.org/10.1038/ncomms8228

27. Bardeen J, Shockley W (1950) Scattering of Electrons in Crystals in the Presence of Large Electric Fields. Physical Review 80:69. https://doi.org/10.1103/PhysRev.80.69

28. Rode DL (1975) Chapter 1 Low-Field Electron Transport. Semiconductors and Semimetals 10:1–89. https://doi.org/10.1016/S0080-8784(08)60331-2

29. Conwell E, Weisskopf VF (1950) Theory of Impurity Scattering in Semiconductors. Physical Review 77:388. https://doi.org/10.1103/PhysRev.77.388

30. Chattopadhyay D, Queisser HJ (1981) Electron scattering by ionized impurities in semiconductors. Rev Mod Phys 53:745. https://doi.org/10.1103/RevModPhys.53.745

31. Mergel D, Qiao Z (2004) Correlation of lattice distortion with optical and electrical properties of In2O3:Sn films. J Appl Phys 95:5608–5615. https://doi.org/10.1063/1.1704852

32. Erginsoy C (1950) Neutral Impurity Scattering in Semiconductors. Physical Review 79:1013. https://doi.org/10.1103/PhysRev.79.1013

33. Aven M (Manuel), PJS (Jerome S) Physics and chemistry of II-VI compounds. (No Title)

34. Seto JYW (1975) The electrical properties of polycrystalline silicon films. J Appl Phys 46:5247–5254. https://doi.org/10.1063/1.321593

35. Sieber I, Wanderka N, Urban I, et al (1998) Electron microscopic characterization of reactively sputtered ZnO films with different Al-doping levels. Thin Solid Films 330:108–113. https://doi.org/10.1016/S0040-6090(98)00608-7

36. Hartnagel H (1995) Semiconducting Transparent Thin Films

37. Sagalowicz L, Fox GR (1999) Planar defects in ZnO thin films deposited on optical fibers and flat substrates. J Mater Res 14:1876–1885. https://doi.org/10.1557/JMR.1999.0252

38. Hafdallah A, Ynineb F, Aida MS, Attaf N (2011) In doped ZnO thin films. J Alloys Compd 509:7267–7270. https://doi.org/10.1016/J.JALLCOM.2011.04.058

39. Pathak TK, Kumar V, Swart HC, Purohit LP (2016) Effect of doping concentration on the conductivity and optical properties of p-type ZnO thin films. Physica B Condens Matter 480:31–35. https://doi.org/10.1016/J.PHYSB.2015.09.033

40. Grasza K, ŁUsakowska E, Skupiński P, et al (2007) Effect of annealing atmosphere on the quality of ZnO crystal surface. physica status solidi (b) 244:1468–1472. https://doi.org/10.1002/PSSB.200675110

41. Yu X, Ma J, Ji F, et al (2005) Influence of annealing on the properties of ZnO:Ga films prepared by radio frequency magnetron sputtering. Thin Solid Films 483:296–300. https://doi.org/10.1016/J.TSF.2005.01.013

42. Bouhssira N, Abed S, Tomasella E, et al (2006) Influence of annealing temperature on the properties of ZnO thin films deposited by thermal evaporation. Appl Surf Sci 252:5594–5597. https://doi.org/10.1016/J.APSUSC.2005.12.134

43. Jeong WJ, Park GC (2001) Electrical and optical properties of ZnO thin film as a function of deposition parameters. Solar Energy Materials and Solar Cells 65:37–45. https://doi.org/10.1016/S0927-0248(00)00075-1

44. Assunção V, Fortunato E, Marques A, et al (2003) Influence of the deposition pressure on the properties of transparent and conductive ZnO:Ga thin-film produced by r.f. sputtering at room temperature. Thin Solid Films 427:401–405. https://doi.org/10.1016/S0040-6090(02)01184-7

45. Li FM, Hsieh GW, Dalal S, et al (2008) Zinc oxide nanostructures and high electron mobility nanocomposite thin film transistors. IEEE Trans Electron Devices 55:3001–3011. https://doi.org/10.1109/TED.2008.2005180

46. Tsukazaki A, Ohtomo A, Kawasaki M (2006) High-mobility electronic transport in ZnO thin films. Appl Phys Lett 88:. https://doi.org/10.1063/1.2193727/907736

47. Bhattacharya Pallab, Fornari R (Roberto), Kamimura H (2011) Comprehensive semiconductor science and technology

48. Bouderbala M, Hamzaoui S, Amrani B, et al (2008) Thickness dependence of structural, electrical and optical behaviour of undoped ZnO thin films. Physica B Condens Matter 403:3326–3330. https://doi.org/10.1016/J.PHYSB.2008.04.045

49. Kandpal K, Singh J, Gupta N, Shekhar C (2018) Effect of thickness on the properties of ZnO thin films prepared by reactive RF sputtering. Journal of Materials Science: Materials in Electronics 29:14501–14507. https://doi.org/10.1007/S10854-018-9584-0/METRICS

50. Yen T, Haungs A, Kim SJ, et al (2010) Effect of post-deposition processing on ZnO thin films and devices. J Electron Mater 39:568–572. https://doi.org/10.1007/S11664-009-0999-5/METRICS

51. Tsakonas C, Kuznetsov VL, Cranton WM, et al (2017) Low temperature sputter-deposited ZnO films with enhanced Hall mobility using excimer laser post-processing. J Phys D Appl Phys 50:485306. https://doi.org/10.1088/1361-6463/AA9316

52. Leiter F, Alves H, Pfisterer D, et al (2003) Oxygen vacancies in ZnO. Physica B Condens Matter 340–342:201–204. https://doi.org/10.1016/J.PHYSB.2003.09.031

53. Wang NW, Yang YH, Yang GW (2009) Indium oxide-zinc oxide nanosized heterostructure and whispering gallery mode luminescence emission. Journal of Physical Chemistry C 113:15480–15483. https://doi.org/10.1021/JP906924W/ASSET/IMAGES/MEDIUM/JP-2009-06924W_0005.GIF

54. Lin B, Fu Z, Jia Y (2001) Green luminescent center in undoped zinc oxide films deposited on silicon substrates. Appl Phys Lett 79:943–945. https://doi.org/10.1063/1.1394173

55. Djurišić AB, Leung YH (2006) Optical Properties of ZnO Nanostructures. Small 2:944–961. https://doi.org/10.1002/SMLL.200600134

56. Yen WM (William M), Shionoya S, Yamamoto H (2007) Phosphor handbook. 1051

57. Vanheusden K, Seager CH, Warren WL, et al (1996) Correlation between photoluminescence and oxygen vacancies in ZnO phosphors. Appl Phys Lett 68:403–405. https://doi.org/10.1063/1.116699

58. Zhang SB, Wei SH, Zunger A (2001) Intrinsic *n*-type versus *p*-type doping asymmetry and the defect physics of ZnO. Phys Rev B 63:075205. https://doi.org/10.1103/PhysRevB.63.075205

59. Studenikin SA, Golego N, Cocivera M (1998) Fabrication of green and orange photoluminescent, undoped ZnO films using spray pyrolysis. J Appl Phys 84:2287–2294. https://doi.org/10.1063/1.368295

60. Sekiguchi T, Ohashi N, Terada Y (1997) Effect of hydrogenation on ZnO luminescence. Japanese Journal of Applied Physics, Part 2: Letters 36:L289. https://doi.org/10.1143/JJAP.36.L289/XML

61. Lavrov E V., Weber J, Börrnert F, et al (2002) Hydrogen-related defects in ZnO studied by infrared absorption spectroscopy. Phys Rev B 66:165205. https://doi.org/10.1103/PhysRevB.66.165205

62. Tam KH, Ng AMC, Leung YH, et al (2006) ZnO nanorods by hydrothermal method for ZnO/GaN LEDs. Conference on Optoelectronic and Microelectronic Materials and Devices, Proceedings, COMMAD 109–112. https://doi.org/10.1109/COMMAD.2006.4429892

63. Wang ZG, Zu XT, Zhu S, Wang LM (2006) Green luminescence originates from surface defects in ZnO nanoparticles. Physica E Low Dimens Syst Nanostruct 35:199–202. https://doi.org/10.1016/J.PHYSE.2006.07.022

64. Alvi NH, ul Hasan K, Nur O, Willander M (2011) The origin of the red emission in n-zno nanotubes/p-gan white light emitting diodes. Nanoscale Res Lett 6:1–7. https://doi.org/10.1186/1556-276X-6-130/FIGURES/4

65. Nambiar B, Sadiku Emmanuel R, Babu Perumal A, et al (2023) Various Applications of ZnO Thin Films Obtained by Chemical Routes in the Last Decade. Molecules 2023, Vol 28, Page 4674 28:4674. https://doi.org/10.3390/MOLECULES28124674

66. Wibowo A, Marsudi MA, Amal MI, et al (2020) ZnO nanostructured materials for emerging solar cell applications. RSC Adv 10:42838–42859. https://doi.org/10.1039/D0RA07689A

67. Rai N, Rai S, Singh PK, et al (2020) Analysis of various ETL materials for an efficient perovskite solar cell by numerical simulation. Journal of Materials Science: Materials in Electronics 31:16269–16280. https://doi.org/10.1007/S10854-020-04175-Z/METRICS

68. Platzer-Björkman C, Barreau N, Bär M, et al (2019) Back and front contacts in kesterite solar cells: state-of-the-art and open questions. Journal of Physics: Energy 1:044005. https://doi.org/10.1088/2515-7655/AB3708

69. Otalora C, Botero MA, Ordoñez G (2021) ZnO compact layers used in third-generation photovoltaic devices: a review. Journal of Materials Science 2021 56:28 56:15538–15571. https://doi.org/10.1007/S10853-021-06275-5

70. Drapak IT (1968) Visible luminescence of a ZnO-Cu2O heterojunction.. Soviet Physics Semiconductors-USSR 24 (1968): 513

71. Macaluso R, Lullo G, Crupi I, et al (2020) Progress in Violet Light-Emitting Diodes Based on ZnO/GaN Heterojunction. Electronics 2020, Vol 9, Page 991 9:991. https://doi.org/10.3390/ELECTRONICS9060991

72. Huang Y, Zhou X, Zhang L, et al (2020) Tunable electroluminescence from an n-ZnO/p-GaN heterojunction with a CsPbBr3 interlayer grown by pulsed laser deposition. J Mater Chem C Mater 8:12240–12246. https://doi.org/10.1039/D0TC02807J

73. Shafiqul IM, Deep R, Lin J, et al (2022) Demonstration and Evaluation of p-Type and n-Type ZnO Nanoparticles-Based Homojunction UV Light-Emitting Diodes. physica status solidi (RRL) – Rapid Research Letters 16:2100556. https://doi.org/10.1002/PSSR.202100556

74. He G, Jiang M, Li B, et al (2017) Sb-Doped ZnO microwires: emitting filament and homojunction light-emitting diodes. J Mater Chem C Mater 5:10938–10946. https://doi.org/10.1039/C7TC03956E

75. Park J, Kim C, Kim S, et al (2008) Source/drain series-resistance effects in amorphous gallium-indium zinc-oxide thin film transistors. IEEE Electron Device Letters 29:879–881. https://doi.org/10.1109/LED.2008.2000815

76. Kandpal K, Gupta N (2018) Perspective of zinc oxide based thin film transistors: A comprehensive review. Microelectronics International 35:52–63. https://doi.org/10.1108/MI-10-2016-0066/FULL/XML

77. Fortunato E, Barquinha P, Martins R (2012) Oxide Semiconductor Thin-Film Transistors: A Review of Recent Advances. Advanced Materials 24:2945–2986. https://doi.org/10.1002/ADMA.201103228

78. Wang W, Li K, Lan J, et al (2023) CMOS backend-of-line compatible memory array and logic circuitries enabled by high performance atomic layer deposited ZnO thin-film transistor. Nature Communications 2023 14:1 14:1–11. https://doi.org/10.1038/s41467-023-41868-5

79. Ngwashi DK, Mih TA (2023) The impact of multi-layered dielectrics on the electrical performance of ZnO thin-film transistors. Sci Afr 20:e01653. https://doi.org/10.1016/J.SCIAF.2023.E01653

80. Kim T, Kim Y, Ahn J, Kim EK (2023) Enhancement of InGaZnO Thin-Film Transistors by Contact Barrier Modulation Using Oxygen Defects. ACS Appl Electron Mater 5:3772–3779. https://doi.org/10.1021/ACSAELM.3C00508/SUPPL_FILE/EL3C00508_SI_001.PDF

81. Liu Y, Yu Y, Li T, et al (2023) High Performance and High Yield Solution Processed IGZO Thin Film Transistors Fabricated with Low-Temperature Annealed Hafnium Dioxide Gate Dielectric. Adv Electron Mater 9:2300415. https://doi.org/10.1002/AELM.202300415

82. Wang D, Jiang Z, Li L, et al (2023) High-Performance Thin-Film Transistors with ZnO:H/ZnO Double Active Layers Fabricated at Room Temperature. Nanomaterials 2023, Vol 13, Page 1422 13:1422. https://doi.org/10.3390/NANO13081422

83. Cao J, Liu D, Xia W, et al (2023) Achieving High-Performance Solution-Processed Thin-Film Transistors by Doping Strong Reducibility Element Into Indium-Zinc-Oxide. IEEE Journal of the Electron Devices Society 11:406–410. https://doi.org/10.1109/JEDS.2023.3288395

84. Zhang Y-H, 张永晖, Mei Z-X, et al (2017) Review of flexible and transparent thin-film transistors based on zinc oxide and related materials*. Chinese Physics B 26:047307. https://doi.org/10.1088/1674-1056/26/4/047307

85. Kang Y, Yu F, Zhang L, et al (2021) Review of ZnO-based nanomaterials in gas sensors. Solid State Ion 360:115544. https://doi.org/10.1016/J.SSI.2020.115544

86. Nakate UT, Ahmad R, Patil P, et al (2020) Ultra thin NiO nanosheets for high performance hydrogen gas sensor device. Appl Surf Sci 506:144971. https://doi.org/10.1016/J.APSUSC.2019.144971

87. Drmosh QA, Olanrewaju Alade I, Qamar M, Akbar S (2021) Zinc Oxide-Based Acetone Gas Sensors for Breath Analysis: A Review. Chem Asian J 16:1519–1538. https://doi.org/10.1002/ASIA.202100303

88. Wang CN, Li YL, Gong FL, et al (2020) Advances in Doped ZnO Nanostructures for Gas Sensor. The Chemical Record 20:1553–1567. https://doi.org/10.1002/TCR.202000088

89. Raza W, Ahmad K (2018) A highly selective Fe@ZnO modified disposable screen printed electrode based non-enzymatic glucose sensor (SPE/Fe@ZnO). Mater Lett 212:231–234. https://doi.org/10.1016/J.MATLET.2017.10.100

90. Chen CY, Liu YR, Lin SS, et al (2016) Role of annealing temperature on the formation of aligned zinc oxide nanorod arrays for efficient photocatalysts and photodetectors. Sci Adv Mater 8:2197–2203. https://doi.org/10.1166/SAM.2016.3005

91. Spencer MJS (2012) Gas sensing applications of 1D-nanostructured zinc oxide: Insights from density functional theory calculations. Prog Mater Sci 57:437–486. https://doi.org/10.1016/J.PMATSCI.2011.06.001

92. Yu A, Jiang P, Lin Wang Z (2012) Nanogenerator as self-powered vibration sensor. Nano Energy 1:418–423. https://doi.org/10.1016/J.NANOEN.2011.12.006

93. Ameen S, Shaheer Akhtar M, Shin HS (2012) Highly sensitive hydrazine chemical sensor fabricated by modified electrode of vertically aligned zinc oxide nanorods. Talanta 100:377–383. https://doi.org/10.1016/J.TALANTA.2012.08.001

94. Ibrahim AA, Dar GN, Zaidi SA, et al (2012) Growth and properties of Ag-doped ZnO nanoflowers for highly sensitive phenyl hydrazine chemical sensor application. Talanta 93:257–263. https://doi.org/10.1016/J.TALANTA.2012.02.030

95. Umar A, Akhtar MS, Al-Hajry A, et al (2015) Enhanced photocatalytic degradation of harmful dye and phenyl hydrazine chemical sensing using ZnO nanourchins. Chemical Engineering Journal 262:588–596. https://doi.org/10.1016/J.CEJ.2014.09.111

96. Ahmad R, Tripathy N, Ahn MS, Hahn YB (2017) Development of highly-stable binder-free chemical sensor electrodes for p-nitroaniline detection. J Colloid Interface Sci 494:300–306. https://doi.org/10.1016/J.JCIS.2017.01.099

97. Cheng XL, Zhao H, Huo LH, et al (2004) ZnO nanoparticulate thin film: preparation, characterization and gas-sensing property. Sens Actuators B Chem 102:248–252. https://doi.org/10.1016/J.SNB.2004.04.080

98. Smith CS (1954) Piezoresistance Effect in Germanium and Silicon. Physical Review 94:42. https://doi.org/10.1103/PhysRev.94.42

99. Gong T, Zhang H, Huang W, et al (2018) Highly responsive flexible strain sensor using polystyrene nanoparticle doped reduced graphene oxide for human health monitoring. Carbon N Y 140:286–295. https://doi.org/10.1016/J.CARBON.2018.09.007

100. Kumari P, Mathew L, Syal P (2017) Increasing trend of wearables and multimodal interface for human activity monitoring: A review. Biosens Bioelectron 90:298–307. https://doi.org/10.1016/J.BIOS.2016.12.001

101. Cai G, Yang M, Xu Z, et al (2017) Flexible and wearable strain sensing fabrics. Chemical Engineering Journal 325:396–403. https://doi.org/10.1016/J.CEJ.2017.05.091

102. Vatani M, Lu Y, Engeberg ED, Choi JW (2015) Combined 3D printing technologies and material for fabrication of tactile sensors. International Journal of Precision Engineering and Manufacturing 16:1375–1383. https://doi.org/10.1007/S12541-015-0181-3/METRICS

103. Zang Y, Zhang F, Di CA, Zhu D (2015) Advances of flexible pressure sensors toward artificial intelligence and health care applications. Mater Horiz 2:140–156. https://doi.org/10.1039/C4MH00147H

104. Xu F, Li X, Shi Y, et al (2018) Recent Developments for Flexible Pressure Sensors: A Review. Micromachines 2018, Vol 9, Page 580 9:580. https://doi.org/10.3390/MI9110580

105. Samoei VK, Jayatissa AH (2020) Aluminum doped zinc oxide (AZO)-based pressure sensor. Sens Actuators A Phys 303:111816. https://doi.org/10.1016/J.SNA.2019.111816

106. Rodwihok C, Choopun S, Ruankham P, et al (2019) UV sensing properties of ZnO nanowires/nanorods. Appl Surf Sci 477:159–165. https://doi.org/10.1016/J.APSUSC.2017.11.056

107. Rodwihok C, Choopun S, Ruankham P, et al (2019) UV sensing properties of ZnO nanowires/nanorods. Appl Surf Sci 477:159–165. https://doi.org/10.1016/J.APSUSC.2017.11.056

108. Xu QA, Zhang JW, Ju KR, et al (2006) ZnO thin film photoconductive ultraviolet detector with fast photoresponse. J Cryst Growth 289:44–47. https://doi.org/10.1016/J.JCRYSGRO.2005.11.008

109. Humayun Q, Kashif M, Hashim U, Qurashi A (2014) Selective growth of ZnO nanorods on microgap electrodes and their applications in UV sensors. Nanoscale Res Lett 9:1–5. https://doi.org/10.1186/1556-276X-9-29/FIGURES/6

110. Kwon K, Shim J, Lee JO, et al (2015) Localized Laser-Based Photohydrothermal Synthesis of Functionalized Metal-Oxides. Adv Funct Mater 25:2222–2229. https://doi.org/10.1002/ADFM.201404215

111. Qin L, Mawignon FJ, Hussain M, et al (2021) Economic Friendly ZnO-Based UV Sensors Using Hydrothermal Growth: A Review. Materials 2021, Vol 14, Page 4083 14:4083. https://doi.org/10.3390/MA14154083

112. Kern W, Schuegraf KK (2001) Deposition Technologies and Applications: Introduction and Overview. Handbook of Thin Film Deposition Processes and Techniques 11–43. https://doi.org/10.1016/B978-081551442-8.50006-7

113. Waser R, Schneller T, Hoffmann-eifert S, Ehrhart P (2001) Advanced chemical deposition techniques - from research to production. Integrated Ferroelectrics 36:3–20. https://doi.org/10.1080/10584580108015524

114. Creighton JR, Ho P (2001) Introduction to Chemical Vapor Deposition (CVD)

115. Spear KE (1982) Principles and applications of chemical vapor deposition (CVD). Pure and Applied Chemistry 54:1297–1311. https://doi.org/10.1351/PAC198254071297/MACHINEREADABLECITATION/RIS

116. Purica M, Budianu E, Rusu E, et al (2002) Optical and structural investigation of ZnO thin films prepared by chemical vapor deposition (CVD). Thin Solid Films 403–404:485–488. https://doi.org/10.1016/S0040-6090(01)01544-9

117. Ritala M, Leskelä M (2002) Atomic layer deposition. Handbook of Thin Films 103–159. https://doi.org/10.1016/B978-012512908-4/50005-9

118. Gao Z, Banerjee P (2019) Review Article: Atomic layer deposition of doped ZnO films. Journal of Vacuum Science & Technology A: Vacuum, Surfaces, and Films 37:50802. https://doi.org/10.1116/1.5112777/13960621/050802_1_ACCEPTED_MANUSCRIPT.PDF

119. Shinde VR, Lokhande CD, Mane RS, Han SH (2005) Hydrophobic and textured ZnO films deposited by chemical bath deposition: annealing effect. Appl Surf Sci 245:407–413. https://doi.org/10.1016/J.APSUSC.2004.10.036

120. Kim HW, Kim HE, Kim HW, Knowles JC (2005) Improvement of Hydroxyapatite Sol–Gel Coating on Titanium with Ammonium Hydroxide Addition. Journal of the American Ceramic Society 88:154–159. https://doi.org/10.1111/J.1551-2916.2004.00030.X

121. Wu C, Ramaswamy Y, Gale D, et al (2008) Novel sphene coatings on Ti–6Al–4V for orthopedic implants using sol–gel method. Acta Biomater 4:569–576. https://doi.org/10.1016/J.ACTBIO.2007.11.005

122. Kern W, Vossen JL (2012) Thin Film Processes II. Thin Film Processes II 1–866. https://doi.org/10.1016/C2009-0-22311-7

123. Znaidi L (2010) Sol–gel-deposited ZnO thin films: A review. Materials Science and Engineering: B 174:18–30. https://doi.org/10.1016/J.MSEB.2010.07.001

124. Adnan M, Irshad Z, Lee JK (2020) Facile all-dip-coating deposition of highly efficient (CH 3) 3 NPbI 3−x Cl x perovskite materials from aqueous non-halide lead precursor. RSC Adv 10:29010–29017. https://doi.org/10.1039/D0RA06074G

125. Wang Z, Zhang Z (2016) Electron Beam Evaporation Deposition. Advanced Nano Deposition Methods 33–58. https://doi.org/10.1002/9783527696406.CH2

126. Ali HM, Abd El-Raheem MM, Megahed NM, Mohamed HA (2006) Optimization of the optical and electrical properties of electron beam evaporated aluminum-doped zinc oxide films for opto-electronic applications. Journal of Physics and Chemistry of Solids 67:1823–1829. https://doi.org/10.1016/J.JPCS.2006.04.005

127. Electron Beam Evaporation - Polyteknik AS. https://www.polyteknik.com/technology/electron-beam-evaporation/. Accessed 25 Jan 2024

128. le Febvrier A, Landälv L, Liersch T, et al (2021) An upgraded ultra-high vacuum magnetron-sputtering system for high-versatility and software-controlled deposition. Vacuum 187:110137. https://doi.org/10.1016/J.VACUUM.2021.110137

129. Christie DJ (2005) Target material pathways model for high power pulsed magnetron sputtering. Journal of Vacuum Science & Technology A 23:330–335. https://doi.org/10.1116/1.1865133

130. Kukla R (1997) Magnetron sputtering on large scale substrates: an overview on the state of the art. Surf Coat Technol 93:1–6. https://doi.org/10.1016/S0257-8972(97)00018-2

131. Han JG (2009) Recent progress in thin film processing by magnetron sputtering with plasma diagnostics. J Phys D Appl Phys 42:043001. https://doi.org/10.1088/0022-3727/42/4/043001

132. Gonçalves C, Charvet S, Zeinert A, et al (2002) Nanocrystalline silicon thin films prepared by radiofrequency magnetron sputtering. Thin Solid Films 403–404:91–96. https://doi.org/10.1016/S0040-6090(01)01553-X

133. Gao W, Li Z (2004) ZnO thin films produced by magnetron sputtering. Ceram Int 30:1155–1159. https://doi.org/10.1016/J.CERAMINT.2003.12.197

134. Hwang DH, Ahn JH, Hui KN, et al (2012) Structural and optical properties of ZnS thin films deposited by RF magnetron sputtering. Nanoscale Res Lett 7:1–7. https://doi.org/10.1186/1556-276X-7-26/FIGURES/5

135. Haider AJ, Jabbar AA, Ali GA (2021) A review of Pure and Doped ZnO Nanostructure Production and its Optical Properties Using Pulsed Laser Deposition Technique. J Phys Conf Ser 1795:012015. https://doi.org/10.1088/1742-6596/1795/1/012015

136. Craciun V, Elders J, Gardeniers JGE, Boyd IW (1994) Characteristics of high quality ZnO thin films deposited by pulsed laser deposition. Appl Phys Lett 65:2963–2965. https://doi.org/10.1063/1.112478

137. Drude P The theory of optics. 1902

138. Fujiwara H, Collins RW (2018) Springer Series in Optical Sciences 212 Spectroscopic Ellipsometry for Photovoltaics Volume 1: Fundamental Principles and Solar Cell Characterization

139. Fujiwara H (2007) Spectroscopic Ellipsometry: Principles and Applications. Spectroscopic Ellipsometry: Principles and Applications 1–369. https://doi.org/10.1002/9780470060193

140. Soult MC, Siller V, Zhu X, et al (2022) Spectroscopic Ellipsometry for Operando Monitoring of (De)Lithiation-Induced Phenomena on LiMn2O4 and LiNi0.5Mn1.5O4 Electrodes. J Electrochem Soc 169:040501. https://doi.org/10.1149/1945-7111/AC5CEB

141. Fouad SS, Amin GAM, El-Bana MS (2018) Physical and optical characterizations of Ge10Se90 − xTex thin films in view of their spectroscopic ellipsometry data. J Non Cryst Solids 481:314–320. https://doi.org/10.1016/J.JNONCRYSOL.2017.11.006

142. Benhaliliba M (2021) ZnO a multifunctional material: Physical properties, spectroscopic ellipsometry and surface examination. Optik (Stuttg) 241:167197. https://doi.org/10.1016/J.IJLEO.2021.167197

143. Kaspar TC, Reiser JT, Ryan J V., Wall NA (2018) Non-destructive characterization of corroded glass surfaces by spectroscopic ellipsometry. J Non Cryst Solids 481:260–266. https://doi.org/10.1016/J.JNONCRYSOL.2017.10.054

144. Home - J.A. Woollam. https://www.jawoollam.com/. Accessed 27 Jan 2024

145. Pascu R, Dinescu M (2012) SPECTROSCOPIC ELLIPSOMETRY *. Rom Rep Phys 64:135–142

146. Mackay TG, Lakhtakia A (2020) The Transfer-Matrix Method in Electromagnetics and Optics. https://doi.org/10.1007/978-3-031-02022-3

147. Hassanien AS, Akl AA (2016) Effect of Se addition on optical and electrical properties of chalcogenide CdSSe thin films. Superlattices Microstruct 89:153–169. https://doi.org/10.1016/J.SPMI.2015.10.044

148. Chabou N, Birouk B, Aida M, Raskin J (2019) Deposition time and annealing effects on morphological and optical properties of ZnS thin films prepared by chemical bath deposition. Materials Science-Poland 37:404–416. https://doi.org/10.2478/msp-2019-0043

149. Klein J, Kampermann L, Mockenhaupt B, et al (2023) Limitations of the Tauc Plot Method. Adv Funct Mater 33:2304523. https://doi.org/10.1002/ADFM.202304523

150. Viezbicke BD, Patel S, Davis BE, Birnie DP (2015) Evaluation of the Tauc method for optical absorption edge determination: ZnO thin films as a model system. physica status solidi (b) 252:1700–1710. https://doi.org/10.1002/PSSB.201552007

151. Rambadey O V., Kumar A, Sati A, Sagdeo PR (2021) Exploring the Interrelation between Urbach Energy and Dielectric Constant in Hf-Substituted BaTiO3. ACS Omega 6:32231–32238. https://doi.org/10.1021/ACSOMEGA.1C05057/ASSET/IMAGES/LARGE/AO1C05057_0007.JPEG

152. Voronin AA, Zheltikov AM (2017) The generalized Sellmeier equation for air. Scientific Reports 2017 7:1 7:1–11. https://doi.org/10.1038/srep46111

153. Birouk B, Madi D (2011) Thermal oxidation effect on structural and optical properties of heavily doped phosphorus polycrystalline silicon films. Appl Phys A Mater Sci Process 104:739–748. https://doi.org/10.1007/S00339-011-6332-1/METRICS

154. What is hall effect in physics: Definition, Types and Importance of hall effect | AESL. https://www.aakash.ac.in/important-concepts/physics/hall-effect. Accessed 27 Jan 2024

155. (13) Vac Coat | LinkedIn. https://www.linkedin.com/in/vac-coat-4504b2187/. Accessed 27 Jan 2024

156. Rossnagel SM (1999) Sputter deposition for semiconductor manufacturing. IBM J Res Dev 43:163–179. https://doi.org/10.1147/RD.431.0163

157. Simon AH (2018) Sputter Processing. Handbook of Thin Film Deposition: Fourth Edition 195–230. https://doi.org/10.1016/B978-0-12-812311-9.00007-4

158. Tuyaerts R Internal stress and opto-electronic properties of pure and Al-doped ZnO thin films deposited by reactive sputtering. dial.uclouvain.be

159. Tuyaerts R, Raskin JP, Proost J (2020) Opto-electrical properties and internal stress in Al:ZnO thin films deposited by direct current reactive sputtering. Thin Solid Films 695:137760. https://doi.org/10.1016/J.TSF.2019.137760

160. Mackay TG, Lakhtakia A (2020) The Transfer-Matrix Method in Electromagnetics and Optics. https://doi.org/10.1007/978-3-031-02022-3

161. Melsheimer J, Ziegler D (1985) Band gap energy and Urbach tail studies of amorphous, partially crystalline and polycrystalline tin dioxide. Thin Solid Films 129:35–47. https://doi.org/10.1016/0040-6090(85)90092-6

162. Young EWA, Gerretsen JH, De Wit JHW, et al (2021) Annealing Effect on Structural and Optical Properties of Cr2O3 Thin Films Prepared by R.F Magnetron Sputtering. IOP Conf Ser Mater Sci Eng 1105:012064. https://doi.org/10.1088/1757-899X/1105/1/012064

163. Mott.N F. EAD (2012) Electronic process in non-crystalline materials. 605

164. Abdallah B, Jazmati AK, Refaai R (2017) Oxygen Effect on Structural and Optical Properties of ZnO Thin Films Deposited by RF Magnetron Sputtering. Materials Research 20:607–612. https://doi.org/10.1590/1980-5373-MR-2016-0478

165. Liu Y, Lian J (2007) Optical and electrical properties of aluminum-doped ZnO thin films grown by pulsed laser deposition. Appl Surf Sci 253:3727–3730. https://doi.org/10.1016/J.APSUSC.2006.08.012

166. Dib T, Birouk B (2023) Optoelectrical properties extraction using spectroscopic ellipsometry, in case of AZO thin films deposited by DC reactive sputtering in various oxygen concentration. Journal of Materials Science: Materials in Electronics 34:1–10. https://doi.org/10.1007/S10854-023-10717-Y/METRICS

167. H. G. Tompkins and J. N. Hilfiker (2016) Spectroscopic ellipsometry

168. Tripathy SK (2015) Refractive indices of semiconductors from energy gaps. Opt Mater (Amst) 46:240–246. https://doi.org/10.1016/j.optmat.2015.04.026

169. Tuyaerts R, Raskin JP, Proost J (2020) Opto-electrical properties and internal stress in Al:ZnO thin films deposited by direct current reactive sputtering. Thin Solid Films 695:137760. https://doi.org/10.1016/J.TSF.2019.137760

170. Kim DS, Park JH, Lee SJ, et al (2013) Effects of oxygen concentration on the properties of Al-doped ZnO transparent conductive films deposited by pulsed DC magnetron sputtering. Mater Sci Semicond Process 16:997–1001. https://doi.org/10.1016/j.mssp.2013.02.012

171. Castro M V., Cerqueira MF, Rebouta L, et al (2014) Influence of hydrogen plasma thermal treatment on the properties of ZnO:Al thin films prepared by dc magnetron sputtering. Vacuum 107:145–154. https://doi.org/10.1016/j.vacuum.2014.04.022

172. Gabás M, Landa-Cánovas A, Luis Costa-Krämer J, et al (2013) Differences in n-type doping efficiency between Al- and Ga-ZnO films. J Appl Phys 113:. https://doi.org/10.1063/1.4803063/380468

173. Shah A, Ahmad M, Rahmanuddin, et al (2019) The role of Al doping on ZnO nanowire evolution and optical band gap tuning. Appl Phys A Mater Sci Process 125:1–8. https://doi.org/10.1007/S00339-019-3005-Y/METRICS

174. Uprety P, Junda MM, Ghimire K, et al (2017) Spectroscopic ellipsometry determination of optical and electrical properties of aluminum doped zinc oxide. Appl Surf Sci 421:852–858. https://doi.org/10.1016/J.APSUSC.2017.01.139

175. Pat S, Mohammadigharehbagh R, Özen S, et al (2017) The Al doping effect on the surface, optical, electrical and nanomechanical properties of the ZnO and AZO thin films prepared by RF sputtering technique. Vacuum 141:210–215. https://doi.org/10.1016/J.VACUUM.2017.04.025

176. Hassanien AS, Akl AA (2016) Effect of Se addition on optical and electrical properties of chalcogenide CdSSe thin films. Superlattices Microstruct 89:153–169. https://doi.org/10.1016/j.spmi.2015.10.044

177. Moss TS (1954) The interpretation of the properties of indium antimonide. Proceedings of the Physical Society Section B 67:775–782. https://doi.org/10.1088/0370-1301/67/10/306

178. Burstein E (1954) Anomalous optical absorption limit in InSb [4]. Physical Review 93:632–633

179. Wang F, Wu MZ, Wang YY, et al (2013) Influence of thickness and annealing temperature on the electrical, optical and structural properties of AZO thin films. Vacuum 89:127–131. https://doi.org/10.1016/J.VACUUM.2012.02.040

180. Mickan M, Helmersson U, Horwat D (2018) Effect of substrate temperature on the deposition of Al-doped ZnO thin films using high power impulse magnetron sputtering. Surf Coat Technol 347:245–251. https://doi.org/10.1016/J.SURFCOAT.2018.04.089

181. Misra P, Ganeshan V, Agrawal N (2017) Low temperature deposition of highly transparent and conducting Al-doped ZnO films by RF magnetron sputtering. J Alloys Compd 725:60–68. https://doi.org/10.1016/J.JALLCOM.2017.07.121

182. Kang SJ, Joung YH (2007) Influence of substrate temperature on the optical and piezoelectric properties of ZnO thin films deposited by rf magnetron sputtering. Appl Surf Sci 253:7330–7335. https://doi.org/10.1016/J.APSUSC.2007.03.020

183. Zhang Z, Bao C, Yao W, et al (2011) Influence of deposition temperature on the crystallinity of Al-doped ZnO thin films at glass substrates prepared by RF magnetron sputtering method. Superlattices Microstruct 49:644–653. https://doi.org/10.1016/J.SPMI.2011.04.002

184. Chaabouni F, Abaab M, Rezig B (2004) Effect of the substrate temperature on the properties of ZnO films grown by RF magnetron sputtering. Materials Science and Engineering: B 109:236–240. https://doi.org/10.1016/J.MSEB.2003.10.105

185. Li XY, Li HJ, Wang ZJ, et al (2009) Effect of substrate temperature on the structural and optical properties of ZnO and Al-doped ZnO thin films prepared by dc magnetron sputtering. Opt Commun 282:247–252. https://doi.org/10.1016/J.OPTCOM.2008.10.003

186. Li W, Sun Y, Wang Y, et al (2007) Effects of substrate temperature on the properties of facing-target sputtered Al-doped ZnO films. Solar Energy Materials and Solar Cells 91:659–663. https://doi.org/10.1016/J.SOLMAT.2006.11.018

187. Kim DS, Park JH, Lee SJ, et al (2013) Effects of oxygen concentration on the properties of Al-doped ZnO transparent conductive films deposited by pulsed DC magnetron sputtering. Mater Sci Semicond Process 16:997–1001. https://doi.org/10.1016/J.MSSP.2013.02.012

188. Zubkins M, Arslan H, Bikse L, Purans J (2019) High power impulse magnetron sputtering of Zn/Al target in an Ar and Ar/O2 atmosphere: The study of sputtering process and AZO films. Surf Coat Technol 369:156–164. https://doi.org/10.1016/J.SURFCOAT.2019.04.044

189. Kong H, Yang P, Chu J (2011) Processing Parameters and Property of AZO Thin Film Prepared by Magnetron Sputtering. J Phys Conf Ser 276:012170. https://doi.org/10.1088/1742-6596/276/1/012170

الملخص: الهدف الأساسي من هذا البحث هو إجراء تحليل مفصل لعينات أكسيد الزنك النقي وأكسيد الزنك المشوب بالألمنيوم، المترسبتين باستخدام تقنية الرش المغناطيسي. وينصب التركيز أيضا على ايجاد طريقة بديلة لاستخراج الخصائص الإلكتروضوئية لهذه العينات. تتضمن الدراسة التغيير في تركيبة أكسيد الزنك عن طريق ضبط تركيز الأكسجين، مما يؤدي إلى الحصول على عينات ذات خصائص مختلفة. بالاستعانة بجهاز القياس الطيفي الضوئي يتم دراسة الخصائص الإلكتروضوئية مثل تركيز الشحنة، وحركة حامل الشحنة، والمقاومة الضوئية، والمقاومة الكهربائية، والامتصاص الضوئي، وطاقة الفجوة.

بالإضافة إلى ذلك، يتم تطبيق نموذج معامل الانكسار الجديد "نموذج بيروك" لاختبار توافق وكفاءة العينات معه. وبعد ذلك، تتضمن عملية التحسين انشاء عينات مشابهة لتلك التي تظهر خصائص مفضلة من سلسلة أكسيد الزنك المشوب بالالمنيوم. يتم إجراء مزيد من التحقيق في هذه السلسلة المختارة عن طريق تغيير عامل درجة حرارة الترسيب. بالاستعانة بجهاز القياس الإهليلجي الطيفي يتم دراسة هذه العينات للحصول على فهم شامل لخصائصها. يتضمن فحص العينات تقييم نقاط قوتها للتطبيقات المحتملة في مختلف المجالات الصناعية.

لتعزيز الفائدة العملية للدراسة، يتم اشتقاق العلاقات الرياضية التجريبية لتبسيط عملية استخراج الخصائص الإلكترونية البصرية والتحقق من دقتها. يهدف هذا البحث إلى المساهمة برؤى قيمة للتطبيقات الصناعية وتوفير أساس للدراسات المستقبلية في هذا المجال.

Abstract: The primary objective of this research is to conduct a detailed analysis of samples of pure zinc oxide and aluminum-doped zinc oxide, deposited using the magnetron sputtering technique. The focus is on identifying an alternative method for efficiently extracting the optoelectronic properties of these samples. The study involves varying the composition of zinc oxide by adjusting the oxygen concentration, resulting in samples with distinct properties. Spectroscopic ellipsometry is employed to investigate optoelectronic properties such as charge concentration, charge carrier mobility, photoresistance, electrical resistance, absorption, and gap energy.

Additionally, a novel refractive index model, Birouk's model, is applied to test the compatibility and efficiency of the samples. Subsequently, a refinement process involves sorting samples that exhibit favorable characteristics from a previous series. These selected samples are further investigated by varying the deposition temperature factor. using spectroscopic ellipsometry to gain a comprehensive understanding of their properties. The examination of the samples includes assessing their strengths for potential applications across various industrial fields.

To enhance the practical utility of the study, experimental mathematical relationships are derived to streamline the extraction of optoelectronic properties and validate their accuracy. This research aims to contribute valuable insights for industrial applications and provide a foundation for future studies in the field.

Résumé: L'objectif principal de cette recherche est de mener une analyse détaillée d'échantillons d'oxyde de zinc pur et d'oxyde de zinc dopé à l'aluminium, déposés à l'aide de la technique de pulvérisation magnétron. L'accent est mis sur l'identification d'une méthode alternative pour extraire efficacement les propriétés optoélectroniques de ces échantillons. L'étude implique la variation de la composition de l'oxyde de zinc en ajustant la concentration en oxygène, ce qui donne des échantillons aux propriétés distinctes. L'ellipsométrie spectroscopique est utilisée pour étudier les propriétés optoélectroniques telles que la concentration de charges, la mobilité des porteurs de charges, la photo-résistance, la résistance électrique, la photoabsorption et l'énergie de bande.

De plus, un nouveau modèle d'indice de réfraction, le modèle de Birouk, est appliqué pour tester la compatibilité et l'efficacité des échantillons. Par la suite, un processus de raffinement consiste à trier les échantillons présentant des caractéristiques favorables d'une série précédente. Ces échantillons sélectionnés font l'objet d'une étude approfondie en faisant varier le facteur de température de deposition. En utilisant l'ellipsométrie spectroscopique, nous avons étudié ces échantillons pour acquérir une compréhension complète de leurs propriétés. L'examen des échantillons comprend l'évaluation de leurs points forts en vue d'applications potentielles dans divers secteurs industriels.

Pour améliorer l'utilité pratique de l'étude, des relations mathématiques expérimentales sont déduites afin de simplifier l'extraction des propriétés optoélectroniques et de valider leur précision. Cette recherche vise à apporter des informations précieuses pour les applications industrielles et à fournir une base pour des études futures dans le domaine.